Modeling of pellet cladding interaction

Jerome Sercombe, Bruno Michel, Chantal Riglet-Martial, Olivier. Fandeur

Modeling of Pellet Cladding Interaction

J. Sercombe[1], B. Michel[1], C. Riglet-Martial[1], O. Fandeur[2]

[1] CEA, DEN, DEC, F-13108 Saint-Paul-lez-Durance, France.
[2] CEA, DEN, DM2S, Gif-sur-Yvette, France.
e-mail: jerome.sercombe@cea.fr

Abbreviations

AGR	Advanced Gas-cooled Reactor
BWR	Boiling Water Reactor
CANDU	CANada Deuterium Uranium reactor
EOL	End Of Life
EPMA	Electron Probe Micro-Analyzer
FE	Finite Elements
FEM	Finite Element Method
FG	Fission Gas
FGR	Fission Gas Release
FP	Fission Products
HBS	High Burnup Structure
IP	Inter-Pellet
I-SCC	Iodine-Stress Corrosion Cracking
LHR	Linear Heat Rate
LWR	Light Water Reactor
MP	Mid-Pellet
MPS	Missing Pellet Surface
MTR	Material Testing Reactor
PCI	Pellet Cladding Interation
PIE	Post-Irradiation Examination
PPN	Peak Power Node
PWR	Pressurized Water Reactor
RIA	Reactivity Initiated Accident
RTL	Ramp Terminal Level
SEM	Scanning Electron Microscopy
SIMS	Secondary-Ion Mass Spectrometry
UO_2	Uranium diOxide
WWER	Water Water Energy Reactor

Contents

1 Pellet Cladding Interaction phenomenology

Pellet-Cladding Interaction (PCI) failures, discovered in the early 1970's, can be avoided in electro-nuclear reactors thanks to optimized plant operational procedures and fuel management schemes. Research and development programs are however still undertaken worldwide in order to improve the understanding of the mechanisms possibly leading to PCI failure, as well as to qualify a PCI resistant rod design. These research and development programs associate experiments and modeling in order to reduce the number of experiments.

A nuclear fuel element typically consists of a metallic tube containing cylindrical uranium dioxide fuel pellets. In the reactor, heat is generated in the pellets by nuclear fission reactions and transfered through the cladding tube to the surrounding coolant. In consequence, a quasi-parabolic radial temperature gradient holds in the fuel pellets with the maximum temperature at the pellet center. In consequence of the thermal stresses induced by the radial temperature gradient, radial cracks develop in the pellets and their opening increase in order to accommodate the excess central thermal expansion. The fuel pellet thermal expansion, swelling due to fission products accumulation and the clad creep-down lead at some point to the closure of the pellet clad gap. When pellet-clad contact is well established, these radial cracks lead to a stress and strain localization in the clad inner wall, as illustrated in Figure 1. The magnitude of clad stresses and strains in front of pellet radial cracks is however limited by frictional sliding at the pellet-clad interface.

Another consequence of the radial temperature gradient and associated radial thermal expansion gradient in the fuel pellet fragments is the axially non uniform radial deformation (maximum in front of pellet ends), originally refered as pellet "hourglassing" or "wheatsheafing". This non uniform fuel pellet deformation will also induce an increase of the clad stresses and strains in front of the pellet ends leading to residual strains in the cladding, characterized at the end of irradiation by a "bamboo-like" shape with regularly spaced ridges, see Figure 1.

A power transient of significant magnitude (power ramp) following a well established pellet clad contact can eventually lead to clad failure by Iodine Stress Corrosion Cracking (I-SCC), a failure mode initiated at the clad inner wall, generally in front of pellet radial cracks and pellet ends (see Figure 2). The availability of fission products (iodine, cesium, tellurium ...) released from the fuel pellet core, which migrate in the opened pellet radial cracks to the clad inner surface, is a key factor for the initiation of I-SCC.

In this chapter, a review of PCI models is proposed. Industrial approaches proposed by fuel vendors or utilities and which have proved to give excellent results in avoiding PCI failures by limiting power variations [1] are out of the scope of the present chapter. **The aim of this chapter is to detail the advanced multi-dimensional modeling of the phenomena leading to a stress-strain and iodine concentration at the clad inner wall during a power transient, and eventually to fuel rod failure by I-SCC**. Complementary information on PCI-SCC failure of zircaloy claddings can be found in the reviews of Cox [2] and Sidky [3] and in chapter XX "A review of Pellet-Cladding Interaction behavior in zirconium alloy fuel cladding" by Piro et al. [4].

In section 2 of this chapter, the experimental characterization of PCI is first briefly discussed by the presentation of typical Post Irradiation Examinations (PIE) performed on industrial fuel rods after power ramps. These experimental measures are essential to assess the simulation results.

In consequence of the correlation between fuel pellet radial cracks location and clad I-SCC cracks, the first historical attempts to model PCI have been focused on catching the stress-strain concentration in the cladding over an opening pellet radial crack. Analytical solutions derived from elastic pellet fragment and cladding models are recalled in section 3.

With the development of computers, 2D radial-tangential (2DRθ) FE analyses of a fuel pellet fragment have been performed to study in more details the impact of friction at the interface on stress-strain concentrations in the cladding over an opening pellet radial crack. The main models and results of these 2DRθ FE analyses of PCI are presented in section 4.

The impact of pellet "hourglassing" and pellet cracking on stress-strain concentrations in the cladding is nowadays studied by 3D FE analyses. These highly sophisticated descriptions of PCI include non-linear material models which can describe the viscoplasticity of the pellet and the cladding. The stress-relaxation at the pellet-clad interface resulting from pellet cracking and pellet/clad creep during power increase can therefore be properly evaluated. The 3D models for PCI are described in section 5. The 2D radial-axial (2DRZ) models for PCI, a subgroup of 3D models, will also be reviewed in section 5.

In the last decade, efforts have been focused on the introduction of sophisticated FG models and FP chemistry in PCI simulations, with the main objective to assess the impact of fuel pellets initial composition on FG induced swelling and FGR during power transients. These efforts have been triggered by the development of commercial doped fuels with additives in small proportions that modify the fission gas retention (related to grain-growth) and possibly the chemical composition of the gases released from the fuel pellet. Models and simulation results are presented in section 6.

Finally, to conclude this chapter, the models available for the simulation of clad failure by I-SCC will be briefly described.

2 In-reactor PCI assessment

2.1 Power ramps in Material Testing Reactors

The PCI failure propensity of a nuclear fuel element can be assessed by power ramp tests performed in MTRs. Short rods (called rodlets) are needed for the tests. They are fabricated in hot cell laboratories from a full length rod pre-irradiated in a power reactor, using a qualified fabrication process, or from a simple separation process if pre-designed segmented rods are used. The experimental procedure for power ramp tests aims at simulating reactor power transients, especially control blade movements for BWRs and class 2 transients for PWRs. Two main types of experimental sequence are generally considered: the “staircase” ramp [5] or the single step ramp [6], see Figure 3 for a schematic description.

The staircase ramp is an efficient way to estimate the PCI threshold but is certainly less aggressive than the single step ramp because of the stress relaxation in the fuel and the cladding during the holding periods at each step [7] [8]. Prior to the transient, a conditioning period is applied in order to re-establish the thermo-mechanical and physico-chemical state of the rod achieved at the end of the base irradiation in power reactor. The power transient rate is often around 10 $kW.m^{-1}.min^{-1}$, but more severe rates up to 100 $kW.m^{-1}.min^{-1}$ can be applied to explore the influence of ramp rate on PCI resistance [9] [10]. In order to achieve all the conditions required for PCI failure, in addition to a sufficient power increase from the conditioning plateau, a sufficient holding time at RTL is necessary. This time is needed for the development of I-SCC cracks in the cladding [2]. The formation of I-SCC cracks during the holding period is related to 1) the release kinetics of fission products from the fuel pellet, 2) the incubation time of I-SCC, as shown by out-of-pile I-SCC laboratory test results [11]. For research purposes, power ramp sequences with zero holding time are sometimes performed to improve the understanding on the main phenomena involved during a power transient [12] [13].

The technological PCI limit of the different fuel rod designs is derived from the analysis of a ramp test database, which has to cover a wide range of burnup [12]. Thanks to the use of a standardized methodology for ramp resting, the PCI performance of standard and advanced designs can be compared. While there is evidence of a higher PCI resistance of MOX fuel [14] [15], chromia doped fuel [13] [16] or advanced cladding with protective inner coatings [2] [4], the main challenge is to understand the mechanisms at the origin of the differential behavior of the rods, whether related to the cladding or fuel materials, burnup or irradiation conditions prior to the ramp tests.

2.2 Post Irradiation Examinations

To help understanding the mechanisms behind PCI, non-destructive and destructive examinations are performed on fuel rods before and after the ramp test. PIEs can include clad diameter profilometry, eddy current measurements of the external zirconia thickness, visual inspection, neutron radiography, gamma spectrometry, fission gas puncturing, optical microscopy, examinations by SEM, EPMA or SIMS measurements of FPs distribution. These examinations, illustrated in Figure 4, give valuable information on the kinetics of the numerous phenomena involved in PCI:

- Fuel rod profilometry give access to the residual clad strains, the clad diameter increase, the clad ridges height in front of pellet ends (IP level) and at mid-pellet level (MP), before the ramp, and also, after the ramp, as a function of the local power reached during the ramp.

- Optical microscopy on fuel cross-section or longitudinal fuel section give access to the pellet cracking (number and extension of each type of cracks), pellet dish filling, fuel microstructure (porosity distribution), cladding damage shape and location (hydrides, I-SCC crack), interface conditions between fuel and cladding (thickness and distribution of internal zirconia, bonding).

- SEM, EPMA and SIMS examinations give access to the fuel microstructure evolution in more details (FG bubbles concentration and size, location whether in the grains or at the grain boundaries, HBS, grain boundary cracking), to the FP distribution (concentration and location), and to cladding I-SCC mechanims [17] (intergranular, transgranular propagation by pseudo-clivage, fluting).

- Gamma spectometry give access to power axial distribution through the measurement of non mobile period isotopes such as ^{140}La, movements of volatile FPs such as ^{137}Cs.

Examinations performed after power ramp tests are very useful to evaluate the capacity of numerical simulations to quantify the numerous non-linear phenomena that compete during a power transient. In return, modeling tools can contribute to a better understanding of PCI, since they can be used to assess the impact of each phenomenon or parameter on the fuel rod behavior during transient conditions, as will be discussed in the next sections. Obviously, a good simulation of in-reactor Pellet Cladding Interaction should describe both materials with a similar precision and with material properties based on out-of-pile tests. While cladding mechanical properties can be measured on irradiated samples [18], mechanical testing on irradiated fuel is still a challenge in consequence of the pronounced in-reactor cracking of the fuel pellets. Another difficulty in PCI modeling is the lack of out-of-pile tests that fully reproduce the in-reactor loading and chemical environment at the clad inner surface.

2.3 Fuel pellet cracking during irradiation

From PIE after power ramps, fuel pellet radial cracks are known to be the root of fuel rod failure by PCI, see Figure 1. A precise assessment of the chronology of fuel pellet cracking during irradiation in reactor is therefore of importance. The evolution of fuel pellet radial cracking during base irradiation and power ramps is schematically described in Figure 5.

The mechanisms by which pellet cracking occurs during normal operating conditions may be summarized as follows. During startup, the radial thermal gradient in the pellet give rise to high circumferential and axial tensile stresses at the pellet periphery. In consequence, radial and transverse cracking occurs. Oguma showed that radial cracking is initiated at a low power level (6 kW/m) and that the number of cracks increases step-wise with the rod power [20]. At hot state, radial crack propagation towards the pellet center is limited by the compressed central part of the pellet [21]. During cooling down, compressive stresses are progressively relieved and radial cracks might then extend towards the pellet center generally leading to well divided pellet fragments as illustrated in Figure 6.

The number of pellet fragments after irradiation depends mainly on the power level reached in reactor. It increases with the rod power [20] [24]. For PWR conditions (mean rod power around 20 kW/m), PIEs indicate an average number of radial cracks close to 10 [25]. This estimate is consistent with three-dimensional thermo-elastic simulations of fuel pellet cracking which show that the hoop stresses at the pellet periphery remain below the tensile strength of the fuel if the fuel pellet

is divided in 8 identical fragments [26]. It is important to stress that radial cracking during base irradiation occurs mainly when the pellet-clad gap is open and that it is reasonably described by simulations assuming an elastic behavior for the materials (creep can be neglected). Transverse cracking (in planes perpendicular to the axial direction, also refered as axial cracks) also takes place during reactor start-up almost simultaneously with radial cracking and extends to the pellet core during cooling.

The situation is rather different during power ramps. First, the pellet-clad gap is generally closed at the end of the conditioning plateau. The temperature in the pellet is higher and leads to significant creep of the material [25]. The strong pellet-clad interaction upon power increase leads furthermore to high stresses in the cladding with possible plastic and viscoplastic flow. The stable crack pattern obtained after the first power cycle in normal operating conditions is modified by power rise and the development of new radial and transverse cracks initiated at the pellet periphery can be observed, as illustrated in Figure 6. The radial extension of these secondary cracks is limited by the size of the (visco)plastic central region of the fuel pellet under compression. Power shutdown leads to radial tensile stresses at the boundary between the highly deformed (visco)plastic central part of the pellet and the elastic outer layer and hence to circumferential cracking. Circumferential cracking is particularly important when viscoplastic flow has been high, i.e., in ramp tests with long holding times [22], as shown in Figure 6. Additional transverse cracks might appear with radial cracks during a power ramp with a radial extension also limited by the viscoplastic central core of the pellets.

3 Analytical models for PCI

3.1 Introduction

Early works on PCI have tried to assess the importance of fuel pellet radial cracking on stress concentration in the cladding. Some authors have derived closed-form solutions to estimate the stress concentration factor ($\sigma_{\theta\theta}^{max}/\sigma_{\theta\theta}^{average}$) as a function of the applied thermal and mechanical load on the cladding [27] [28] [29] [30] [31] [32]. Fuel performance codes are generally based on a radial one-dimensional description of the fuel pellet and the cladding [33] [34] [35] (see Chapter 3.19 "Oxide Fuel Performance Modeling and Simulation" for an overview). In consequence, this type of code cannot provide estimates of stress or strain concentration in front of an opening radial pellet crack which is by essence a two-dimensional problem. To fill this gap, some of these closed-form solutions are used in fuel performance codes to improve the one-dimensional description of PCI [36] [37]. A pre-requisites to stress concentration models is that the crack mouth opening is known. In this respect, so-called hoop enrichment models have been developed to estimate the impact of the thermal gradient, of solid swelling and of the contact pressure in a pellet fragment on the crack mouth opening [37]. In this section, closed-form solutions for the pellet crack mouth opening and the stress intensification in the cladding are recalled and used to illustrate the important parameters for PCI analyses.

3.2 The pellet fragment crack opening model

This solution, based on the theoretical work of Muskhelishvili [38], is detailed in reference [39]. The problem at hand concerns a two-dimensional fuel pellet fragment obeying to an elastic isotropic behavior. The pellet fragment is assumed to be divided in N identical fragments. The boundary conditions are illustrated in Figure 7.

Neglecting first the internal rod pressure, it might be assumed that the outer surface of the pellet fragment is free. When the fuel pellet clad gap is open, the loading consists of a radial distribution of strain corresponding to an isotropic swelling which can be approximated by:

$$\epsilon^{an} = \sum_{k\geq 2} \epsilon^{an}_{k+1} r^k \tag{1}$$

with r the pellet radius. In this general expression, a thermal strain gradient induced by heat generation from nuclear fission and heat transfer corresponds to $k = 2$. Other types of swelling (solid swelling, fission gas induced swelling) can be taken into account by the general expression of ϵ^{an} provided their radial distribution is known.

When the pellet cladding gap is closed, the pellet fragments are submitted to loadings that lead to opposit effects: the swelling strain gradient tends to open the radial cracks while the contact pressure tends to close the cracks. The balance between these two phenomena leads to a partial closing of the cracks along the radius, represented by a contact radius (denoted as R_c in Figure 7). To derive relevant approximations of the displacement field, the pellet fragment is divided in two parts as shown in Figure 7.

In the first part ($0 \leq r \leq R_c$), pellet fragments are in contact and the displacement field (radial u_r and tangential u_θ displacements) is given by:

$$\begin{aligned} u_r &= \frac{\gamma}{G}(1-2\nu)\, r + \sum_{k\geq 3} \epsilon^{an}_k \frac{1+\nu}{1-\nu}\frac{r^k}{k+1} \\ u_\theta &= 0 \end{aligned} \tag{2}$$

with G the shear modulus, ν Poisson's ratio and γ a constant parameter (Pa).

In the second zone ($R_c \leq r \leq R$), the displacement field is given by the general expressions:

$$\begin{aligned} u_r &= \sum_{k\geq 3} \epsilon^{an}_k \left[\frac{1+\nu}{1-\nu}\frac{1}{k+1} + \frac{1}{2\,G}\left((3-4\nu-k)\alpha_k \cos\left((k-1)\theta\right) - \beta_k \cos\left((k+1)\theta\right)\right)\right] r^k \\ &+ \frac{A}{2\,G}\left[(4-4\nu)\cos(\theta)\ln\left(\frac{r}{r_0}\right) + (2-4\nu)\theta\sin(\theta) - \cos(\theta)\right] \\ u_\theta &= \frac{1}{2G}\sum_{k\geq 3} \epsilon^{an}_k \left[(3-4\nu+k)\,\alpha_k \sin\left((k-1)\theta\right) + \beta_k \sin\left((k+1)\theta\right)\right] r^k \\ &+ \frac{A}{2G}\left[(2-4\nu)\theta\cos(\theta) - (4-4\nu)\sin(\theta)\ln\left(\frac{r}{r_0}\right) - \sin(\theta)\right] \end{aligned} \tag{3}$$

with the coefficients (α_k, β_k) given by the following relations:

$$\begin{aligned}\alpha_k &= \frac{1+\nu}{1-\nu}\frac{2G}{k+1}\frac{\sin\left((k+1)\theta_m\right)}{\sin\left(2k\theta_m\right)+k\sin(2\theta_m)} \\ \beta_k &= \frac{1+\nu}{1-\nu}\frac{2G}{k+1}\frac{(1-k)\sin\left((k-1)\theta_m\right)}{\sin(2k\theta_m)+k\sin(2\theta_m)}\end{aligned} \tag{4}$$

θ refers to the angular position with respect to the crack plane of the fragment while θ_m is equal to half of the fragment angle (see Figure 7). It is worth noticing that the displacement is singular at the apex of the fragment. To avoid these singularities, a small region close to this apex ($0 \leq r \leq r_i$ with $r_i << R$) is truncated and the parameter r_0 is chosen such that the radial displacement at $r = r_i$ is zero in an average sense:

$$\frac{1}{2\theta_m}\int_{-\theta_m}^{\theta_m} u_r(r_i,\theta)\,d\theta = 0 \tag{5}$$

The coefficient A in eq. 3 is such that the average radial stress on the pellet periphery equilibrates the contact pressure P_c:

$$\begin{aligned}A &= \frac{R}{4\sin(\theta_m)}\left\{-P_c\,\theta_m + \sum_{k\geq 3}\epsilon_k^{an}R^{k-1}\left[\frac{2G}{k+1}\frac{1+\nu}{1-\nu}\theta_m\right.\right. \\ &+ \left.\left. k\left(\alpha_k\frac{k-3}{k-1}\sin((k-1)\theta_m) + \frac{\beta_k}{k+1}\sin((k+1)\theta_m)\right)\right]\right\}\end{aligned} \tag{6}$$

With this approximated solution, the displacement field cannot be continuous on the boundary between the two zones ($r = R_c$). A good approximation is however derived by forcing this continuity condition at the particular point (R_c, θ_m):

$$\begin{aligned}u_\theta^{zone2}(R_c,\theta_m) &= 0 \\ u_r^{zone1}(R_c,\theta_m) &= u_r^{zone2}(R_c,\theta_m)\end{aligned} \tag{7}$$

From relations 7, the value of the parameter r_0 and of the contact radius R_c can be determined.

3.3 Pellet fragment crack opening during PCI

The model was applied to a pellet fragment submitted to a parabolic radial distribution of strain $\hat{\epsilon}^{an}(r) = \epsilon_1^{an} + \epsilon_3^{an}\,r^2$, representative of thermal strains experienced by fuel pellets during nominal irradiation or power ramps [39]. The authors studied the impact of the thermal strain magnitude, of the contact pressure P_c and of the number of pellet fragments N on the calculated crack mouth opening along the radius of the pellet fragment. Results are plotted in Figure 8. The analytical expressions have been compared with FE simulations performed with the code Cast3M [40].

The pellet crack mouth opening reaches 10 μm for a temperature difference across the radius close to 1000 K ($\epsilon_3^{an} = -7.5\,10^{-4}$ mm^{-2}). Increasing thermal strains leads to higher crack mouth openings and smaller contact radii R_c. Increasing the contact pressure leads to smaller crack mouth openings with greater contact radii R_c. The

calculations with a high contact pressure are representative of the closing of pellet radial cracks when strong PCI takes place. Increasing the number of fragments in the pellet tends to reduce the crack mouth opening but has very little impact on the contact radius. Similar results were obtained by Klouzal and Dostál from FE simulations performed with ABAQUS [41].

3.4 The clad stress concentration model

Roberts studied the case of a pellet divided by N regularly spaced cracks having an angular displacement of $2\theta_m$ between them and a crack mouth opening of 2ϕ [28], in contact with a cladding tube, as represented in Figure 9.

In this approach, the pressure on the clad external wall was assumed equal to zero, a uniform pressure was considered on the inner cladding surface together with a shear stress related to the radial stress and the friction coefficient. The author showed that the problem resolved into a standard one, namely finding the distribution of elastic stresses in a thick-walled cylinder having specified normal and shear stresses on the inner and outer surfaces. An Airy stress function satisfying the compatibility equation and the symmetries of the problem and of the following form was proposed:

$$\Phi = A_0 r^2 + B_0 \ln r + \sum_{m=2}^{\infty} \left(A_m r^{m+2} + B_m r^{-m} + C_m r^m + D_m r^{-m+2} \right) \cos(m\theta) \quad (8)$$

with A_0, B_0, A_m, B_m, C_m and D_m constant parameters. By derivation, the plane strain stresses in the cladding are given by:

$$\begin{aligned}
\sigma_{rr} &= 2A_0 + \frac{B_0}{r^2} - \sum_{m=2}^{\infty} \big[(m+1)(m-2) A_m r^m + m(m+1) B_m r^{-m-2} \\
&+ m(m-1) C_m r^{m-2} + (m-1)(m+2) D_m r^{-m} \big] \cos(m\theta) \\
\sigma_{\theta\theta} &= 2A_0 - \frac{B_0}{r^2} - \sum_{m=2}^{\infty} \big[(m+1)(m+2) A_m r^m + m(m+1) B_m r^{-m-2} \\
&+ m(m-1) C_m r^{m-2} + (m-1)(m-2) D_m r^{-m} \big] \cos(m\theta) \\
\sigma_{r\theta} &= \sum_{m=2}^{\infty} \big[m(m+1) A_m r^m - m(m+1) B_m r^{-m-2} + m(m-1) C_m r^{m-2} \\
&- m(m-1) D_m r^{-m} \big] \sin(m\theta) \qquad (9)
\end{aligned}$$

The displacements in the cladding tube read as follows:

$$\begin{aligned}
u_r &= \frac{1}{G} \Big\{ 2A_0(1-2\nu) r - \frac{B_0}{r} + \sum_{m=2}^{\infty} \big[(2(1-2\nu) - m) A_m r^{m+1} + m B_m r^{-m-1} \\
&- m C_m r^{m-1} + (2(1-2\nu) - m) D_m r^{-m+1} \big] \cos(m\theta) \Big\} \\
u_\theta &= \frac{1}{G} \Big\{ \sum_{m=2}^{\infty} \big[(m + 4(1-\nu)) A_m r^{m+1} + m B_m r^{-m-1} + m C_m r^{m-1} \\
&+ (m + 4(1-\nu)) D_m r^{-m+1} \big] \sin(m\theta) \Big\} \qquad (10)
\end{aligned}$$

In the above expressions, σ_{rr} denotes the radial, $\sigma_{\theta\theta}$ the hoop and $\sigma_{r\theta}$ the shear stress. The radial and circumferential displacements are signified by u_r and u_θ, respectively.

The original formulation proposed by Roberts was modified by Sercombe et al. [39] to account for boundary conditions closer to those taking place in a PWR fuel rod, see Figure 9: a non-zero external pressure related to the coolant p_{ext} is considered, a linear evolution of the contact pressure with angular position given by $p_{cont} = K_1\theta + K_2$ is assumed, a fuel rod gas pressure p_{gas} is applied on the clad inner wall which is not in contact with the pellet ($-\phi \leq \theta \leq \phi$).

The boundary conditions reflect the discontinuity of the contact pressure and shear stresses on the inner surface of the cladding due to the pellet crack opening ($-\phi \leq \theta \leq \phi$).

Since the clad materials (Zircaloy based alloys) are usually two to three times softer than uranium dioxide, Pellet Cladding Interaction is conveniently described by applying an azimuthally uniform radial displacement on the inner clad surface rather than a constant pressure. This point was discussed by Ranjan and Smith [29] and led to the derivation of their so-called hard pellet model. Jackson showed furthermore by FE analyses that a linear variation in contact pressure with angular position can lead to a substantial reduction in the variation of the radial displacement [31].

Achieving a constant radial displacement on the inner clad wall is by essence impossible with Roberts' approach. To fulfill that condition as much as possible, a minimization of the angular variation of the radial displacement has been proposed by adding the following condition on the contact pressure slope [39]:

$$\min_{K_1} \left\{ \int_{\phi}^{\theta_m} \left[u_r(b,\theta) - u_r(b,\theta_m) \right]^2 d\theta \right\} \tag{11}$$

which can be expressed as :

$$2 \int_{\phi}^{\theta} \left[u_r(b,\theta) - u_r(b,\theta_m) \right] \times \left[\frac{\partial u_r}{\partial K_1}(b,\theta) - \frac{\partial u_r}{\partial K_1}(b,\theta_m) \right] d\theta = 0 \tag{12}$$

from which K_1 can be deduced.

3.5 Clad stresses during PCI

The impact of the number of pellet fragments, of the pellet crack opening and of the friction coefficient on the hoop stress distribution in the cladding was studied with this analytical solution. The main results are presented in references [39] [42] and illustrated in Figure 10.

According to the model, increasing the initial pellet fragmentation (4 to 16 fragments, crack opening 8 μm, friction coefficient 0.5) leads to a moderate decrease of the maximum hoop stress (from $\sim$ 900 MPa to $\sim$ 800 MPa). An increasing crack mouth opening has a similar impact on the maximum hoop stress since it leads to a larger area where stresses are concentrated. The most important parameter with respect to stress concentration in the cladding appears to be the friction coefficient. A reasonable variation of the friction coefficient between 0.5 and 1.5 can be assumed

based on the litterature review of friction coefficient measurements detailed in reference [43] [44]. As shown in Figure 10, the maximum hoop stress in the cladding is more than doubled when the friction coefficient increases from 0.5 to 1.5. Klouzal and Dostál confirmed these results with the FE code ABAQUS [41]. Apart from giving the main trends during PCI, these analytical solutions have been used to verify advanced FE simulations of PCI with friction [39].

4 2DRθ Finite Element models for PCI

4.1 Introduction

The analytical solutions for the PCI problem presented in section 3 are restricted to fuel and clad materials with an elastic behavior. They are furthermore based on independent solutions for the pellet radial crack opening and for the clad stress concentration problem. During in-reactor PCI, many additional phenomena take place within the fuel pellet and the cladding. Among the most important are fuel irradiation and thermal creep, clad irradiation and thermal creep, fuel radial, circumferential and axial secondary cracking, fuel solid and FG induced swelling. They can lead to a drastic change of the stress and strain state within the fuel and the cladding. At the interface, friction can also evolve in consequence of irradiation.

To enhance the description of PCI, 2D radial-tangential (2DRθ) FE models of the fuel pellet with explicit radial cracks have been developed and used with sophisticated fuel and clad materials models. Among this category fall the 2DRθ pellet fragment models of the FALCON [45] [46], BISON [47] and ALCYONE fuel performance codes [19].

In this section, the FE mesh and boundary conditions considered in 2DRθ calculations will first be described. The modelling of fuel pellet cracking and creep and of clad creep and plasticity will then be detailed in order to explain the consequences of these phenomena on clad stress distribution during PCI. The impact of friction at the pellet-clad interface will then be discussed. Finally, the PCI failure models derived from 2DRθ simulations will be detailed.

4.2 Finite Element mesh and boundary conditions

As the fuel pellet fragmentation occurs quasi-immediately during reactor startup, a reasonable assumption adopted in 2DRθ models is to consider that the fuel pellet is initially divided in a finite number of identical fragments. Based on PIE performed after nominal irradiation in PWR, an initial fragmentation in 8 pieces is generally considered in 2DRθ simulations. By symmetry, only half of the fuel pellet fragment needs to be considered if proper boundary conditions are enforced. This is the case in the fuel performance codes FALCON and ALCYONE. In BISON, the 2DRθ simulations have been performed so far with more than one fragment in order to catch the loss of symmetry induced by the presence of a MPS [47].

To discuss the 2DRθ FE modeling of PCI, the boundary conditions considered in ALCYONE will be described. ALCYONE is a multi-dimensional FE based code that includes all the basic components of fuel performance codes, as summarized in

Table 1, and detailed in Chapter 3.19 on "Oxide fuel performance code modeling and simulation".

The FE mesh and boundary conditions considered in the 2DRθ scheme of ALCYONE are illustrated in Figure 11 and can be summarized as follows:

- Zero tangential displacement ($U_\theta = 0$) on the axis of symmetry of the pellet fragment (Pr_1).
- Pellet-pellet inter-penetration along the radial crack (line Px_1) is forbidden by the unilateral contact condition $U_y \geq 0$. It must be stressed that the radial crack length and contact radius are not fixed a priori but are given at each time step by the mechanical equilibrium. This is the main difference with the 2DRθ schemes of FALCON and BISON where the crack radial extension are defined at the beginning of the simulations.
- In ALCYONE, generalized plane strain conditions are used in order to model the out-of-plane stress and strain. The out-of-plane condition consists in a uniform axial strain ϵ_z. Before pellet-clad contact, the pellet and clad axial strains are independent. Upon contact, an axial locking condition is enforced to suppress the axial relative movement between the pellet and the cladding, $\Delta\epsilon_z^{pellet} = \Delta\epsilon_z^{clad}$. In ALCYONE, a smeared crack model (see section 4.3) is used to model transverse cracking in the 2D(r,θ) scheme.
- In ALCYONE, unilateral contact is assessed and a Coulomb model is introduced to simulate friction-slip or adherence at the pellet-clad interface. A specific gap element with normal and shear components is used in FALCON to model the same phenomena.

Concerning the loading conditions, the internal rod pressure (gas pressure) is applied to the cladding inner surface and to the pellet fragment outer surface if there is no contact with the cladding or the adjacent fragment. The external pressure (water pressure) is applied to the cladding outer surface.

In general, the temperature of the cladding surface in contact with the coolant, the pressure of the coolant and the internal pressure of the fuel rod are extracted from preliminary simulations of the complete fuel rod (from standard 1.5D simulations) and applied directly as boundary conditions in the local 2DRθ calculations that are usually performed at the PPN where PCI failures are most likely to occur.

4.3 Modeling of fuel pellet secondary cracking

In recent years, a significant number of papers have been devoted to the modeling of fuel pellet cracking during reactor operation, mostly due to the development or the availibility in commercial software of new numerical methods. The FEM with cohesive zones was used by Williamson [48] and Dostal [49] (solid and hollow pellets of WWER reactors) to study fuel pellet cracking in 2DRθ simulations during start-up, long-term irradiation, power transients and reactor shutdown. Compared to the fixed radial crack length of FALCON and BISON, cohesive zones do not require a pre-define length and are interesting for studying the crack propagation

during the loading sequence. The number of potential cracks and their orientation must however be set initially and cannot be changed during the simulations. The FEM with pre-defined non cohesive discrete cracks was used by Haynes to study the opening of radial cracks in Advanced Gas Cooled (AGR) reactor hollow pellets and the resulting stress concentration in the steel cladding [50].

The development of fuel pellet radial and circumferential cracks during reactor operation has also been studied in 2DRθ with the Discrete Element Method [51] or with the peridynamic theory [52]. A somewhat similar approach has been proposed by interfacing all the continuum elements of the mesh with cohesive zones [53]. Contrary to the discrete or cohesive crack methods, the stochastic nature of pellet cracking and the connection/bifurcation of radial cracks at the pellet center during power shutdown are nicely reproduced, see Figure 12. The main drawback being the increased CPU time required for the computations.

Recently, 3D FE simulations of a complete fuel pellet were proposed using a smeared crack model with crack orientations related to the principal stresses [54], see Figure 13, from which the pellet "hourglassing" can be recovered. So far, no simulation with the cladding have however been performed with these numerical methods.

The development of secondary cracks in the fuel pellet during power ramps (see Figure 6) has been less treated in numerical simulations owing to the complex behavior at hand, which requires the simultaneous modeling of fuel pellet creep, clad creep and plasticity, fuel fission-gas induced swelling and friction at the pellet interface. In order to account for secondary pellet cracking during irradiation, smeared crack models are convenient for fuel performance codes based on the FEM since these models show similarities with strain-hardening plasticity and can be readily implemented [55] [23]. The formulation proposed used in ALCYONE fuel performance code is here described to illustrate the general behavior of smeared crack models [23] [56]. The stress-strain constitutive law for the fuel material is given by Hooke's law as follows :

$$\boldsymbol{\sigma} = \boldsymbol{C} : (\boldsymbol{\varepsilon} - \boldsymbol{\varepsilon}^{vp} - \alpha_{fuel}\Delta T\mathbf{1} - \sum_{i=1}^{3} \epsilon_i^c \boldsymbol{n}_i) \tag{13}$$

with $\boldsymbol{\sigma}$ the stress tensor, $\boldsymbol{\varepsilon}$, the total strain tensor, $\boldsymbol{\varepsilon}^{vp}$ the creep strain tensor, α_{fuel} the thermal expansion coefficient, ΔT the temperature increase and $\mathbf{1}$ the unit tensor. ϵ_i^c refer to the crack strain component in direction i with its associated normal tensor $\boldsymbol{n}_i$. $\boldsymbol{C}$ is the fourth-order elastic tensor. Other strain tensors associated with fuel swelling (solid or gaseous) are omitted here for the sake of clarity.

The yield stress of the material in tension is described by three independent failure criteria :

$$f_i = \sigma_i - R_i(\epsilon_i^c) \leq 0 \tag{14}$$

In eq. 14, σ_i refers to the stress component in direction i, R_i is the fuel residual tensile strength in direction i. Since normal or off-normal reactor operating conditions lead generally to well defined radial, circumferential and axial cracks, the orientation of cracks can be prescribed by the cylindrical coordinate system

$(i = r, \theta, z)$. The orientation of the cracks can also be defined from the directions of the principal stresses or strains [55] [45]. 2DRθ simulations of PCI showed however that the crack orientations were very close to the radial and tangentiel directions [57], justifying the prescribed cylindrical orientations.

The development of cracking once the yield stress is reached and till complete loss of stiffness can be represented by a linear softening law, as expressed by the following equation:

$$R_i(\epsilon_i^c) = \langle f_i^t - K_i \epsilon_i^c \rangle \tag{15}$$

with f_i^t and K_i respectively as the fuel tensile strength and the softening modulus in direction i. $\langle A \rangle = A$ if $A > 0$ and 0 if $A \leq 0$. Exponential softening laws are another possible choice. As in standard plasticity, the crack strain rate in direction i is given by the consistency condition $\dot{f}_i = 0$.

The stress-strain relationship obtained from eqs. 13-15 in any direction ($i = r, \theta, z$) is illustrated in Figure 14 (left) along path 0-1 (elastic loading), path 1-2 (softening part with a decreasing tensile strength R_i) and path 2-3 (fully cracked material with no residual strength $R_i = 0$). These expressions are applicable only for monotonic loading conditions during which crack openings tend to increase. During normal operating conditions in reactor, the fuel undergoes loading cycles which can lead to crack closing. As illustrated schematically in Figure 14 (right), crack closing or/and re-opening are taken into account by modifying the elastic modulus of the material such that $\epsilon_i^c = 0$ when $\sigma_i = 0$ [56] (path 2-0 and 3-0). The history of crack-induced damage is thus described by the residual tensile strength variable R_i. To account for the irregularity of crack surfaces, Jernkvist proposed a slightly modified version with a progressive closing condition dependent on the compressive load applied [55] (complete closure possible only if a certain compressive stress is reached).

The smeared crack model requires two input parameters per direction i: the fuel tensile strength f_i^t and the softening modulus K_i. A reasonable assumption is to consider the fuel tensile strength independent of the direction, i.e., $f_i^t = f_t$. For temperatures below 1200°C, the tensile strength is relatively constant and close to that measured at room temperature [58] [59]. Based on an extensive experimental program, Radford derived analytical formulae to estimate the tensile strength at room temperature of UO_2 as a function of porosity and grain size [60]. For a standard UO_2 of porosity 3-4% and grain size 10 μm, the tensile strength is close to 130 MPa [25].

The other parameters of the fuel pellet crack model are the softening moduli K_i. It is well known that the use of material laws which account for softening leads to mesh-size dependent calculations. One way to overcome this problem is to use generalized fictitious crack models [61] in which the softening path is made dependent on the mesh size in order to ensure that the dissipated energy equals the fracture energy of the material. In a uniaxial tensile test such as is represented in Figure 14, the following relation holds between the fracture energy G_f, the tensile strength f^t, the softening modulus K_i and the mesh size in direction L_i:

$$G_f = \frac{1}{2} \frac{(f_i^t)^2}{K_i} . L_i \tag{16}$$

For UO_2, the fracture energy G_f is approximately 10 J/m^2, as estimated from Vicker's indentation tests performed on irradiated fuel samples [62]. Another method used for mesh-size independent calculations is to include viscous damping [55] with the drawback that the tensile strength can be locally exceeded.

In compression, a non-brittle behavior is generally considered with only creep strains. This is a reasonable assumption for base irradiation and power ramps since the power transients are sufficiently slow to allow for pronounced stress relaxation by creep. In fast transients such as those occuring during RIA, the behavior of the fuel in compression is better described by elasto-plasticity [63] [64].

4.4 Modeling of fuel pellet creep

The constitutive law describing creep of UO_2 generally involves three creep mechanisms [65]: irradiation creep, scattering-creep for small stresses and dislocation-creep for large stresses. Creep strain rate is given by the following relation:

$$\dot{\boldsymbol{\varepsilon}}^{vp} = \dot{\boldsymbol{\varepsilon}}^{irr} + (1+\alpha\phi)\left[(1-\theta)\dot{\boldsymbol{\varepsilon}}^{scat} + \theta\dot{\boldsymbol{\varepsilon}}^{disl}\right] \tag{17}$$

in which $\dot{\boldsymbol{\varepsilon}}^{irr}$, $\dot{\boldsymbol{\varepsilon}}^{scat}$ and $\dot{\boldsymbol{\varepsilon}}^{disl}$ are respectively the irradiation, scattering and dislocation creep strain rate tensors. The switch from scattering-creep to dislocation-creep is defined by the function $\theta(\sigma_{eq}, T)$ which depends on the temperature and the stress level, as proposed by Monerie and Gatt [66].

The creep strain tensors obey the normality rule and are usually expressed as a function of the equivalent creep strain rates $\dot{\epsilon}^i_{eq}$ according to :

$$\dot{\boldsymbol{\varepsilon}}^{i} = \frac{3}{2}\dot{\epsilon}^i_{eq}\frac{\boldsymbol{s}}{\sigma_{eq}} \tag{18}$$

with σ_{eq} the Von Mises stress and $\boldsymbol{s}$ the stress deviator tensor. The equivalent creep strain rates are then defined according to the following relations:

$$\dot{\epsilon}^{irr}_{eq} = A_{irr}\sigma_{eq}\phi\exp\left(-\frac{E_{irr}}{RT}\right) \tag{19}$$

$$\dot{\epsilon}^{scat}_{eq} = A_{scat}\sigma_{eq}\frac{1}{d_g^2}\exp\left(-\frac{E_{scat}}{RT}\right) \tag{20}$$

$$\dot{\epsilon}^{disl}_{eq} = A_{disl}\sigma^8_{eq}d_g^2\exp\left(-\frac{E_{disl}}{RT}\right) \tag{21}$$

In Eqs. 19, 20 and 21, A_i and E_i are constant parameters, ϕ is the local fission density, d_g the grain size and σ_{eq} the Von Mises stress. α models the increase of thermal creep with irradiation as observed for scattering-creep. Fuel densification can be included in the formulation of fuel creep resulting in a poro-viscoplastic formulation [63] [67] [66].

4.5 Modeling of clad creep and plasticity

The anisotropic behavior of irradiated SRA Zy-4 cladding must be taken into account in the multi-dimensional calculations of PCI. A coupled creep-plasticity model with isotropic non-linear hardening has been proposed by Soniak [18], based on an extensive database of creep laboratory and in-reactor tests performed on irradiated clad samples at temperatures ($280-400°$C), stress levels ($0-550$ MPa), fast neutron fluxes ($1-2.10^{-18}$ n/m^2/s) and fluences ($0-10.10^{25}$ n/m^2), representative of normal and power transient conditions.

As for the pellet material, the stress-strain constitutive law for the clad material is given by Hooke's law as follows :

$$\boldsymbol{\sigma} = \boldsymbol{C} : (\boldsymbol{\varepsilon} - \alpha_{clad}\Delta T\mathbf{1} - \boldsymbol{\varepsilon}^{vp} - \boldsymbol{\varepsilon}^{p}) \tag{22}$$

with $\boldsymbol{\varepsilon}^{vp}$ the creep strain tensor and $\boldsymbol{\varepsilon}^{p}$ the plastic strain tensor. The creep component of eq. 22 accounts for irradiation and thermal creep contributions and can be split as follows in rate form :

$$\dot{\boldsymbol{\varepsilon}}^{vp} = \dot{\boldsymbol{\varepsilon}}^{irc} + \dot{\boldsymbol{\varepsilon}}^{thc} \tag{23}$$

Each of the creep components includes primary creep and secondary creep. To account for the anisotropy of the material, the creep strain rates are function of Hill's equivalent stress $\sigma_H = \sqrt{\boldsymbol{\sigma} : \boldsymbol{H} : \boldsymbol{\sigma}}$ with $\boldsymbol{H}$ a symmetric fourth rank tensor and obey the normality rule given by:

$$\dot{\boldsymbol{\varepsilon}}^{i} = \dot{\epsilon}^{i}_{eq}\boldsymbol{H} : \frac{\boldsymbol{\sigma}}{\sigma_H} \tag{24}$$

with $\dot{\epsilon}^{i}_{eq}$ the equivalent creep strain rate. σ_H reads as follows when the tube reference system (r,θ,z) is used :

$$\sigma_H^2 = H_r(\sigma_{\theta\theta} - \sigma_{zz})^2 + H_\theta(\sigma_{rr} - \sigma_{zz})^2 + H_z(\sigma_{rr} - \sigma_{\theta\theta})^2 + 2H_{r\theta}\sigma_{r\theta}^2 + 2H_{rz}\sigma_{rz}^2 + 2H_{\theta z}\sigma_{\theta z}^2 \tag{25}$$

The formulation depends on three coefficients H_r, H_θ, H_z which have been identified from uniaxial and biaxial creep tests (the shear components are assumed equal to the isotropic ones, i.e., $H_{r\theta} = H_{rz} = H_{\theta z} = 1.5$). Hill's coefficients are identical for irradiation and thermal creep. The equivalent irradiation creep strain rate is expressed as follows:

$$\dot{\epsilon}^{irc}_{eq} = \dot{\epsilon}^{irc1}_{eq} + \dot{\epsilon}^{irc2}_{eq} \tag{26}$$

with the primary creep component $\dot{\epsilon}^{irc1}_{eq}$ given by :

$$\dot{\epsilon}^{irc1}_{eq} = A_{irc1}\frac{\sigma_H^{n1}}{(\epsilon^{irc1})^{n2}}\exp\left(-\frac{E_{irc1}}{RT}\right) \tag{27}$$

and the secondary creep component $\dot{\epsilon}^{irc2}_{eq}$ given by :

$$\dot{\epsilon}^{irc2}_{eq} = A_{irc2}\sigma_H^{n3}\dot{\Phi}^{n4}\exp\left(-\frac{E_{irc2}}{RT}\right) \tag{28}$$

In Eqs. (27) and (28), A_{irc1}, A_{irc2}, n_i $(i = 1, 4)$ and E_{irc1}, E_{irc2} are constant values. Creep rate enhancement due to the effect of the fast neutron flux $\dot{\Phi}$ on the material is taken into account in the stationary creep component $\dot{\epsilon}^{irc2}$.

The equivalent thermal creep strain rate reads as follows:

$$\dot{\epsilon}^{thc} = V_s + \left[(V_p - V_s) \exp\left(-\frac{\epsilon^{thc}}{\epsilon_0} \right) \right] \tag{29}$$

with V_p, V_s given by :

$$V_p = V_{p0}(T, \sigma_H) V_{pf}(\Phi) \tag{30}$$

$$V_s = V_{s0}(T, \sigma_H) V_{sf}(\Phi) \tag{31}$$

and $\epsilon_0(T, \sigma_H)$ a function of temperature T and Hill's stress σ_H. V_p (primary thermal creep rate) and V_s (secondary thermal creep rate) are equal to the product of two functions which parameters are identified from tests performed on fresh Zy-4 ($V_{p0}(T, \sigma_H)$, $V_{s0}(T, \sigma_H)$) and on irradiated Zy-4 ($V_{pf}(\Phi)$, $V_{sf}(\Phi)$). The latter functions account for the reduction in thermal creep rates with irradiation, as observed experimentally [18].

As for creep, the plastic model is based on Hill's equivalent stress with Hill's coefficients given as a function of the temperature T and the fluence Φ [68] (except the shear components). The plastic criterion is given by:

$$f(\sigma_H, \epsilon^p, T, \Phi) = f_1(\epsilon^p, T) + f_2(T, \Phi) \tag{32}$$

with $f_1(\epsilon^p, T)$ accounting for the strain-hardening of the material (ϵ^p is the equivalent plastic strain) and $f_2(T, \Phi)$ for irradiation-induced hardening. The plastic strain rate is given by the normality rule.

4.6 Modeling of friction at the pellet clad interface

Pellet-clad friction modeling is usually based on Coulomb's law which relates the sliding rate v_t at the interface of two materials to the normal F_n and tangential forces F_t according to the following expression:

$$\begin{cases} v_t = 0 \quad if \quad \|F_t\| \leq \mu \|F_n\| \\ v_t = -\lambda F_t \quad if \quad \|F_t\| = \mu \|F_n\| \end{cases} \tag{33}$$

where μ is the friction coefficient, λ a positive number and $\|F\|$ denotes the norm of force vector F.

Brochard and al. have summarized the test conditions and friction coefficient measures performed by different authors [43]. Most of the tests were performed out-of-pile on non-irradiated materials and are therefore only representative of pellet-clad friction at the beginning of irradiation in commercial reactors. The overall variation of the friction coefficient was found to be within $0.4 < \mu < 0.69$ [69] [70]. Among the

tests, those of Nakatsuka were performed in experimental conditions representative of a power transient [70], i.e., temperatures $300 - 400°C$, contact pressure 100-200 MPa, internal corrosion layer of a few μm thick, and lead to friction coefficients in the range 0.47-0.6.

From in-pile friction tests, several authors showed that the friction coefficient increases significantly (up to 1.2) with irradiation [71] [72] [73]. These measures can be related to the evolution of the pellet clad interface during in-reactor normal operation which is characterized by the development of an internal zirconia layer approximately 10-15 μm thick [74] [75]. A common feature of high burnup fuel rods with a formed HBS, irrespective of the reactor, pellet and cladding type, is the strong pellet-clad bonding at the interface that is observed at EOL [76] [77] [78] [79] [80] [81]. Generally, bonding is associated with the development of a $(U,Zr)O_2$ reaction layer at the interface between the pellet rim and internal zirconia [82] [83] [81]. A constant friction coefficient at the pellet-clad interface in simulations of reactor operations is certainly not realistic.

From the relation between friction coefficient and the calculated secondary radial cracking during ramp testing of fuel pellets of increasing burnup, Sercombe et al. have derived a function that can be used to assess the evolution of the pellet-clad interface with irradiation [19]:

$$\mu = 0.56 \exp\left(0.03 \Delta\tau\right) \tag{34}$$

where $\Delta\tau$ (in GWd/tU) is the mean burnup variation after initial pellet clad gap closing. According to relation (34), clad-pellet friction evolves only when pellet-clad gap is closed since internal zirconia is only found in fuel rods parts where contact is effective [74]. The friction coefficient increases with burnup to reach a value of $\sim$2 at 60 GWd/tU.

To account for the evolution of the pellet-clad interface in their simulations of lift-off experiments, Suzuki et al. have related the evolution of pellet clad bonding to a time integral of the contact pressure at the pellet-clad interface [84] [85].

4.7 Impact of friction and fuel creep on clad stresses

The impact of friction, fuel and clad creep/plasticity on clad stresses was studied with the fuel performance code ALCYONE by 2DRθ FE simulations of a power ramp (RTL $\sim$ 400 W/cm, holding time 12h) on a UO_2-Zy4 fuel rodlet of average burnup $\sim$ 25 GWd/tU [19]. Twenty simulations with a friction coefficient in the range $0.5 - 5$ were performed. The simulations were first performed with an infinite tensile strength f^t to avoid fuel secondary cracking. Creep of the pellet and of the cladding were therefore the only stress-relief mechanism taken into account.

The calculated deformed shape of the pellet fragment at RTL is illustrated in Figure 15 for a friction coefficient equal to 1.7. The high thermal gradient in the pellet (over 1000°C) leads to a small opening of the pellet radial crack (25 μm). The opening of the crack is restricted by friction forces at the pellet clad interface which prevent significant sliding in the calculation. In consequence of the high tangential forces that develop at the interface, a pronounced hoop stress localization in the cladding takes place in front of the crack tip, as shown in Figure 15.

The resulting stress intensification factor is plotted in Figure 16 (with circles) as a function of the friction coefficient. The maximum hoop stress increases significantly with friction. A plateau is however reached for friction coefficients greater than 2 [43] [41]. The plateau is a consequence of the plasticity of the cladding material with limited strain-hardening.

A similar spatial distribution of the plastic strains in the cladding was obtained in the 2DRθ simulations [19]. The hoop stress distribution in the pellet at RTL is plotted in Figure 17 for the simulation with a friction coefficient of 1.7.

Owing to the thermal gradient, a rather standard distribution with compressive stresses at the pellet center and tensile stresses at the pellet periphery is obtained. The maximum tensile hoop stress at the pellet periphery increases by more than a factor 3 with the friction coefficient (circles). In the case of a friction coefficient of 0.5, representative of non-irradiated materials, the maximum hoop stress reaches 150 MPa, which means obviously that secondary cracking during power ramps cannot be avoided. Hoop stress saturation takes place when the friction coefficient exceeds 2 partly because of the plasticity of the cladding material and partly because of the creep of the fuel material at the pellet center which increases rapidly with the stress level.

Haynes et al. reached similar conclusions in their 2DRθ simulations of stress-strain concentration on the inner surface of the cladding resulting from the fuel pellet cracks [50]. The friction coefficient was found the most influencial parameter. The stress-strain concentration was surprisingly found insensitive to the number of pellet radial cracks. Their calculations were however performed with a pre-defined (and fixed) number of pellet radial cracks. Capps et al. reported an opposit trend with an increasing maximum clad hoop stress with increasing crack spacing [86]. The simulations were however performed assuming that there were no relative movements at pellet/cladding interface (infinite friction coefficient). They compared their results to FALCON simulations which showed no impact of the number of pellet radial cracks, in agreement with Haynes et al. [50]. These differences can be related to fuel pellet secondary cracking or sliding at the pellet-clad interface as detailed in the next section.

4.8 Impact of fuel secondary cracking on clad stresses

To study the developement of fuel secondary cracking and its impact on clad stresses, 2DRθ simulations with realistic properties for the tensile strength and the fracture energy of uranium dioxide have been analyzed in reference [19]. The hoop stress distribution at RTL is illustrated in Figure 18 for a simulation performed with a friction coefficient of 1.7.

The stress distribution was found very different from the one obtained when creep was the only stress-relief mechanism (Figure 17). While the center of the pellet is still under compression at a similar stress level, intense secondary radial cracking at the pellet periphery leads to a very high stress relaxation. Pellet cracking, represented in Figure 18, tends in fact to level the stresses with a maximum that never exceeds the tensile strength of the material, whatever the friction coefficient. This point is illustrated in Figure 17 by plotting the maximum tensile hoop stress in the brittle

pellet as obtained from all the simulations (square symbols). The maximum hoop stress is almost constant ($\approx$ 100 MPa) when secondary cracking is considered in the simulations.

In Figure (19), the impact of the friction coefficient on secondary radial cracking at RTL is illustrated. The mesh elements that are plotted on the fragment are those where the residual strength of the material R_θ is less than 5 MPa, i.e., where local failure of the material is achieved.

The total number of secondary radial cracks in the pellet fragment increases with friction which explains the leveling of the maximum hoop stress. The impact of secondary radial cracking on the stress intensification factor in the cladding is shown in Figure 16 (square symbols). Stress concentration in front of the crack tip appears limited in magnitude (maximum 1.4) compared to the calculations without secondary radial cracking (maximum 2.1). The stress intensification was furthermore insensitive to the friction coefficient. The same conclusion was drawn from the maximum plastic strain in the cladding.

2DRθ simulations show the counterbalanced effect of increasing friction which tends: 1) to increase clad stresses and strains due to increasing interfacial shear forces and 2) to enhance radial cracking of the pellet which in turn leads to some leveling of the clad stresses and strains. Pellet-cladding friction combined to pellet secondary cracking leads therefore to an almost stable stress and strain state in the cladding, far from the estimations presented in section 3 for elastic materials. It also indicates that FE models with a pre-defined number of radial cracks might overestimate the stress concentration in the cladding during PCI. In this respect, Capps et al. mention that the stress concentration in the cladding depends on the (fixed) length of the radial cracks considered in the simulations [86], showing the importance of the unilateral condition ($U_y \geq 0$ on the crack plane) described in Figure 11.

4.9 PCI failure threshold in 2DRθ models

The 2DRθ model of FALCON with a pre-defined radial crack of finite length has been used by Lyon et al. to assess the PCI-SCC failure/non failure of a database of fuel rods [87]. The fuel failure/non failure assessment relies on the definition of a cumulative damage index (CDI) coupled with a local cladding stress evaluation [45]. The CDI is updated at each time step of the 2DRθ calculation based on the hoop stress $\sigma_{\theta\theta}$ in the cladding element right over the tip of the pellet radial crack, the local clad temperature T and the burnup of the rodlet B. The CDI increment is defined from a time-to-failure empirical function t_f obtained from laboratory I-SCC tests (pressurized tube) performed on non irradiated clad samples, and dependent on the same quantities (stress, temperature, burnup, yield stress):

$$D = \int_0^{t_n} \frac{dt}{t_f(\sigma_{\theta\theta}, B, T)} \tag{35}$$

A threshold stress and a minimum burnup are furthermore used to activate the model. A CDI-based failure probability function was derived assuming that the CDI calculated from 14 power ramps followed a normal distribution. Lyon et al. showed

that the CDI was more appropriate than the maximum clad stress to assess the failure/non failure of the rods during loading sequences that often included more than one power ramp [87].

Capps et al. analyzed nearly the same database of power ramps with the 2DRθ and 3D models of BISON with explicit radial cracks to define a PCI-SCC hoop stress threshold that could discriminate failed and non failed fuel rods [47]. They used a probability function to identify a 5% failure probability stress threshold for standard PCI-SCC. The threshold was then compared to the maximum hoop stress calculated in a fuel rod that was confirmed to contain an MPS of known dimensions. Simulations of a series of power sequence on fuel rods with an MPS of unknown dimension were used to estimate the size of the defect that could have led to the observed non expected failure of the rods.

5 2DRZ and 3D Finite Element models for PCI

5.1 Introduction

While 2DRθ FE analyses are powerful to catch the stress-strain concentration in front of an opening pellet radial crack, they are not able to describe the pronounced axial localization in front of pellet ends that results in the clad ridges. In French PWR fuel rods tested in the OSIRIS MTR [6], clad failures always occur in front of pellet ends, showing the importance of the underlying mechanism for PCI failure assessment.

This has led to the development of 3D models for PCI based on the FEM [88] [44] [89] [90]. Taking advantage of the symmetries offered by pellet cracking and pellet geometry and in order to reduce calculation times, 3D models were originally restricted to a single fuel pellet fragment and overlying cladding. The progressive incorporation of pellet-clad friction [43], of fuel creep and fuel secondary cracking [23], of fission-gas induced swelling [91] and of sophisticated FG models coupled with fuel thermochemistry [92] to these early thermo-mechanical models is at the root of the multi-dimensional fuel performance code ALCYONE.

In the last decade, the multi-dimensional FEM based code BISON has been extensively developed with a similar approach aiming at the integration of the main phenomena considered in fuel performance codes in 3D multi-pellet calculations of fuel rods [93] [94] [95] [96] [97]. The BISON code is used by the BWR community to determine the origin of fuel rod failure by PCI, related or not to a Missing Pellet Surface [95] [86].

In this section, the complex boundary conditions required to model PCI in 3D will first be recalled. Simulations results will then be presented to illustrate the capacity of 3D models to catch the clad and pellet deformation during nominal irradiation and power ramps. The impact of fuel pellet secondary cracking, of fuel pellet creep and burnup on PCI will then be discussed. The clad local loading obtained from 3D simulations of PCI will then be analyzed to derive a thermomechanical PCI failure threshold. To end this section, the 2D radial-axial FE models of PCI (2DRZ) are discussed.

5.2 Mesh and boundary conditions

In the next sections, the 3D model of ALCYONE will be used to illustrate PCI simulation during base irradiation and power ramps. As for the 2DRθ scheme presented in section 4.2, the fuel pellet is assumed to be initially divided in 8 identical fragments. Taking advantage of the symmetries (mid-pellet plane and mid-fragment plane), only one quarter of a single pellet fragment and of the overlying piece of cladding are meshed (see Figure 20).

The pellet fragment description accounts explicitely for the geometrical particularities of the fuel element (dishes, chamfers, ...). The boundary conditions, illustrated in Figure 20, can be divided in three groups:

- In the axial direction, the boundary conditions must reflect the fact that the fuel pellet is part of a fissile column enclosed in a cladding tube. At the inter-pellet plane Ox_0y_0, unilateral contact conditions are prescribed ($U_z \geq 0$ with U_z the axial displacement). This condition is important to catch the hourglassing of the fuel pellet. The axial condition at the top of the fragment (plane Px_1y_1) and of the cladding piece consist in a uniform axial displacement U_z. Before pellet-clad contact, the pellet and clad axial displacements are independent. Upon contact, an axial locking condition is enforced to suppress the axial relative movement between the pellet and the cladding, $\Delta U_z^{pellet} = \Delta U_z^{clad}$. As shown by many three-dimensional simulations of fuel pellet cracking during reactor startup [44] [48] [49], a transverse fracture plane develops first at the mid-pellet plane. In ALCYONE, the smeared crack model (see section 4.3) is used to model the development of transverse cracks in the 3D scheme.

- In the circonferential direction, the boundary conditions must account for the neighbouring fragments. Pellet-pellet inter-penetration along the fracture plane Ox_0z is forbidden by the unilateral contact condition $U_y \geq 0$. As in the 2DRθ scheme, the pellet fracture plane opening stems from the solution of the mechanical equilibrium. The radial and axial extensions of the fuel pellet primary cracks are therefore not fixed a priori. On the opposit plane Or_0z, symmetry conditions imply that $U_\theta = 0$.

- In the radial direction, the fragmentation of the fuel pellet must be considered. In consequence, the pellet fragment central axis (Oz) must be free to move radially but not interact with the other fragments ($U_r \geq 0$). This condition is essential to catch the pronounced radial shift of the fuel pellet fragment (leading to clad ridges) in consequence of the fuel radial thermal gradient.

- Unilateral contact is assessed and the Coulomb model is introduced to simulate friction-slip or adherence at the pellet-clad interface (see section 4.6).

Loading conditions are similar to those considered in 2D (section 4.2): the internal pressure (gas) is applied to the clad inner surface and to the pellet fragment outer surface, the external pressure (water) is applied to the clad outer surface. The temperature of the clad surface in contact with the coolant and the pressure of the coolant are extracted from 1.5D fuel rod simulations and applied directly as boundary conditions in the 3D calculations. In general, the simulation is performed at the

PPN during the power ramp since it is the most likely location of standard PCI failures. In the fuel performance code BISON, the 3D simulations of standard PCI are performed with a quarter of the fuel pellet including three radially orientated craks of finite radial extension [96]. Analyses of PCI with a MPS rely on the modeling of a 5 pellet rodlet with no initial radial cracks in the fuel.

5.3 Modeling of Fission Gas Release and Swelling

The contribution of Fission Gas Swelling to the overall deformation of the cladding during PCI can be important and should be taken into account in 3D simulations. Theoretically, the FGR and the FG swelling models should be closely related. In most fuel performance codes however semi-empirical relations are used for fission gas swelling generally expressed as a function of temperature and burnup (see Chapter 3.19 "Oxide fuel performance modeling and simulation"). When it comes to 3D simulations of PCI during power ramps, the consistent formulation of FGR and gaseous swelling becomes essential because both phenomena are strongly related to the stress state in the fuel pellet which can vary significantly spatially and temporally in consequence of fuel pellet creep and of pellet dishes [98]. The non homogeneous radial deformation of the pellet during irradiation (higher at pellet ends) can also lead to smaller temperatures at the pellet center near pellet ends and consequently to some differences in FGR and gaseous swelling.

To explain the coupling and without going into the complex formulation of mechanistic FGR models (see chapter 3.20 "Modeling of Fission-Gas-Induced Swelling of Nuclear Fuels" for an overview), the problem might be summarized as follows [99]. Gas release from the fuel to the free volumes in the rod may be described schematically as a three stage process. First, intragranular bubbles migrate to grain boundaries. The assumed mechanism is surface diffusion in a temperature gradient. The flow of grain boundary gas to the interconnected porosity then occurs if the estimated grain surface occupied by intergranular bubbles exceeds a pre-defined percentage of the total grain boundary surface area. The transfer kinetics from the grain boundary to the interconnected porosity is generally assumed to be proportional to the difference in pressure between the corresponding gas populations. Finally, the flow of gas through the interconnected porosity to the free volumes which ultimately leads to its release is modelled as following a percolation law.

In advanced FG models, inter and intragranular swelling are considered. Intragranular bubbles coarsen as a result of both the influx of gas atoms from the matrix and of coalescence of moving bubbles. However, the coarsening kinetics is dictated at high temperature (above $\sim$1200°C) by the diffusion and trapping of vacancies. The fuel swelling computation is therefore based on the rate at which vacancies are captured by bubbles. The thermodynamic force governing the rate at which vacancies are captured by bubbles is proportional to the difference in vacancy concentrations between the concentration at the bubble surface and the thermal equilibrium vacancy concentration. The differential equation expressing bubble growth is generally of the following form:

$$\frac{dr_b}{dt} = -\frac{D_u}{kT}\omega\frac{1}{r_b}\left(P_{ext} + \frac{2\gamma}{r_b} - P_b\right) \tag{36}$$

where r_b is the bubble radius, D_u the uranium self diffusion coefficient, T the local fuel temperature, P_{ext} the surrounding hydrostatic stress (calculated from the stress tensor $\boldsymbol{\sigma}$ given by the fuel mechanical behaviour model, i.e., $P_{ext} = -\frac{1}{3}\boldsymbol{\sigma} : \mathbf{1}$), P_b the bubble inner pressure, γ the fuel surface tension and ω the volume occupied by a molecule of UO_2 in the lattice. A similar treatment is applied to intergranular swelling, only bubbles are described as taking on a lenticular shape.

The strains associated to fission gas swelling can be estimated as a function of the concentration in bubbles in the fuel and as a function of their radii:

$$\epsilon^{gs} = \frac{4}{3} c_{bia} \pi \alpha r_{bia}^3 + \frac{4}{3} c_{bie} \frac{S_g}{V_g} \pi \alpha r_{bia}^3 \tag{37}$$

where ϵ^{gs} is the gaseous swelling volumetric strain, c_{bia} and c_{bie} are the number of intragranular and intergranular bubbles per unit volume of fuel, respectively, r_{bia} and r_{bie} are the bubbles' radii and S_g/V_g is the ratio between the grain boundary surface and the grain volume.

Finally, the stress-strain constitutive law for the fuel material including the contribution of fission gas induced swelling in addition to fuel creep and cracking strains reads as follows:

$$\boldsymbol{\sigma} = \boldsymbol{C} : \left(\boldsymbol{\varepsilon} - \alpha_{fuel} \Delta T \mathbf{1} - \boldsymbol{\varepsilon}^{vp} - \sum_{i=1}^{3} \epsilon_i^c \boldsymbol{n}_i - \frac{1}{3} \epsilon^{gs} \mathbf{1} \right) \tag{38}$$

The above equations show how the fission gas swelling and mechanical behaviour models are coupled. According to equation 36, small, highly pressurized bubbles will have a tendency to grow. However, bubble growth is hindered as compressive stresses are set up in the fuel pellet center during a PCI event. Fission gas fuel swelling appears therefore as a balance which results from the diffusive phenomena involved: fission gas, uranium vacancy diffusion and fuel creep.

In PCI simulations with FG swelling, the thermal, mechanical and gaseous swelling problems are strongly coupled, resulting in the so-called multiphysics problem [91] [100]. As described schematically in Figure 21, the temporal resolution of the coupled system of equations (heat balance equation, heat conductance in the gap, mechanical equilibrium, constitutive laws, fission gas swelling) is done in the fuel code ALCYONE in a sequential way for each time interval dt. First the thermal problem is solved to determine the nodal temperature T at time $t + dt$ from the mechanical displacements U at time t. Second the mechanical equilibrium at time $t + dt$ (displacements U and stresses $\boldsymbol{\sigma}$ from the constitutive laws) is calculated from the updated temperature field T and the gas swelling strains ϵ^{gs} obtained at time t. The latter are then updated to give the gas swelling strains ϵ^{gs} at time $t + dt$. This step-by-step process is then repeated with the new set of state variables (T, U, $\boldsymbol{\sigma}$ and ϵ^{gs}) till the variations in temperature, displacements, stresses and gaseous swelling strains at each node during two consecutive iterations are less than prescribed tolerances.

To ensure a fast convergence and avoid oscillations, a specific acceleration algorithm has been developed for the stress - gaseous swelling problem [91] [101]. The difficulty is schematically explained in Figure 22. The evolution of the quantities of interest (hydrostatic pressure and gas swelling strain) with each other are opposit.

A decreasing hydrostatic pressure will favor the growth of fission gas bubbles and hence increase gaseous swelling. An increase in gaseous swelling will on the contrary increase the stress state and hence the hydrostatic pressure. An efficient way to improve the slow convergence of the coupled problem is to use 2 successive estimations of the hydrostatic pressure and of the gaseous swelling strain to get a new initial value of the gaseous swelling strain closer to the solution.

In ALCYONE fuel performance code, two mechanistic models for FG behavior are currently integrated in the iterative scheme of the fuel performance code, designated by the acronyms MARGARET [102] and CARACAS [103]. Mechanistic models for FG behavior are also integrated in the FEM based fuel performance codes BISON [104] [105], FALCON [106] and FAST [107].

5.4 3D modeling of PCI

Results from 3D simulations of PCI with ALCYONE are presented in the next sections. The mechanical models for the fuel and the cladding and the interface are detailed in sections 4.3 to 4.6. The other models are referenced in Table 1.

5.4.1 Pellet clad gap closure

The mechanisms leading to pellet-clad gap closure and ridge formation in the cladding during base irradiation can be decomposed as follows [90]. During the first power increase, the radial thermal gradient leads to tensile stresses at the pellet periphery and to the fuel fragmentation. The radial thermal expansion gradient and the fuel fragmentation are at the origin of the non uniform radial deformation of the pellet along its height, leading the so-called hourglass shape. The consequence is a reduction of the gap first at the IP plane, as illustrated in Figure 23a.

During the constant power periods of the irradiation cycles, the fuel rod dimensions will change due to the following phenomena:

- Densification and swelling of the pellet,
- Clad irradiation creep under a compressive stress state induced by the coolant-rod pressure difference.

The competition between these phenomena leads to a decrease of the gap with two main periods for PCI:

- first, a low interaction period with a gap closed only near the IP plane,
- second, a strong interaction period with a gap closed everywhere along the pellet height and a significant contact pressure, generally around 5-10 MPa, as illustrated in Figure 23b.

During PCI, the peculiar shape of the pellet is printed in the cladding because inelastic strains related to irradiation creep tend to develop in consequence of the external pressure. Moreover, the decrease of the clad diameter when contact is established can reduce the magnitude of pellet radial deformation because of the stress relaxation induced by irradiation creep in the pellet fragment. According to

3D simulation results, it appears that the magnitude of clad primary ridges at the end of base irradiation is the result of the competition between cladding and pellet irradiation creep and also of the cladding anisotropy. The development of a high-burn up structure in the pellets with pronounced gaseous swelling tends to reduce the height of clad ridges by smoothing the radial deformation of the pellet during the last irradiation cycles [7].

5.4.2 Clad and fuel deformations during power ramps

The behaviour of fuel rods during power ramps is complex and depends on many factors: the geometry of the fuel pellet (height/diameter ratio of the pellet, dish volume, chamfer dimensions ...), the power history (initial burnup, maximum power, increase of power, power rate, duration of holding period ...), the thermo-mechanical behavior of the fuel and of the cladding (thermal expansion of the fuel pellet, cladding creep and plasticity, fuel creep, ...) and the fission gas swelling in the fuel pellet [108].

The diameter increase of the cladding during power ramps is mainly driven by the thermal expansion of the pellet and by fission gas swelling if the temperature of the pellet is high enough. The contribution of gaseous swelling can be high particularly if the holding period is exceeds 15 to 30 minutes or if the fuel rod has a high initial burnup.

Cladding expansion during power ramps is first induced at IP level due to the pellet deformation resulting from the radial thermal gradient (see Figure 24a). As soon as the temperature at the pellet center is high enough, clad expansion at IP level is limited by pellet dish filling due to creep of the fuel and gaseous swelling.

If the height/diameter ratio of the pellet is large ($\sim$ 1.5), the impact of dish filling on the MP plane will be small. Radial expansion will therefore be maximum at MP level since dish filling will limit radial expansion at IP level [7], see Figure 24b. This is the reason why clad ridges at MP level can reach significant values (30 μm) and often exceed their IP counterparts by a factor 2 or 3, see Figure 25.

In general, clad ridges at MP level do not develop in the case of pellets with height/diameter ratio $\sim$ 1, as shown by PIEs of BWR pellets. Clad strains induced by pellet ends radial deformation remain therefore predominant in this configuration leading mainly to clad ridges at IP level, see Figure 26. As shown by 3D simulations, dish filling has consequences on the deformation of the MP plane in short fuel pellets which explains the limited development of ridges at this level [7].

The kinetics of clad ridges development at MP level depends on the maximum power during the power ramp since the radial expansion of the pellet and the fuel creep depend mostly on temperature. In fact, the stress is at the power 4-8 in the formulation of fuel creep strain rates which ensures very fast creep rates in case of high temperatures. Figure 27 illustrates the evolution of the pellet diameter increase during power transients due to the total swelling of the fuel pellet and to gaseous swelling only, as a function of the maximum temperature of the pellet [98]. Also plotted is the evolution of dish filling. The plots were obtained from the 3D simulations results of more than 50 power ramps on UO_2 fuel rods.

As can be seen, when the pellet maximum temperature is greater than 1800°C, FG swelling has some impact on the fuel fragment expansion. The contribution of

gaseous swelling to the total diameter increase of the pellet during power transients remains however small and does not exceed 25% for the fuel rods considered in Figure 27 (average burnup < 45 GWd/tU). A threshold temperature can also be defined for complete dish filling in the 3D simulations. It is close to 1700°C and hence of the same order than the 1800°C for FG swelling activation. Simulation results indicate furthermore that 100% dish filling is usually reached within a few minutes during the holding period if the power is sufficient. The residual $\sim 80\%$ dish filling that is calculated is a consequence of the thermo-elastic shrinkage of the fuel pellet during cooling which leads to a small reopening of the dish.

5.4.3 Fuel pellet cracking

The development of secondary cracks in the fuel pellet fragment during nominal irradiation and power ramps is illustrated in Figure 28 by the presentation of isovalues of crack strains [23].

The end of nominal irradiation is characterized by the extension to the pellet center of an axial crack located at the MP plane. This crack actually appears during reactor startup but it closes at the pellet periphery at the end of nominal irradiation (or during any intermediate cooling phase) owing to fuel thermal shrinkage. The crack reaches the pellet center in the simulation because of the high tensile residual axial stress generated by fuel irradiation creep. Bentejac et al. showed that considering a MP axial crack is essential to avoid the formation of a clad ridges at MP level during nominal irradiation [89]. No secondary radial crack appears during nominal irradiation, showing that the initial fragmentation in 8 identical pieces is consistent with the stresses induced by the thermal gradient during the first power increase.

During the power ramp, the mid-pellet axial crack is closed because of the radial thermal gradient which leads to compressive stresses close to the fragment central axis (see Figure 28). During the transient stage of the power ramp, new axial and radial cracks appear on the fragment external surface as a result of the biaxial tensile stress state induced by the thermal gradient and friction at the pellet-clad interface. At the end of the power ramp, these new axial cracks formed at the pellet periphery and of limited radial extension due to the compressive stresses at the pellet center, extend to the fuel pellet core during power shutdown. The radial cracks generated when RTL is reached, are partially closed after shutdown. Simultaneously, circumferential cracks appear at approximately MP radius. The radial position of the latter is approximately equal to the radial extension of secondary radial cracks formed during the power ramp. It is furthermore related to the FG swelling that maintains significant compressive stresses in the central core of the fuel pellet in spite of fuel creep.

5.4.4 Assessment of a 3D model for PCI

A comparison between calculated and experimental measurements of the cladding outer diameter before and after the power ramp test is presented in Figure 25. In theory, the experimental data available for each single pellets could be compared to 3D simulations. In practice, the simulations are usually restricted to the pellet situated at the PPN during the power ramp, since it is the most likely location of

a PCI failure. The differences in initial burnup of the rodlets, maximum power and power increase during the ramp, duration of the power plateau lead to significant differences that a 3D model of PCI is expected to catch. Detailed comparison based on clad residual profilometry may include out-of-pile residual diameters after nominal irradiation, residual diameter increases at inter-pellet and mid-pellet level during power ramps, clad inter-pellet and mid-pellet ridges heights [109]. 3D simulations have a good capacity to assess the residual clad diameters after nominal irradiation and power ramps and the increase in residual diameter at MP and IP level during power ramps. The assessment of clad ridges heights is less precise owing to the small magnitude of clad ridges (5-15 μm in most cases) and the important experimental dispersion ($\pm 3\mu$m on ridges heights from 8 generatrices and 7 successive pellets [109]). The impact of pellet height on the development or not of ridges at the MP level is however one of the outcomes of 3D simulations [7].

The behaviour of the fuel pellet at IP level is rather complex since it results from a compromise between the pellet thermal and gaseous swelling which tend to increase the diameter, and the filling up of the dish due to fuel creep at high temperature which tends to reduce the diameter expansion. Therefore, data concerning dish filling are of importance to check that creep rates of the fuel are correctly estimated. In fact, overestimated dish filling leads to underestimated IP ridges and IP diameters [111]. Figure 29 gives an overview of the calculated dish fillings (residual) after ramp tests compared to experimental measurements.

The experimental residual dish filling are separated in three main categories depending on the holding period of the power ramp: 1) zero holding time (dish filling less than 20%), 2) short holding period less than 16 minutes (dish filling between 15 and 80%), 3) long holding period exceeding 16 minutes (dish filling $>$ 60%). Figure 29 shows that the calculated dish fillings are well estimated by the 3D model. In particular, small dish fillings ($<$ 20%) obtained on ramp tests with no holding periods, very important for assessing the clad loading during the power transient (and hence PCI failure), are correctly estimated. In practice, a more detailed assessment of calculations can be made by comparing the residual radial shape of the dish to the simulations, as illustrated in Figure 29.

From optical micrographs, the distribution, length and number of radial cracks can also be estimated after power ramps (see Figure 6). As discussed in section 4, the number and length of the radial cracks formed during a power ramp are dependent on the fuel material properties (tensile strength and fracture energy) and on the friction coefficient. These detailed information can be compared to 3D FE simulation results to check the magnitude of these parameters [113].

5.5 Analysis of clad loading in 3D simulations of PCI

5.5.1 Strain and stress concentration in the cladding

The distribution of stresses and strains in the cladding at RTL (mean burnup $\sim$ 25 GWd/tU, max. power 42.5 kW/m), as calculated from a 3D simulation of PCI with ALCYONE [114], are presented in Figure 30.

Overall, the expansion of the fuel pellet fragment leads to high tensile hoop stresses in the cladding, with a mean value of $\sim$450 MPa. As can be seen in Figure

30, the radial stress is maximum close to the IP plane, at the exact location where the chamfer starts, due to the axially non uniform radial deformation of the fragment and the contact discontinuity between two successive pellets. Consistent with the observed localization of PCI failures in ramp tested rodlets [6], the hoop stress and equivalent cumulated creep strain are maximum at the so-called triple point, i.e., in front of a pellet radial crack, at the clad inner wall and in front of pellet ends, see Figure 1.

5.5.2 Impact of fuel pellet cracking

The impact of fuel pellet radial cracking on clad local loading has been analysed by the comparison of 3D simulations of power ramps performed on a standard UO_2 fuel rodlet and on a UO_2 Cr-doped fuel rodlet [114]. In spite of a higher maximum power reached during the transient, the Cr-doped UO_2 rodlet survived the power ramp undamaged while the UO_2 rodlet failed. Michel et al. attributed this improved behavior to lower fracture properties (tensile strength, fracture energy) for the Cr-doped UO_2 fuel, as inferred from post-ramp PIEs that showed a higher density of secondary radial cracks at the pellet periphery than in the standard UO_2 fuel. The 3D simulation of the power ramp performed on the Cr-doped UO_2 rodlet led to the isovalues of crack strains presented in Figure 31, compared to those relative to the standard UO_2 rodlet. In consequence of the reduced fracture properties, secondary radial cracking is, as expected, much more developed at RTL.

The mechanical fields of Figure 30 are plotted in Figure 32 for the Cr-doped UO_2 fuel rodlet.

As can be seen, the calculated stresses and strains at the clad inner surface are higher for the Cr-doped UO_2 specimen than for the standard UO_2 rodlet. This is not consistent with the respective non failure / failure of the rodlets, respectively. Hence, other mechanical quantities have been introduced by Michel et al. to analyse clad loading [114]. The radial and tangential stresses, respectively σ_r and σ_t, were defined at the pellet-clad interface from the nodal forces according to:

$$[\sigma_r] = \frac{[\vec{f}][\vec{r}]}{\int_S [N(x,y,y]ds} \quad \text{and} \quad [\sigma_t] = \frac{[\vec{f}][\vec{\theta}]}{\int_S [N(x,y,y]ds} \tag{39}$$

with [], a symbolic definition for a nodal quantity, $\vec{f}$, the nodal force vector at pellet cladding interface, $\vec{r}$ and $\vec{\theta}$, the unit radial and circumferential vectors, $N(x,y,z)$ the finite element interpolation functions and S the area of a clad FE on the inner surface. According to this definition, the tangential stress σ_t represents the shear load at the pellet-clad interface. The radial and tangential stresses calculated for the two rodlets of interest are plotted in Figure 33.

A marked difference in the tangential stresses at the pellet/clad interface is observed, with the maximum obtained in the case of the standard UO_2 rodlet ($\sim$ 110 MPa in Figure 33b, $\sim$ 50 MPa in Figure 33d for the Cr-doped UO_2 rodlet). This result is the consequence of the more pronounced radial cracking of the Cr-doped UO_2 rodlet during the power transient which leads to a relaxation of shear stresses at the pellet-clad interface. Concerning the radial stresses, due to the chamfer height, the maximum takes place at the exact location where pellet ends are in contact with

the cladding. Interestingly, in both calculations, the triple point lies at the position where both the radial and shear stresses are maximum.

5.5.3 Impact of fuel burnup and friction coefficient

This approach was extended to high burnup UO_2 fuel rodlets (up to 60 GWd/tU) by Sercombe et al. [19]. As discussed in section 4.6, an increasing burnup leads to a modification of friction at the pellet-clad interface which increases the stresses at the pellet periphery during a power transient and hence might increase significantly the number of secondary radial cracks. To illustrate the importance of evolving friction with respect to PCI failure propensity, three dimensional simulations of two rodlet have been compared: a low burnup rodlet, irradiated 2 cycles (mean burnup $\sim$ 25 GWd/tU) ramped at an RTL of 425 W/cm, failed after a few minutes, a high burnup rodlet, irradiated 4 cycles (mean burnup $\sim$ 50 GWd/tU), ramped with no failure at 460 W/cm (holding time $<$ 15 minutes). For both rodlets, the number of secondary radial cracks were measured at MP and IP levels. At IP level, the high burnup rodlet had approximately twice the number of cracks of the low burnup rodlet. This difference in pellet secondary radial cracking was recovered in the 3D simulations thanks to the use of the burnup-dependent friction coefficient given by eq. 34 [19].

In Figure 34, the radial and shear stress distributions at RTL on the inner clad surface of the low and high burnup rodlets are compared.

The distribution of both stress components is strongly modified by the development of a high number of radial cracks in the case of the high burnup rodlet. A smoother distribution of stresses with no strong localization at the inter-pellet plane is obtained. The magnitude of shear stresses is also significantly reduced by radial cracking (maximum of $\sim$200 MPa for the low burnup fuel and of $\sim$150 MPa for the high burnup fuel). This result is consistent with the better resistance of high burnup fuel rodlets in ramp tests [115].

In the case of radial stresses, a smoother distribution along the pellet height with smaller maximum values is obtained for the high burnup rodlet. This distribution is not a consequence of enhanced radial cracking but of the higher dish filling that takes place in this fuel during the simulation of the ramp ($\sim$10% dish filling for the low burnup rodlet and 100% dish filling for the high burnup rodlet). Dish filling leads to a very high radial stress relaxation mostly at the inter-pellet plane. The higher power and the higher temperature in the pellet due to its higher burnup are at the origin of the marked difference in dish filling in the simulations. Dislocation creep is the main creep mechanism during ramp testing which explains the marked temperature dependency.

5.5.4 PCI failure threshold in 3D models

From 3D simulations with ALCYONE, a failure curve based on two calculated quantities, the mean circumferential stress in the cladding and the interfacial shear stresses at pellet-cladding interface, was proposed [114]. The authors analyzed with 2DRθ simulations the impact of prescribed interfacial shear and radial stresses on the distribution of hoop stresses in the clad inner wall. They showed that shear

stresses are by far the most important loading, confirming the importance of friction at the pellet-clad interface. Instead of the local maximum shear stress at the pellet-clad interface, an energy density due to circumferential friction forces during the transient stage was used [114]. This parameter, called $W_{r\theta}$, is calculated from the energy dissipated at the pellet-clad interface, divided by the surface of a potential through wall crack in the cladding, as detailed in eq. 40:

$$W_{r\theta} = \frac{\int_{S_{pellet}} \frac{1}{2}(f_{\theta 1} + f_{\theta 2})(\Delta u_{\theta 2} - \Delta u_{\theta 2})}{S_{cladding}} \tag{40}$$

with f_θ the circumferential component of the tangential nodal force at the pellet clad interface, Δu_θ the circumferential component of the tangential displacement discontinuity at the pellet-clad interface (see Figure 35). Subscripts 1 and 2 refer respectively to the value of the variables at the beginning and at the end of the power transient. S_{pellet} and $S_{cladding}$ are the pellet external and clad lateral surfaces, as shown in Figure 35.

This parameter can be considered as an upper bound of the energy density due to shear loading at the pellet clad interface that contribute to the cladding damage by I-SCC. In this approach it is assumed that the shear energy integrated on S_{pellet} is available for the formation of a through wall crack of surface $S_{cladding}$, which means that $W_{r\theta}$ can be approximately compared to the cladding toughness.

The two parameter PCI failure threshold (mean hoop stress in the cladding, shear energy density) has been applied to a database of 9 power ramps simulated in 3D with the code ALCYONE [114]. It was possible to clearly separate the failed fuel rods from the non failed, in which group the Cr-doped UO_2 pellets had reached very high RTL. The non failure of these rods was related to the reduced shear energy density in consequence of an increased number of secondary radial cracks.

Capps et al. tried to use the peak cladding hoop stress calculated with BISON from a 3D pellet model [47] to separate the failed and non failed rods from a database of 15 power ramps already analyzed with the FALCON code [87]. They could not identify a clear failure threshold stress, confirming the difficulties encountered in ALCYONE with a local stress-based criterion. Their analysis was exdented to three-dimensional simulations of a multi-pellet rodlet with an MPS where they obtained good correlations between the MPS width, the peak clad stress and the peak fuel temperature, thus confirming the deleterious impact of a MPS on the PCI failure threshold.

5.6 2DRZ Finite Element model for PCI

2DRZ axisymmetric Finite Element models are probably the most widely used models for PCI, due to the low computer cost required to run calculations compared to 3D. In this section, only the fuel performance codes dealing with discrete pellets will be discussed. A number of codes are based on a 2DRZ axisymmetric continuous representation of the fuel column which is close to the 1.5D representation where the fuel pellet geometry is not explicitely included. Discrete 2DRZ pellet models are available in the FALCON code (individual pellet) [45] [46], in the FEMAXI code

(individual pellet) [116], in the BISON code (multi-pellet) [95], in the FAST code (multi-pellet) [107] and in the ALCYONE code (individual pellet) [117].

While the stress concentration in the cladding resulting from fuel pellet radial cracks cannot obviously be catched by 2DRZ simulations, a number of experimental observations related to PCI can be reproduced. Among them, the increased clad loading in front of pellet ends and the partial or total dish filling during power transients.

In 2DRZ simulations including pellet creep/cracking and clad creep and plasticity, Rashid showed that the formation of clad ridges at the pellet interface but also secondary ridging at MP level could be reproduced [118]. The author developed a damage model to account for the loss of material stiffness in the directions perpendicular to the crack surfaces, leading to an orthotropic material behavior. This model is used in the FALCON code [45] and was recently implemented in the BISON code [94]. A similar approach is implemented in the FEMAXI code [116]. One interesting advantage of the 2DRZ representation is the lack of mesh dependency of the fuel radial cracking.

Helfer compared his 2DRZ simulation results to 3D simulations performed with ALCYONE and to experimental measurements of the external clad profilometry [117] [119] [120]. The pellet-clad gap closure kinetics, the development of IP clad ridges during base irradiation and of MP clad ridges during power ramps, as illustrated in Figure 36, were recovered by the 2DRZ simulations under the condition that fuel pellet radial cracking was included in the calculations [120]. To acount for the loss of material stiffness in the directions perpendicular to the radial direction, Helfer developed a damage model very similar to the one proposed by Rashid. The development of fuel pellet radial cracking during base irradiation is illustrated in Figure 36 by plotting the undamaged/damaged areas. Similar damage distribution are reported by Williamson et al. with the BISON code [94]. To illustrate the correlation between pellet hourglassing in 2DRZ simulations and the damage associated to radial cracking, the calculated radial displacement of the points situated on the symmetry axis is also plotted in Figure 36.

To account for radial cracking of the fuel pellet and hence increase the calculated IP clad ridges in the FAST code, Prudil et al. chose to add a crack strain component to the circumferential component of the elastic strain tensor to ensure that the elastic strain is always less or equal to zero. This approach corresponds to a limiting case where there is an infinite number of radial cracks and no stiffness in the circumferential direction [107].

6 PCI modeling with fuel thermochemistry

6.1 Introduction

The assessment of the PCI resistance of fuel rods during in-reactor irradiation relies on thermo-mechanical calculations performed with fuel performance codes, based on the conservative assumption that iodine is always available in sufficient quantities to induce I-SCC. While this approach together with constraints on power variations has given excellent results over the years, the development of UO_2 fuels with small

quantities of dopants [121] [122] has raised questions on the origin of their generally improved behaviour during ramps tests. In addition to the fuel thermo-mechanical properties (creep [13] [123], cracking), dopants might also modify the chemistry of volatile fission products (caesium, iodine, ...) and this mechanism may be of some importance with regards to PCI-SCC failures. Testing of hyper-stoichiometric UO_2 fuels with O/U up to 2.05 have shown that a small excess of oxygen in the matrix can lead to higher RTL without failure of the rods [5]. It has been suggested by the author that this improved behaviour was of chemical rather than mechanical origin. In fact, oxygen might compete with iodine at the clad surface and inhibit I-SCC or reduce the general pitting attack observed in pure iodine. Scanning Electron Microscopy with Energy Dispersive X-ray Spectroscopy (SEM/EDS) analyses of Al-Si-O additive fuels have shown the formation of a Cs-Al-Si-O compound at the grain boundary that could trap volatile species [124], such as iodine, and therefore explain the PCI resistance of these fuels at high power.

The modeling of volatile fission products chemistry in the fuel applied to PCI is still very limited. For PWR fuels, Baurens et al. have detailed a 3D calculation of a power ramp with thermochemical calculations of fission products chemistry and release with emphasis on the resulting partial iodine pressure at the clad inner wall [92]. Piro et al. studied the fission products chemistry during the irradiation of a UO_2 fuel up to a burnup of around 100 GWd/tU [125] [126]. Based on the calculated shape of the radial profile of oxygen potential in the fuel, the authors proposed an explanation for the PCI mitigation of high burnup fuels related to oxygen transport at the pellet periphery. Preliminary simulations with BISON including thermodynamic calculations of irradiated fuel and oxygen transport are reported in reference [127]. The 3D thermo-chemical-mechanical calculations of Baurens et al. were recently extended to account for oxygen transport in the fuel [128] [129] [130]. The authors analyzed the consequences of oxygen transport on the chemistry of the fission gas released from the fuel pellet during a power ramp.

In this section, an overview of these modeling approaches for PCI including fuel thermochemistry and oxygen transport will be given.

6.2 Thermochemistry of irradiated fuel

Most thermochemical models used in thermodynamic analyses of irradiated fuel define the equilibrium state of the multiphase and multicomponent system at hand at given temperature and pressure by the minimization of the Gibbs energy [131] [132] [133] [134]. Calculations for irradiated fuels require comprehensive thermodynamic data for all the compounds which are likely to be formed in the gaseous, liquid and solid state [135] [136] [137]. In general, the thermodynamic database includes one or several models describing the solubility of fission products (plutonium, rare earth mostly) in the uranium dioxide matrix in order to catch the pronounced evolution of the oxygen potential of the fuel with irradiation. For more details, see the chapter 1.17 "Computational Thermodynamics: Application to Nuclear Materials". Among the main iodine compounds of interest for PCI, the following species were considered in the 3D coupled thermo-chemical-mechanical simulations of Baurens et al. [92]: $CsI_{(s)}$, $CsI_{(l)}$, $CsI_{(g)}$, $Cs_2I_{2(g)}$, $I_{(g)}$, $I_{2(g)}$ and $TeI_{2(g)}$. In these simulations, special

attention was given to tellurium diodide since experimental results obtained on UO_2 fuel rods after a power ramp with no holding period showed a co-location of iodine and tellurium at the clad inner wall [138].

The thermodynamic calculations require initial estimations of the quantities of FPs in the fuel. The latter can be provided by complex neutronic calculations that account for all the isotopes and their decay chains [126] [139] [130]. Such calculations are necessary when nominal irradiation is considered since the FPs inventory increases progressively during irradiation cycles. For power ramps which are of particular interest in PCI analyses, the FPs inventory can be assessed by empirical correlations usually expressed as a function of burn-up [92], since the burnup of the fuel does not evolve significantly. In consequence of the often long period of time between the end of reactor irradiation and the power ramp, only the stable isotopes need furthermore to be considered. Concerning iodine, Fregonese et al. showed that the quantity of radioactive iodine isotopes created during a power transient performed on a fuel rod irradiated during 2 cycles in a PWR was negligible compared to the stable part [140].

To simplify the thermochemical analyses and to compensate for the lack of some specific thermochemical data, several authors reduce the number of FPs by grouping together those with a similar physico-chemical behavior [141] [134] [92]. An example of such arrangement is given in Table 2, the starting point of thermochemical calculations with ANGE, the thermochemical solver used in ALCYONE fuel performance code.

6.3 Thermochemistry and Fission Gas Release

The use of a thermochemical solver in a fuel performance code gives access to a great number of gas species that are formed by reaction between the FPs. The question of how these gas species move in the fuel and of how they are released from the fuel is not well established. In severe accident conditions, it is well known that the FP release depends on the thermochemical conditions applied to the fuel pellet, whether oxidizing or reducing [142] [143] [144]. The thermochemical equilibria at hand in the fuel are thus of importance to assess the chemical form of FPs in the gas phase and their release kinetics [145]. In PCI studies, only the central part of the fuel pellet reaches high temperatures where thermodynamic equilibrium can be considered. Fuel melting being unlikely (max. temperatures generally below 2500°C), it is reasonable to assume that only the gas species that are formed in the fuel can be released in the free volume of the rodlet. Condensed phases and species in solid solution in the fuel can thus be assumed immobile.

Baurens et al. adopted the following approach to couple the fuel performance code ALCYONE with the thermochemical solver ANGE and the inert fission gas release model MARGARET [92]. As illustrated in Figure 37, at each time step of a typical loading sequence, the thermochemical solver ANGE provides the spatial distribution of the concentrations in gas species. Ideal binary mixtures of each gas species with the major gas component, i.e., xenon, are then considered to define the transport of the minor components. The molar flux of each gas species i to the rod free volume ($J_{gas(i)\rightarrow rod}$) is obtained from the inert fission gas flux ($J_{Xe\rightarrow rod}$)

given by MARGARET and from the proportion of the gas species i (n_i) in the interconnected bubbles/pores filled with xenon (n_{Xe}). Note that this formulation implies that all the gas species i are available at grain boundaries. At each time step of the simulation, the quantities of each FP released in the rod free volume is subtracted from the total amount of each FP considered in the chemical equilibrium calculations. The observed consistency between the calculated radial profiles of FPs remaining in the pellets with SIMS measurements (I, Te, Cs, Xe) after a power ramp justifies a posteriori this treatment of chemically active gas release [92].

6.4 Evolution of Fission Products during a power ramp

A 3D simulation was performed by Baurens et al. [92] to study the FP distribution during a power transient. The power ramp was particularly interesting for PCI-SCC studies because of the high power reached (RTL of 52 kW/m) which had led to the development of I-SCC cracks on the inner surface of the cladding with a maximum penetration of around 100 µm. The short hold time (90 s) did not permit the extension of the cracks across the full thickness of the cladding thus leading to a rare case of a power ramp with PCI-SCC initiation but no failure.

The calculated fraction of rare gas (Xe, Kr) released from the pellet fragment during the power ramp, as illustrated in Figure 38, are strongly related to the axial hydrostatic pressure gradient in the central part of the pellet. In consequence, the release of inert fission gas at the IP plane is approximately equal to twice that calculated at the MP plane when the RTL is reached. The IP plane where the hydrostatic pressure is the lowest was shown to release the most. These results are an illustration of the strong coupling that holds between FGR and the stress state in the fuel pellet, as discussed in section 5.3.

The calculated fractions of iodine and caesium released from the pellet fragment during the power ramp are also shown in Figure 38. Since the volatile fission product release during the power transient and the holding period is related to the inert fission gas percolation flux, the iodine and caesium release from the pellet are also more pronounced near the IP plane. The axial gradient of species release at the pellet center is, however, much more pronounced than for xenon. At RTL, iodine release from the pellet center exceeds 90% close to the dish for approximately 30% at MP level. This result stems from a major impact of thermo-mechanics on thermochemistry. In fact, at MP level, the high hydrostatic pressure resulting from the stresses in the oxide matrix reduces the formation of gaseous species (other than inert gases) to the benefit of liquid or solid species. Conversely, at the IP level, the hydrostatic pressure is much lower which favors the formation of gaseous compounds, and the xenon flux is much higher. Consequently, the local release of iodine at the IP level is three times higher than at the MP level.

6.5 Chemical speciation of iodine in the fuel

Baurens et al. analyzed the chemical speciation of the iodine released from the fuel during a power transient [92]. The majority of the iodine was found to come from $CsI_{(g)}$ and to a lesser extent from $TeI_{2(g)}$. The spatial distributions of $CsI_{(g)}$ and

$TeI_{2(g)}$ during the power ramp are given in Figure 39.

The time evolution of gaseous $CsI_{(g)}$ shows a very pronounced axial gradient during the power transient followed by a reduction of the quantity close to the dish and a stable distribution during the holding period. It may be noticed that even if the bulk of the gas phase is preferentially released close to the dish, the local concentration in $CsI_{(g)}$ remains high (in yellow near the IP center, values close to 10^{-4} mol/mol UO_2). This stems from the solid-gas or liquid-gas equilibrium at hand in the fuel ($CsI_{(s,l)} \rightleftharpoons CsI_{(g)}$) which ensures that the released quantity of $CsI_{(g)}$ is replaced instantaneously.

The evolution of $TeI_{2(g)}$ given in Figure 39 is different from that of $CsI_{(g)}$. It appears at the fuel center during the power transient before the other gas components due to its formation at lower temperatures (around 1200 K) from the reaction of $MoO_{2(s)}$ with $Te_{(l,s)}$ and $CsI_{(s,l)}$. Consequently, $TeI_{2(g)}$ is released sooner during the power transient, in particular near the pellet fragment dish. At RTL, the local IP concentration in $TeI_{2(g)}$ is nill while it is still increasing at MP level. During the holding period, no change in the $TeI_{2(g)}$ distribution is observed. Contrary to $CsI_{(g)}$, $TeI_{2(g)}$ is therefore available in the fuel pellet center and near the dish only during a short period of time. This stems from the fact that upon a given temperature level (1900 K), $TeI_{2(g)}$ is destabilized in favor of $CsI_{(g)}$.

6.6 Thermo-chemical-mechanical based PCI-SCC initiation criterion

The occurrence of PCI-SCC in a ramp test depends on three main factors [2] [4]: a sufficient stress in the cladding, a release from the pellet of a sufficient quantity of corrosive gases, the presence of a corrosive chemical environment at the clad inner surface.

6.6.1 Stress state

As shown in section 5, three-dimensional simulations give access to the stress state at the triple point where I-SCC failures are usually observed. The triple point is the location of the maximum stresses during the power transient (see Figure 1). The hoop stress gradient across the clad thickness is also particularly high in front of the triple point. The hoop stress at the triple point obtained from 3D simulations has been used directly by Baurens et al. [92] to assess the risk of failure by PCI-SCC.

6.6.2 Chemical form of corrosive gases

The release of inert fission gas is usually integrated in fuel performance codes but few of them actually give an estimation of the other minor gas species that form in the fuel. Generally, the release of different iodine isotopes is considered based on the Release/Birth model [146] [147] and used to estimate the onset of PCI-SCC in the cladding [148] [149]. Some models also account for iodine diffusion in the cladding to define local concentration thresholds for I-SCC initiation/propagation [150] [151]. Attempts have also been made to quantify the recoil implanted iodine

in the cladding, but it was found of no impact on I-SCC compared to diffusional release of iodine [140].

The origin of the iodine involved in PCI has often been attributed to the dominant and most stable component from a thermodynamic point of view, i.e., $CsI_{(g)}$. However, it is well known from laboratory experiments that this iodide compound is not in itself able to provoke I-SCC failures. Dissociation of $CsI_{(s)}$ by gamma radiation radiolysis has been proposed as a possible mechanism leading to the availability of molecular iodine in the vicinity of the clad surface [146] [152] [153] [140] [3]. In the 3D thermo-chemical-mechanical simulations of Baurens et al., four main gas species containing iodine are released from the pellet: $CsI_{(g)}$, $TeI_{2(g)}$, $I_{(g)}$ and $I_{2(g)}$ with $CsI_{(g)}$ as the most abundant gas species (96%) and a 90-10% proportion of $TeI_{2(g)}$ and $I_{(g)}$+$I_{2(g)}$ for the remaining part (4%). The Gibbs energies of the potential reactions of $I_{(g)}$, $I_{2(g)}$, $CsI_{(g)}$ and $TeI_{2(g)}$ with zirconium are plotted in Figure 40 as a function of temperature. Only the reactions having a negative Gibbs energy are thermodynamically favored.

All the reactions considered in Figure 40 lead to the formation of gaseous $ZrI4_{(g)}$, which is generally believed to be at the origin of I-SCC crack initiation [2] [4]. As expected, Figure 40 shows that the formation of $ZrI_{4(g)}$ from $CsI_{(g)}$ is not likely to take place. On the contrary, the formation of $ZrI4_{(g)}$ from $I_{(g)}$ and $I_{2(g)}$ is favored at all temperatures. The reaction between $TeI_{2(g)}$ and zirconium is likely to occur only at temperatures lower than 900 K. The temperature of the pellet-clad interface is close to 700 K meaning that the $TeI_{2(g)}$/Zr reaction is also a possible candidate for I-SCC by $ZrI_{4(g)}$. This raises the question of what part of the released iodine should be considered for I-SCC initiation. A lower bound for a PCI-SCC initiation criterion should at least include the iodine from the corrosive species released by the pellet. This comprises iodine from $TeI_{2(g)}$ and $I_{(g)}$+$I_{2(g)}$ but excludes $CsI_{(g)}$.

6.6.3 Accessibility of the clad inner surface to volatile gases

The third factor for PCI-SCC to occur is the presence of a corrosive chemical environment in the vicinity of the clad inner surface. This actually depends on the accessibility of the clad inner surface to the volatile gases released by the central part of the pellet. In a fractured dished pellet with a chamfer, there are theoretically two possible path for the gases to reach the cladding: the radial cracks and the dish / chamfer voids. The relevant cracks are those formed during base irradiation which usually extend to the pellet center (see section 2.3). Figure 41 gives the calculated opening of the pellet crack on the fracture plane of the 3D fragment model at RTL. It shows that the crack is closed on about half of the pellet radius at MP level and on almost two thirds of the pellet height. On the contrary, the radial crack is opened till the center of the pellet near the pellet ends (IP level). The latter is a consequence of the hourglassing of the fragment which shifts the fragment from the axis of revolution of the pellet and consequently liberates some space between the fragments. Similar results were reported by Klouzal and Dostàl from 3D simulations performed with the FE code ABAQUS [41].

In the 3D simulations of Baurens et al., it was further shown that most of the gas species of interest ($CsI_{(g)}$, $TeI_{2(g)}$, ...) form and are released near pellet ends (dished ends) due to the reduced hydrostatic pressure. Since gas release occurs where the

radial crack opening reaches the pellet center, this could also explain why failure by I-SCC usually takes place in front of pellet cracks and near pellet ends (apart from the stress concentration factor). The calculated maximum half-crack opening at the pellet periphery is close to $15 - 20$ μm which means that the clad surface accessible to iodine will be small. It is well known that size effects are of importance for I-SCC since the flaw size probability distribution function is strongly dependent on the clad surface [2] [150] [148]. A reasonable PCI-SCC initiation criterion should therefore include some quantification of the clad surface accessible to reactive iodine. An estimate of the surface is given by the product of the pellet half-height times the size of the calculated crack aperture.

Finally, the possible condensation of gases on the cooler parts of the pellet has to be considered. Thermochemical calculations show that condensation of $CsI_{(g)}$ starts at a temperature of 1900 K and is complete at 952 K (melting temperature of $CsI_{(s)}$ [154]). On the contrary, $TeI_{2(g)}$, $I_{(g)}$ and $I_{2(g)}$ remain in gaseous state at all temperatures. $CsI_{(g)}$ is therefore likely to condense during its transport from the pellet center to the clad inner surface [92].

6.6.4 PCI-SCC initiation criteria

Baurens et al. proposed a thermo-chemical-mechanical PCI-SCC initiation criterion based on the clad hoop stress at the triple point and the iodine partial pressure in the free volume of the rod [92]. Figure 42 gives the evolution during the simulated ramp of these quantities together with the LHR and the dish filling. Time 0 refers to the beginning of the holding period at RTL. A maximum stress exceeding 500 MPa is reached at IP level approximately 50 seconds before the end of the transient and maintained quasi-constant afterwards. Creep of the pellet due to the high central temperature is at the origin of the levelling of the hoop stress during the transient. Pellet creep leads to dish filling, the evolution of which is consistent with that of the stress (Figure 42). The contribution of gaseous swelling to clad loading then explains the lack of significant clad stress relaxation observed during the holding period.

The evolution of the iodine partial pressure calculated is also plotted in Figure 42. The free volume used to obtain the iodine partial pressure is estimated at each time step from the remaining volume of the pellet dish, the radial crack opening and the plenum volume of the rod divided by the number of pellet fragments in the rodlet. The iodine partial pressure reaches 60 Pa at time -60 s when the hoop stress is maximum and increases tenfold at the end of the transient (time 0 s, $p_I >$ 600 Pa). This result has been compared to the threshold identified in mandrel testing of irradiated zircaloy-2 tubes at 350°C in an anoxic atmosphere, which showed the existence of a reduced I-SCC susceptibility below 60 Pa of iodine partial pressure [155]. The partial iodine pressure was chosen rather than the quantity of iodine per clad surface since dispersion of experimental thresholds in the abundant literature concerned with I-SCC is very high. This is due to the large variability of the experimental conditions explored, mostly as regard temperature and oxygen partial pressure, which are known to be the main parameters in I-SCC of zircaloy.

This 3D simulation was updated by Konarski et al. to include oxygen transport in the fuel pellet [129] [130]. The authors concluded that oxygen redistribution during

the power transient leads to a decrease of the calculated reactive iodine partial pressure in consequence of the higher release of gaseous caesium which favors the formation of stable unreactive $CsI_{(g)}$ in the fuel rod free volume.

7 Modeling of PCI-SCC failure

7.1 Introduction

The development and propagation of cladding cracks related to I-SCC has been studied extensively in out-of-pile experiments. A review of the test conditions and results can be found in references [2] [4] and [3]. The propagation of cracks induced by I-SCC in the thickness of a zircaloy cladding is generally believed to be governed by different mechanisms depending on the cracks' depth:

- a pre-requisite to I-SCC is the breaking of the internal zirconia layer that form on the clad inner surface, with the formation of a radial crack that reach bare zircaloy.
- the subsequent propagation of the radial crack within the bare zircaloy requires the establishment of adequate chemical conditions at the crack tip, often associated to a Van Arkel process with iodine transport in the crack. This mechanism requires time and is usually refered as the incubation period.
- once a proper chemical environment holds at the crack tip, the propagation of cracks by I-SCC is first intergranular, as shown by many SEM observations.
- when the progression within the clad thickness reaches several tens of μm, the intergranular propagation shifts to fast intragranular propagation.
- the last mechanism involves the ductile shear failure of the remaining clad ligament when the crack reaches a few hundreds of μm.

In the present section, only the models developed for I-SCC within or in relation to FE analyses of PCI will be detailed.

7.2 2DRZ PCI-SCC model

In part due to its shortcomings, the 2DRZ model has been scarcely used to study standard PCI failure by I-SCC. A notable exception is the use with the FAST fuel performance code of the model developed by Lewis et al. for PCI-SCC failure [146]. A flow chart reproduced from Oussoren [156] illustrates in Figure 43 the main phenomena considered in the mechanistic modeling of PCI fuel failure by I-SCC.

The model developed by Lewis et al. includes iodine diffusion and release from the bulk of the fuel, an additional iodine release from the fuel surface (a necessary adjustment related to fuel cracking to match the measurements performed on line in CANDU reactors), $CsI_{(s)}$ radiolysis near the fuel pellet periphery to estimate the amount of molecular iodine in the pellet-clad gap, iodine axial diffusion in the gap to the location of the presumed I-SCC crack, instantaneous reaction with the zirconium

alloy provided the hoop strain increment during the power transient (related to the local inter-pellet clad ridges calculated by FAST) is sufficient to break the internal zirconia layer (the threshold is identified from a large database of power ramps), intergranular crack propagation till the stress intensity factor K_I exceeds a critical value K_{ISCC} leading to intragranular propagation and eventually to the ductile failure of the remaining clad ligament if the fracture toughness K_{1C} is exceeded. The approach developed by Oussoren relies on a post-processing of the stresses calculated by FAST, i.e., the progression of the crack in the cladding does not modify the 2DRZ calculation. Linear elastic fracture mechanics is considered to estimate the stress intensity factor. The model includes furthermore a specific axial iodine diffusion process in the gap which is likely to control the failure kinetics. The methodology has been applied to a very large database of power transients performed in CANDU reactors on CANLUB graphite coated and standard fuels leading respectively to a 60 and 80 % failed versus intact prediction accuracy.

7.3 2DRθ PCI-SCC model

Jernkvist proposed a model for predicting PCI failure of fuel rods, based on 2DRθ simulations of a 90° sector of a fuel pellet with a pre-defined radial crack of finite length [148]. The clad and fuel materials are considered elastic, friction is taken into account at the pellet interface. The proposed description accounts for the progressive release of iodine from the fuel pellet by modeling the diffusion of a series of iodine isotopes which are assumed to react instantaneously with the cladding. The I-SCC crack propagation is simulated as a two step process with first, a transgranular progression which kinetics depends on the stress intensity J_I, the temperature T and the iodine concentration at the clad inner wall I:

$$\frac{da}{dt} = CF(I) \left(\frac{J_I}{J_{ISCC}} \right)^n \exp\left(-\frac{Q}{RT} \right) \tag{41}$$

with a the crack depth and Q the activation energy of transgranular cracking. This process is only activated if the stress intensity exceeds a critical threshold J_{ISCC}. The model includes an explicit description of crack propagation in the clad thickness by using a finite element node release technique. Therefore, the stress and displacement fields at the crack tip are continuously assessed during crack propagation within the clad thickness and used to reevaluate the stress intensity J by non-linear fracture mechanics (from the J integral [157]). When the clad fracture toughness J_{1C} is reached, ductile failure is considered until a through-wall crack is calculated. The author showed that the crack propagation depth is very sensitive to the pellet-clad friction coefficient. Jernskvist's model neglects the kinetics associated to iodine transport to the crack tip and the intergranular propagation phase. As can be infered from eq. 41, the model relies on the determination of an initial flaw size. The latter is estimated from a probability distribution function based on Weibull theory, with parameters deduced from surface defects measured on zircaloy samples.

Leboulch et al. considers iodine diffusion within zirconium below the tip of an I-SCC crack as the rate-limiting phenomenon [11]. The transgranular crack

propagation phase is neglected. The authors developed a coupled creep-damage model for the cladding to describe the embrittlement and I-SCC crack propagation [151]. The damage evolution is based on Kachanov's model [158] and includes a dependency on the local iodine content:

$$\dot{d} = A(I).\max\left(\frac{\sigma_{\theta\theta}}{1-d} - \sigma_{\circ}(I); 0\right)^{n(I)} \exp\left(-\frac{Q}{T}\right) \tag{42}$$

with d the damage variable (0 = uncracked, 1 = fully cracked), $A(I)$ and $n(I)$ two parameters that depend on the iodine content. A stress threshold $\sigma_{\circ}$ also dependent on the iodine content is included. The thermo-activation parameter Q, the stress threshold $\sigma_{\circ}$ were identified by Jezekel et al. from pressure tube I-SCC tests saturated in gaseous iodine performed on non-irradiated Zy-4 materials [159]. The extension to irradiated Zy-4 claddings requires the modeling of iodine diffusion at the crack tip within the zircaloy material which is derived from Miller's model [150]:

$$\frac{dI}{dt} = \frac{1}{\tau}(I_{ext} - I) \tag{43}$$

with τ the characteristic time for iodine diffusion at the crack tip, I_{ext} the clad surface iodine content and I the local iodine content in the clad finite elements. In Miller's model, the characteristic time depends on the local hoop strain in the clad element [150]. This coupling is not considered in Leboulch's model [151]. The local damage calculated by eq. 42 is however coupled with the clad viscoplastic behavior law described in section 4.5 by adding a specific crack hoop strain ϵ_{θ}^{f} which evolution is dependent on that of the damage variable:

$$\dot{\epsilon}_{\theta\theta}^{f} = \dot{d}\epsilon_{\theta\theta}^{u} \tag{44}$$

$\epsilon_{\theta\theta}^{u}$ is the critical hoop strain to which corresponds a zero hoop stress. As for the smeared crack model described in section 4.3 and to avoid mesh dependency, the fracture energy associated to I-SCC crack propagation is dependent on the mesh size in the tangentiel direction.

The model was applied by Leboulch et al. to the simulation of I-SCC pressurized tube tests on irradiated Zy-4 samples with or without a pre-formed crack [151]. The time to failure in the initially intact samples and crack propagation velocities in the pre-cracked samples were recovered in 2DRθ simulations of the cladding tube. The model has then been implemented in the 2DRθ scheme of the fuel performance code ALCYONE to study the I-SCC crack propagation in front of an opening radial pellet crack, as illustrated in Figure 44.

8 Conclusions

PCI modeling is a long story which started with the calculation of hoop stresses in the cladding in front of an opening pellet radial crack. While analytical expressions for elastic fuel and clad materials were first derived, the progressive development of computer power led to the enrichment of the original models and the treatment by the Finite Element Method. Among the phenomena that are now available in

multi-dimensional thermo-mechanical modeling of PCI, clad plasticity and creep, fuel creep and cracking, friction at the pellet-clad interface are known to be of primary importance for the evaluation of clad stresses during a power transient. Fuel swelling induced by fission gas has received attention in the past decade and is now fully operational in 2D or 3D models for PCI. In the last years, the release of minor fission products (iodine, tellurium, caesium) that are important for PCI failure by I-SCC has been introduced in the simulations of power transients, based or not on thermochemical calculations of irradiated fuel. The question of the origin of iodine involved in I-SCC of the cladding remains opened, whether related to minor iodide gas species released from the fuel or from the decomposition of solid ceasium iodide formed at the fuel pellet clad interface by gamma radiolysis. Nowadays, with the possible distribution of calculations on several processors, detailed simulations of full rods or full reactor cores are becoming possible. In parallel, very detailed experimental observations are now available that can be used to assess the validity of all the ingredients of the PCI models.

Despite this progress in the modeling of PCI, the distinction between failed and non-failed fuel rods from advanced simulation results is still a challenge. The reasons are multiple: the stochastic nature of fuel cracking during reactor operation makes any deterministic evaluation of clad stresses certainly conservative; the accessibility of iodide gaseous species released from the central part of the fuel pellet to the clad inner surface depends on the pellet radial cracks and the zirconia coverage of the cladding for which detailed characterization are scarse; the I-SCC mechanisms are not fully understood, in particular, the complex chemical-mechanical conditions leading to the initiation or not of a crack are the subject of current research through the development of experiments with a strict control of the chemical environment; the lack of experimental characterization of fuel mechanical properties (creep, plasticity) on irradiated materials which makes simulations highly speculative. For all these reasons, it is a current trend in PCI-SCC simulations that a non-negligible number of non-failed fuel rods exhibit maximum clad stresses during power transients that exceed the stress threshold associated to failed fuel rods. Consequently, many PCI-SCC criteria include a probabilistic treatment to explain the non failure of some rods. Strong limitations of the power maneuvrability in reactor are also a consequence of this general trend.

Improvement of PCI modeling aims primarily at overcoming these limitations and at the understanding of the non-failure of some rods. A more realistic representation of fuel cracking, and in particular the consideration of the stochastic nature of the phenomenon could explain the necessary up-to-now probabilistic treatment of PCI. In this respect, a non-negligible number of papers released in the last years have been concerned with fuel pellet cracking during reactor operations. While a three-dimensional representation of the phenomenon is still a challenge, great progress has been made in 2DRθ modeling. The consideration of internal zirconia formed during irradiation and of evolving friction at the pellet clad interface are important points in view of the low number of PCI failure in high burnup fuel rods. Whether this good behaviour is related to the development of the softer HBS or not is still a pending question. The chemical speciation of iodine with other FPs (tellurium, caesium), its release from the fuel pellet and its interaction with the cladding are

also topics in which more efforts should be devoted since small changes in the fuel composition are likely to change the corrosivity of iodide gaseous species. The importance of oxygen redistribution in the fuel pellet or released from the fuel pellet when initially in excess on PCI-SCC mitigation has been the focus of some recent papers.

Finally, a completely integrated approach in which pellet cladding interaction and the development of I-SCC cracks are fully coupled is still lacking, in spite of the available models. It will certainly be the focus of future developments.

References

[1] N. Waeckel, "General overview of the french effort to address SCC-PCI issues." PCI workshop, Lucca, Italy, 2016.

[2] B. Cox, "Pellet-clad interaction (PCI) failures of zirconium alloy fuel cladding - a review," *Nuclear Engineering and Design*, vol. 186, no. 3, pp. 411–427, 1998.

[3] P. Sidky, "Iodine stress corrosion cracking of Zircaloy reactor cladding: iodine chemistry (a review)," *Journal of Nuclear Materials*, vol. 256, no. 1, pp. 1–17, 1998.

[4] M. H. Piro, D. Sunderland, S. Livingstone, J. Sercombe, W. Revie, A. Quastel, K. Terrani, and C. Judge, "A review of pellet–clad interaction behavior in zirconium alloy fuel cladding," in *Reference Module in Materials Science and Materials Engineering*, Elsevier, 2017.

[5] J. Davies, E. Hoshi, and D. Zimmerman, "Ramp test behavior of high O/U fuel," *Journal of Nuclear Materials*, vol. 270, no. 1-2, pp. 87–95, 1999.

[6] C. Mougel, B. Verhaeghe, C. Verdeau, S. Lansiart, S. Béguin, and B. Julien, "Power ramping in the OSIRIS reactor: database analysis for standard UO_2 fuel with Zy-4 cladding," in *Pellet-clad Interaction in Water Reactor Fuels, Aix-en-Provence*, 2004.

[7] J. Sercombe, M. Agard, C. Struzik, B. Michel, G. Thouvenin, C. Poussard, and K. Kallstrom, "1D and 3D analyses of the Zy2 SCIP BWR ramp tests with the fuel codes METEOR and ALCYONE," *Nuclear Engineering and Technology*, vol. 41, no. 2, pp. 187–198, 2009.

[8] I. Arimescu and J. Karlsson, "Towards understanding beneficial effects of slow power ramps," *Journal of Nuclear Science and Technology*, vol. 52, no. 10, pp. 1274–1280, 2015.

[9] H. Mogard, D. Howl, and M. Grounes, "The international TRANS-RAMP II fuel project—a study of the effects of rapid power ramping on the PCI resistance of PWR fuel," *Proc. ANS Topical Meet. on LWR Fuel Performance, Williamsburg*, p. 232, 1988.

[10] F. Chamiot-Bisson, G. Thellier, S. Loubiere, S. Martin, and P. Ayme, "High power and high speed ramps in the OSIRIS reactor," *TopFuel conference, Salamanca*, vol. 22, p. 122, 2006.

[11] D. Le Boulch, L. Fournier, and C. Sainte-Catherine, "Testing and modelling iodine induced stress corrosion craking in stress relieved zircaloy," in *Pellet-clad Interaction in Water Reactor Fuels, Aix-en-Provence*, OECD, 2004.

[12] S. Bourreau, J. Brochard, F. Bentejac, P. Couffin, C. Verdeau, and S. Lansiard, "Ramp testing of PWR fuel and multi-dimensional finite element modelling of pcmi," in *ANS Topical Meeting on LWR Fuel Performance, Park City*, 2000.

[13] C. Nonon, J. Ménard, S. Lansiart, J. Noirot, S. Martin, G. Decroix, O. Rabouille, C. Delafoy, and B. Petitprez, "PCI behaviour of chromium oxide-doped fuel," in *Pellet-clad Interaction in Water Reactor Fuels, Aix-en-Provence*, 2004.

[14] P. Blanpain, "Recent results from the in reactor MOX fuel performance in France and improvement program," in *Int. Topical Meeting on LWR Fuel Performance, Portland*, 1997.

[15] M. Barker, K. Stephenson, and R. Weston, "The manufacture and performance of homogeneous microstructure SBR MOX fuel," tech. rep., American Nuclear Society, 2007.

[16] B. Julien, C. Delafoy, V. Rebeyrolle, S. Beguin, and S. Lansiard, "Performance of advanced fuel product under PCI conditions," in *ANS topical meeting on LWR fuel performance, Orlando*, 2004.

[17] A. Serres, L. Fournier, M. Frégonèse, Q. Auzoux, and D. Leboulch, "The effect of iodine content and specimen orientation on stress corrosion crack growth rate in Zircaloy-4," *Corrosion Science*, vol. 52, no. 6, pp. 2001–2009, 2010.

[18] A. Soniak, N. L'Hullier, J.-P. Mardon, V. Rebeyrolle, P. Bouffioux, and C. Bernaudat, "Irradiation creep behavior of Zr-based alloys," in *13th Int. Symp. on Zirconium in the Nuclear Industry*, ASTM International, 2002.

[19] J. Sercombe, I. Aubrun, and C. Nonon, "Power ramped cladding stresses and strains in 3D simulations with burnup-dependent pellet–clad friction," *Nuclear Engineering and Design*, vol. 242, pp. 164–181, 2012.

[20] M. Oguma, "Cracking and relocation behavior of nuclear fuel pellets during rise to power," *Nuclear engineering and design*, vol. 76, no. 1, pp. 35–45, 1983.

[21] S. Levy and J. Wilkinson, "A three-dimensional study of nuclear fuel rod behavior during startup," *Nuclear Engineering and Design*, vol. 29, no. 2, pp. 157–166, 1974.

[22] C. Nonon, S. Lansiart, C. Struzik, D. Plancq, S. Martin, G. Decroix, O. Rabouille, S. Beguin, and B. Julien, "Impact of fuel microstructure on

PCI," in *Advanced fuel pellet materials and designs for water cooled reactors, IAEA-TECDOC-1416*, 2003.

[23] B. Michel, J. Sercombe, G. Thouvenin, and R. Chatelet, "3D fuel cracking modelling in pellet cladding mechanical interaction," *Engineering Fracture Mechanics*, vol. 75, no. 11, pp. 3581–3598, 2008.

[24] L. Walton and D. Husser, "Fuel pellet fracture and relocation." Specialists' meeting on fuel element performance computer, Preston, United Kingdom, 15-19 March 1982, 1983.

[25] H. Bailly, D. Menessier, and C. Prunier, *The nuclear fuel of Pressurized Water Reactors and Fast Reactors. Design and behaviour*. Lavoisier Publishing, Paris, France, 1999.

[26] O. Diard, *An example of coupled behavior-damage-environment simulation in polycristals, application to PCI [In French]*. PhD thesis, Ecole des Mines de Paris, 2001.

[27] J. Gittus, "Theoretical analysis of the strains produced in nuclear fuel cladding tubes by the expansion of cracked cylindrical fuel pellets," *Nuclear Engineering and Design*, vol. 18, no. 1, pp. 69–82, 1972.

[28] G. Roberts, "The concentration of stress in cladding produced by the expansion of cracked fuel pellets," *Nuclear Engineering and Design*, vol. 47, no. 2, pp. 257–266, 1978.

[29] G. Ranjan and E. Smith, "Determination of stress within zircaloy cladding due to pellet-cladding interaction," *Nuclear Engineering and Design*, vol. 56, no. 1, pp. 263–272, 1980.

[30] M. Nakatsuka, "Theoretical and experimental analyses of cladding strain produced by expansion of cracked fuel pellets," *Nuclear Engineering and Design*, vol. 65, no. 2, pp. 197–204, 1981.

[31] P. Jackson, "The effect of pellet wheatsheaf growth during power ramps on cladding stress concentration," *Nuclear Engineering and Design*, vol. 101, no. 3, pp. 225–232, 1987.

[32] V. Retel, F. Trivaudey, M. Boubakar, D. Perreux, and P. Thevenin, "Comparative effects of structural and material parameters variability on pellet–cladding interaction in a pwr fuel rod," *Nuclear engineering and design*, vol. 228, no. 1-3, pp. 35–46, 2004.

[33] P. Jackson, J. Turnbull, and R. White, "A description of the enigma fuel performance code." IAEA report IWGFTP/32, 1989.

[34] K. Lassmann, "TRANSURANUS: a fuel rod analysis code ready for use," *Journal of Nuclear Materials*, vol. 188, pp. 295–302, 1992.

[35] P. Garcia, C. Struzik, M. Agard, and V. Louche, "Mono-dimensional mechanical modelling of fuel rods under normal and off-normal operating conditions," *Nuclear engineering and design*, vol. 216, no. 1-3, pp. 183–201, 2002.

[36] J. Yaung, D. Okrent, and A. Wazzan, "A simple computer model of pellet/cladding interaction including stress corrosion cracking," *Nucl. Tech.*, vol. 71, pp. 644 – 650, 1985.

[37] D. Baron, P. Thevenin, R. Largenton, and R. Masson, "CYRANO3 the EDF fuel code performance especially designed for engineering applications," in *Water Reactor Fuel Performance Meeting, Seoul, Corea*, 2008.

[38] N. Muskhelishvili, *Some Basic Problems of the Mathematical Theory of Elasticity, 4th edn.* JRM Radok, Noordhof, Gronigen, 1963.

[39] J. Sercombe, R. Masson, and T. Helfer, "Stress concentration during pellet cladding interaction: Comparison of closed-form solutions with 2D(r,θ) finite element simulations," *Nuclear Engineering and Design*, vol. 260, pp. 175–187, 2013.

[40] Cast3M, "http://www-cast3m.cea.fr/," 2015.

[41] J. Klouzal and M. Dostál, "Modelling of the impact of local effects on fuel-cladding interaction during power ramp," in *22nd International Conference on Nuclear Engineering, ICONE22, Prague*, American Society of Mechanical Engineers, 2014.

[42] J. Sercombe, R. Masson, B. Michel, and C. Nonon, "Impact of fuel pellet properties and friction on stress concentration during PCI: a review of simulation-based results." PCI Seminar, SCIP II meeting, June, 2010.

[43] J. Brochard, F. Bentejac, N. Hourdequin, S. Seror, C. Verdeau, O. Fandeur, S. Lansiart, and P. Verpeaux, "Modelling of pellet cladding interaction in PWR fuel," in *SMiRT 16 conference, Washington DC*, 2001.

[44] O. Diard, S. Leclercq, G. Rousselier, F. Azzouz, and G. Cailletaud, "Modeling of pellet-cladding interaction during power ramps in pressurized water reactors," *Transactions, SMiRT*, vol. 16, 2001.

[45] S. Yagnik, Y. Rashid, R. Dunham, and R. Montgomery, "Fuel analysis and licensing code: Falcon mod01, volume 1: Theoretical and numerical bases." EPRI Palo Alto, CA, 2004.

[46] J. Rashid, S. Yagnik, and R. Montgomery, "Light water reactor fuel performance modeling and multi-dimensional simulation," *JOM*, vol. 63, no. 8, p. 81, 2011.

[47] N. Capps, M. Kennard, W. Liu, B. Wirth, and J. Rashid, "PCI analysis of a commercial PWR using BISON fuel performance code," *Nuclear Engineering and Design*, vol. 324, pp. 131–142, 2017.

[48] R. Williamson, "Simulating dynamic fracture in oxide fuel pellets using cohesive zone models," in *TopFuel conference, Paris*, 2009.

[49] M. Dostál, J. Klouzal, A. Krupkin, V. Kuznetzov, and S. Linhart, "3D modelling of VVER fuel pellet cracking during power ramp." International conference on WWER fuel performance, modelling and experimental support, Sandanski, Bulgaria, 2013.

[50] T. Haynes, J. Ball, and M. Wenman, "Modelling the role of pellet crack motion in the (r-θ) plane upon pellet-clad interaction in advanced gas reactor fuel," *Nuclear Engineering and Design*, vol. 314, pp. 271–284, 2017.

[51] H. Huang, B. Spencer, and J. Hales, "Discrete element method for simulation of early-life thermal fracturing behavior in ceramic nuclear fuel pellets," *Nuclear Engineering and Design*, vol. 278, pp. 515–528, 2014.

[52] S. Oterkus and E. Madenci, "Peridynamic modeling of fuel pellet cracking," *Engineering Fracture Mechanics*, vol. 176, pp. 23–37, 2017.

[53] J. Pacull, "2D and 3D simulations of fuel pellet cracking with cohesive zones. application to PCI [in french]," 2007.

[54] B. Michel, T. Helfer, I. Ramière, and C. Esnoul, "A new numerical methodology for simulation of unstable crack growth in time independent brittle materials," *Engineering Fracture Mechanics*, vol. 188, pp. 126–150, 2018.

[55] L. Jernkvist, "A continuum model for cracked UO_2 fuel," *Nuclear Engineering and Design*, vol. 176, no. 3, pp. 273–284, 1997.

[56] T. Helfer, B. Michel, J.-M. Proix, M. Salvo, J. Sercombe, and M. Casella, "Introducing the open-source mfront code generator: Application to mechanical behaviours and material knowledge management within the PLEIADES fuel element modelling platform," *Computers & Mathematics with Applications*, vol. 70, no. 5, pp. 994–1023, 2015.

[57] N. Marchal, C. Campos, and C. Garnier, "Finite element simulation of Pellet-Cladding Interaction (PCI) in nuclear fuel rods," *Computational Materials Science*, vol. 45, no. 3, pp. 821–826, 2009.

[58] A. Evans and R. Davidge, "The strength and fracture of stoichiometric polycrystalline UO_2," *Journal of Nuclear Materials*, vol. 33, no. 3, pp. 249–260, 1969.

[59] R. F. Canon, J. T. A. Roberts, and R. J. Beals, "Deformation of UO_2 at high temperatures," *Journal of the American Ceramic Society*, vol. 54, no. 2, pp. 105–112, 1971.

[60] K. Radford, "Effect of fabrication parameters and microstructure on the mechanical strength of UO_2 fuel pellets," *Journal of Nuclear Materials*, vol. 84, pp. 222–236, 1979.

[61] A. Hillerborg, M. Modéer, and P.-E. Petersson, "Analysis of crack formation and crack growth in concrete by means of fracture mechanics and finite elements," *Cement and concrete research*, vol. 6, no. 6, pp. 773–781, 1976.

[62] J.-M. Gatt, J. Sercombe, I. Aubrun, and J.-C. Ménard, "Experimental and numerical study of fracture mechanisms in UO_2 nuclear fuel," *Engineering Failure Analysis*, vol. 47, pp. 299–311, 2015.

[63] M. Salvo, J. Sercombe, J.-C. Ménard, J. Julien, T. Helfer, and T. Désoyer, "Experimental characterization and modelling of UO_2 behavior at high temperatures and high strain rates," *Journal of Nuclear Materials*, vol. 456, pp. 54–67, 2015.

[64] M. Salvo, J. Sercombe, T. Helfer, P. Sornay, and T. Désoyer, "Experimental characterization and modeling of uo 2 grain boundary cracking at high temperatures and high strain rates," *Journal of Nuclear Materials*, vol. 460, pp. 184–199, 2015.

[65] M. S. Seltzer, J. S. Perrin, A. H. Clauer, and B. A. Wilcox, "Review of creep behavior of ceramic nuclear fuels.," *Reactor Technology*, vol. 14, no. 2, pp. 99–135, 1971.

[66] Y. Monerie and J.-M. Gatt, "Overall viscoplastic behavior of non-irradiated porous nuclear ceramics," *Mechanics of Materials*, vol. 38, pp. 608–619, July 2006.

[67] Y. Rashid, H. Tang, and E. Johansson, "Mathematical treatment of hot pressing of reactor fuel," *Nuclear Engineering and Design*, vol. 29, no. 1, pp. 1–6, 1974.

[68] M. Le Saux, J. Besson, S. Carassou, C. Poussard, and X. Averty, "A model to describe the anisotropic viscoplastic mechanical behavior of fresh and irradiated Zy-4 fuel claddings under RIA loading conditions," *Journal of Nuclear Materials*, vol. 378, no. 1, pp. 60–69, 2008.

[69] T. Tachibana, D. Narita, H. Kaneko, and Y. Honda, "Measurement of the friction coefficient between UO_2 and cladding tube," Tech. Rep. PNCT–831-78-02, Power Reactor and Nuclear Fuel Development Corporation, Tokai Works, 1978.

[70] N. Nakatsuka, "Measurements of the coefficient of friction between UO_2 and Al_2O_3 pellets and unirradiated zircaloy cladding," *Journal of Nuclear Materials*, vol. 96, pp. 205–207, 1981.

[71] V. Shchavelin, A. Kostochka, A. Kuznetsov, I. Golovnin, and Y. K. Bibilashvili, "In-reactor study of the friction characteristics of reactor materials," *Soviet Atomic Energy*, vol. 61, no. 3, pp. 686–690, 1986.

[72] Y. V. Bozhko, A. Bolobolichev, A. Kostochka, and V. Shchavelin, "The research of the behaviour of static coefficient of uranium dioxide-zirconium alloy pair under irradiation," *Atomnaya Ehnergiya*, vol. 71, no. 5, pp. 463–466, 1991.

[73] V. M. Baranov, E. M. Kudryavtsev, G. A. Sarychev, and V. M. Schavelin, *Acoustic emission in friction*, vol. 53. Elsevier, 2011.

[74] L. Desgranges, "Internal corrosion layer in PWR fuel." OECD Seminar on Thermal Performance of High Burn-Up LWR Fuel, Cadarache, France, 1998.

[75] J.-B. Minne, L. Desgranges, V. Optasanu, N. Largenton, L. Raceanu, and T. Montesin, "Specific aspects of internal corrosion of nuclear clad made of Zircaloy," in *Defect and Diffusion Forum*, vol. 323, pp. 227–232, Trans Tech Publ, 2012.

[76] C. Walker, W. Goll, and T. Matsumura, "Further observations on OCOM MOX fuel: microstructure in the vicinity of the pellet rim and fuel—cladding interaction," *Journal of Nuclear Materials*, vol. 245, no. 2-3, pp. 169–178, 1997.

[77] S. K. Yagnik, A. J. Machiels, and R. L. Yang, "Characterization of UO_2 irradiated in the BR-3 reactor1," *Journal of Nuclear Materials*, vol. 270, no. 1-2, pp. 65–73, 1999.

[78] S. Van den Berghe, A. Leenaers, B. Vos, L. Sannen, and M. Verwerft, "Observation of a pellet-cladding bonding layer in high power fuel," in *Pellet-clad Interaction in Water Reactor Fuels, Aix-en-Provence*, OECD, 2005.

[79] J. Noirot, L. Desgranges, and J. Lamontagne, "Detailed characterisations of high burn-up structures in oxide fuels," *Journal of Nuclear Materials*, vol. 372, no. 2-3, pp. 318–339, 2008.

[80] J. Noirot, I. Aubrun, L. Desgranges, K. Hanifi, J. Lamontagne, B. Pasquet, C. Valot, P. Blanpain, and H. Cognon, "High Burnup changes in UO_2 fuels irradiated up to 83 GWd/t in M5 claddings," *Nuclear Engineering and Technology*, vol. 41, no. 2, pp. 155–162, 2009.

[81] C. Ciszak, M. Mermoux, S. Miro, G. Gutierrez, F. Lepretre, I. Popa, K. Hanifi, I. Zacharie-Aubrun, L. Fayette, and S. Chevalier, "Micro-Raman analysis of the fuel-cladding interface in a high burnup PWR fuel rod," *Journal of Nuclear Materials*, vol. 495, pp. 392–404, 2017.

[82] K. Nogita and K. Une, "Formation of pellet-cladding bonding layer in high burnup BWR fuels," *Journal of Nuclear Science and Technology*, vol. 34, no. 7, pp. 679–686, 1997.

[83] K. Tanaka, K. Maeda, S. Sasaki, Y. Ikusawa, and T. Abe, "Fuel–cladding chemical interaction in MOX fuel rods irradiated to high burnup in an advanced thermal reactor," *Journal of Nuclear Materials*, vol. 357, no. 1-3, pp. 58–68, 2006.

[84] M. Suzuki, K. Kusagaya, H. Saitou, and T. Fuketa, "Analysis on lift-off experiment in Halden reactor by FEMAXI-6 code," *Journal of Nuclear Materials*, vol. 335, no. 3, pp. 417–424, 2004.

[85] M. Suzuki, H. Uetsuka, and H. Saitou, "Analysis of mechanical load on cladding induced by fuel swelling during power ramp in high burn-up rod by fuel performance code FEMAXI-6," *Nuclear Engineering and Design*, vol. 229, no. 1, pp. 1–14, 2004.

[86] N. Capps, R. Montgomery, D. Sunderland, M. Pytel, and B. Wirth, "Evaluation of missing pellet surface geometry on cladding stress distribution and magnitude," *Nuclear Engineering and Design*, vol. 305, pp. 51–63, 2016.

[87] W. Lyon, R. Montgomery, and J. Rashid, "PCI analysis and fuel rod failure prediction using FALCON." TopFuel conference, Paris, 2009.

[88] N. Hourdequin, *Modeling of the PWR fuel mechanical behaviour and particularly study of the pellet-cladding interaction in a fuel rod [In French]*. PhD thesis, Châtenay-Malabry, Ecole centrale de Paris, 1995.

[89] F. Bentejac and N. Hourdequin, "TOUTATIS: an application of the Cast3M Finite Element Code for PCI three-dimensional modelling," in *Pellet-Clad Interaction in Water Reactor Fuels, Aix-en-Provence*, 2004.

[90] B. Michel, D. Plancq, C. Struzik, P. Garcia, and S. Lansiart, "PCMI assessment using 3D modelling," in *18th SMIRT conference, Beijing*, 2005.

[91] B. Michel, C. Nonon, J. Sercombe, F. Michel, and V. Marelle, "Simulation of pellet-cladding interaction with the PLEIADES fuel performance software environment," *Nuclear Technology*, vol. 182, no. 2, pp. 124–137, 2013.

[92] B. Baurens, J. Sercombe, C. Riglet-Martial, L. Trotignon, and P. Maugis, "3D thermo-chemo-mechanical simulation of power ramps with ALCYONE," *Journal of Nuclear Materials*, vol. 452, pp. 518–594, 2014.

[93] C. Newman, G. Hansen, and D. Gaston, "Three dimensional coupled simulation of thermomechanics, heat, and oxygen diffusion in UO_2 nuclear fuel rods," *Journal of Nuclear Materials*, vol. 392, no. 1, pp. 6–15, 2009.

[94] R. Williamson, J. Hales, S. Novascone, M. Tonks, D. Gaston, C. Permann, D. Andrs, and R. Martineau, "Multidimensional multiphysics simulation of nuclear fuel behavior," *Journal of Nuclear Materials*, vol. 423, no. 1-3, pp. 149–163, 2012.

[95] B. Spencer, R. Williamson, D. Stafford, S. Novascone, J. Hales, and G. Pastore, "3D modeling of missing pellet surface defects in BWR fuel," *Nuclear Engineering and Design*, vol. 307, pp. 155–171, 2016.

[96] R. Williamson, N. Capps, W. Liu, Y. Rashid, and B. Wirth, "Multidimensional simulation of LWR fuel behavior in the BISON fuel performance code," *JOM*, vol. 68, no. 11, pp. 2930–2937, 2016.

[97] G. Pastore, C. Folsom, R. Williamson, J. Hales, L. Luzzi, D. Pizzocri, and T. Barani, "Modeling fission gas behaviour with the BISON fuel performance

code," tech. rep., Idaho National Lab.(INL), Idaho Falls, ID (United States), 2017.

[98] J. Sercombe, B. Michel, G. Thouvenin, B. Petitprez, R. Chatelet, D. Leboulch, and C. Nonon, "Multi-dimensional modeling of PCMI during base irradiation and ramp testing with ALCYONE V1.1," in *TopFuel conference*, (Seoul, Korea), 2009.

[99] P. Garcia, C. Struzik, and M. Moyne, "The effect of gas swelling on cladding strains during power ramp tests." Proc. of the IAEA Technical Commitee Meeting, Nykoping, Sweden, 1998.

[100] K. Clarno, B. Philip, W. Cochran, R. Sampath, S. Allu, P. Barai, S. Simunovic, M. Berrill, L. Ott, S. Pannala, *et al.*, "The AMP (advanced multiphysics) nuclear fuel performance code," *Nuclear Engineering and Design*, vol. 252, pp. 108–120, 2012.

[101] I. Ramière and T. Helfer, "Iterative residual-based vector methods to accelerate fixed point iterations," *Computers & Mathematics with Applications*, vol. 70, no. 9, pp. 2210–2226, 2015.

[102] L. Noirot, "Margaret: A comprehensive code for the description of fission gas behavior," *Nuclear Engineering and Design*, vol. 241, no. 6, pp. 2099–2118, 2011.

[103] G. Jomard, C. Struzik, A. Boulore, P. Mailhé, V. Auret, and R. Largenton, "CARACAS: An industrial model for the description of fission gas behavior in LWR-UO_2 fuel," in *TopFuel conference, Sendai*, 2014.

[104] G. Pastore, L. Swiler, J. Hales, S. Novascone, D. Perez, B. Spencer, L. Luzzi, P. Van Uffelen, and R. Williamson, "Uncertainty and sensitivity analysis of fission gas behavior in engineering-scale fuel modeling," *Journal of Nuclear Materials*, vol. 456, pp. 398–408, 2015.

[105] T. Barani, E. Bruschi, D. Pizzocri, G. Pastore, P. Van Uffelen, R. Williamson, and L. Luzzi, "Analysis of transient fission gas behaviour in oxide fuel using BISON and TRANSURANUS," *Journal of Nuclear Materials*, vol. 486, pp. 96–110, 2017.

[106] G. Khvostov, K. Mikityuk, and M. Zimmermann, "A model for fission gas release and gaseous swelling of the uranium dioxide fuel coupled with the FALCON code," *Nuclear Engineering and Design*, vol. 241, no. 8, pp. 2983–3007, 2011.

[107] A. Prudil, B. Lewis, P. Chan, and J. Baschuk, "Development and testing of the fast fuel performance code: Normal operating conditions (part 1)," *Nuclear Engineering and Design*, vol. 282, pp. 158–168, 2015.

[108] J. Julien, C. Bassi, and C. Struzik, "ALCYONE calculations of GONCOR experiment for the kinetics of gaseous swelling during a power transient."

OECD/NEA Workshop on Nuclear-fuel modelling to support safety and performance enhancement for water-cooled reactors, Paris, 2017.

[109] J. Sercombe, J. Julien, F. Michel, B. Michel, and E. Fédérici, "3D modelling of strain concentration due to PCI within the fuel code alcyone," in *TopFuel conference, Charlotte*, 2013.

[110] J. Desquines, "Contribution à l'analyse de la rupture des composants mécaniques polycristallins.." Mémoire d'Habilitation à Diriger des Recherches, 2015.

[111] J. Julien, I. Zacharie-Aubrun, J. Sercombe, G. Raveu, and J. Gatt, "Adjustement of fuel creep behavior based on post-ramp dish filling observations and 3D simulations. impact on clad ridges.." TopFuel conference, Manchester, UK, 2012.

[112] E. Fédérici and J. Sercombe, "Pellet-cladding interaction: involved phenomena and recent progress [in french]," *Revue Générale Nucléaire*, no. 6, pp. 61–66, 2013.

[113] E. Fédérici, "Recent advances in the understanding of the physical mechanisms involved in pci i–scc and their modeling with alcyone application." PCI Workshop, Lucca, Italy, 2016.

[114] B. Michel, J. Sercombe, and G. Thouvenin, "A new phenomenological criterion for pellet–cladding interaction rupture," *Nuclear Engineering and Design*, vol. 238, no. 7, pp. 1612–1628, 2008.

[115] S. Lansiard and B. Miche, *Pellet-cladding interaction.* Nuclear Fuels, a Nuclear Energy Division monograph, 2009.

[116] K. Ito, M. Ichikawa, T. Okubo, and Y. t. Iwano, "Femaxi-iii, a computer code for fuel rod performance analysis," *Nuclear engineering and design*, vol. 76, no. 1, pp. 3–11, 1983.

[117] T. Helfer, P. Garcia, J. Ricaud, D. Plancq, F. Sidoroff, and L. Bernard, "Modelling the effect of oxide fuel fracturing on the mechanical behaviour of fuel rods," in *Pellet-clad Interaction in Water Reactor Fuels, Aix-en-Provence*, 2005.

[118] Y. Rashid, "Mathematical modeling and analysis of fuel rods," *Nuclear Engineering and Design*, vol. 29, no. 1, pp. 22–32, 1974.

[119] T. Helfer, E. Castelier, and P. Garcia, "Two-dimensional modeling of PWR fuel rods. analysis of fuel cracking," in *European Mechanics of Materials Conference, Moret-sur-Loing, France*, 2006.

[120] T. Helfer, *Impact of fuel pellet cracking on the behavior of fuel rods during normal and off-normal in-reactor conditions [In French].* PhD thesis, Ecole centrale de Lyon, France, 2006.

[121] J. Arborelius, K. Backman, L. Hallstadius, M. Limbaeck, J. Nilsson, B. Rebensdorff, G. Zhou, K. Kitano, R. Loefstroem, and G. Roennberg, "Advanced doped UO_2 pellets in LWR applications," *Journal of Nuclear Science and Technology*, vol. 43, no. 9, pp. 967–976, 2006.

[122] C. Delafoy, P. Dewes, and T. Miles, "AREVA NP Cr_2O_3-doped fuel development for BWRs," in *TopFuel conference, San Francisco*, 2007.

[123] K. Backman, L. Hallstadius, and G. Roennberg, "Westinghouse advanced doped pellet-characteristics and irradiation behaviour," in *Technical Meeting on Advanced Fuel Pellet Materials and Fuel Rod Designs for Water Cooled Reactors, Villigen, Switzerland*, 2009.

[124] J. Matsunaga, Y. Takagawa, K. Kusagaya, K. Une, R. Yuda, and M. Hirai, "Fundamentals of GNF Al-Si-O additive fuel." TopFuel conference, Paris, 2009.

[125] C. Walker, V. Rondinella, D. Papaioannou, S. Van Winckel, W. Goll, and R. Manzel, "On the oxidation state of UO_2 nuclear fuel at a burn-up of around 100 MWd/kgHM," *Journal of Nuclear Materials*, vol. 345, no. 2, pp. 192–205, 2005.

[126] M. Piro, J. Banfield, K. Clarno, S. Simunovic, T. Besmann, B. Lewis, and W. Thompson, "Coupled thermochemical, isotopic evolution and heat transfer simulations in highly irradiated UO_2 nuclear fuel," *Journal of Nuclear Materials*, vol. 441, no. 1, pp. 240–251, 2013.

[127] S. Simunovic, J. McMurray, T. Besmann, E. Moore, and M. Piro, "Coupled mass and heat transport models for nuclear fuels using thermodynamic calculations," tech. rep., Oak Ridge National Laboratory, ORNL/TM-2018/2, 2018.

[128] J. Sercombe, C. Riglet-Martial, and B. Baurens, "Simulations of power ramps with alcyone including fission products chemistry and oxygen thermodiffusion," in *Pellet-Clad Interaction (PCI) in Water-Cooled Reactors*, NEA/CSNI/R(2018)9, 2018.

[129] P. Konarski, J. Sercombe, C. Riglet-Martial, L. Noirot, I. Zacharie-Aubrun, M. Frégonèse, and P. Chantrenne, "3D simulation of a power ramp including fuel thermochemistry and oxygen thermodiffusion." TopFuel conference, Prague, 2018.

[130] P. Konarski, J. Sercombe, C. Riglet-Martial, L. Noirot, I. Zacharie-Aubrun, K. Hanifi, M. Frégonèse, and P. Chantrenne, "3D simulation of a power ramp including fuel thermochemistry and oxygen thermodiffusion," *Journal of Nuclear Materials*, vol. In Press, 2019.

[131] G. Eriksson, "Thermodynamic studies of high-temperature equilibriums. iii. solgas, a computer program for calculating the composition and heat condition of an equilibrium mixture," *Acta Chemica Scandinavica*, vol. 25, pp. 2651–2658, 1971.

[132] W. Thompson, B. Lewis, E. Corcoran, M. Kaye, S. White, F. Akbari, Z. He, R. Verrall, J. Higgs, D. Thompson, *et al.*, "Thermodynamic treatment of uranium dioxide based nuclear fuel," *International Journal of Materials Research*, vol. 98, no. 10, pp. 1004–1011, 2007.

[133] M. Piro, *Computation of thermodynamic equilibria pertinent to nuclear materials in multi-physics codes*. PhD thesis, Royal Military College of Canada (Canada), 2011.

[134] H. Loukusa, "Computational module for the calculation of thermochemical equilibria in nuclear fuel." Master thesis, VTT, Finland., 2014.

[135] E. Corcoran, M. Kaye, and M. Piro, "An overview of thermochemical modelling of candu fuel and applications to the nuclear industry," *Calphad*, vol. 55, pp. 52–62, 2016.

[136] T. M. Besmann, J. W. McMurray, and S. Simunovic, "Application of thermochemical modeling to assessment/evaluation of nuclear fuel behavior," *Calphad*, vol. 55, pp. 47–51, 2016.

[137] `https://www.oecd-nea.org/science/taf-id/`.

[138] L. Desgranges, C. Riglet-Martial, I. Aubrun, B. Pasquet, I. Roure, J. Lamontagne, and T. Blay, "Evidence of tellurium iodine coumpounds in a power-ramped irradiated UO_2 fuel rod.," *Journal of Nuclear Materials*, vol. 437, pp. 409–414, 2013.

[139] H. Loukusa, T. Ikonen, V. Valtavirta, and V. Tulkki, "Thermochemical modeling of nuclear fuel and the effects of oxygen potential buffers," *Journal of Nuclear Materials*, vol. 481, pp. 101–110, 2016.

[140] M. Frégonèse, G. Delette, G. Ducros, and F. Lefebvre, "Amount of iodine responsible for I-SCC of Zircaloy-4 in PCI-conditions: recoil-implanted and thermally released iodine," *Nuclear Engineering and Design*, vol. 186, no. 3, pp. 307–322, 1998.

[141] V. Ozrin, "A model for evolution of oxygen potential and stoichiometry deviation in irradiated UO_2 fuel," *Journal of Nuclear Materials*, vol. 419, no. 1, pp. 371–377, 2011.

[142] Y. Pontillon, G. Ducros, and P. Malgouyres, "Behaviour of fission products under severe PWR accident conditions VERCORS experimental programme—part 1: General description of the programme," *Nuclear Engineering and Design*, vol. 240, no. 7, pp. 1843–1852, 2010.

[143] Y. Pontillon and G. Ducros, "Behaviour of fission products under severe pwr accident conditions: The vercors experimental programme—part 2: Release and transport of fission gases and volatile fission products," *Nuclear engineering and design*, vol. 240, no. 7, pp. 1853–1866, 2010.

[144] Y. Pontillon, E. Geiger, C. Le Gall, S. Bernard, A. Gallais-During, P. Malgouyres, E. Hanus, and G. Ducros, "Fission products and nuclear fuel behaviour under severe accident conditions part 1: Main lessons learnt from the first verdon test," *Journal of Nuclear Materials*, vol. 495, pp. 363–384, 2017.

[145] M. Veshchunov, R. Dubourg, V. Ozrin, V. Shestak, and V. Tarasov, "Mechanistic modelling of urania fuel evolution and fission product migration during irradiation and heating," *Journal of Nuclear Materials*, vol. 362, no. 2, pp. 327–335, 2007.

[146] B. Lewis, W. Thompson, M. Kleczek, K. Shaheen, M. Juhas, and F. Iglesias, "Modelling of iodine-induced stress corrosion cracking in CANDU fuel," *Journal of Nuclear Materials*, vol. 408, no. 3, pp. 209–223, 2011.

[147] C. Beyer and A. Turnbull, "Background and derivation of ANS-5.4 standard fission product release model," tech. rep., Pacific Northwest National Lab.(PNNL), Richland, WA (United States), 2010.

[148] L. Jernkvist, "A model for predicting pellet-cladding interaction-induced fuel rod failure," *Nuclear Engineering and Design*, vol. 156, no. 3, pp. 393–399, 1995.

[149] G. Zhou, J. Lindback, H. Schutte, L. Jernkvist, and A. Massih, "Modeling of pellet-clad interaction during power ramps," in *Pellet-clad Interaction in Water Reactor Fuels Seminar Proceedings*, 2004.

[150] A. Miller, H. Ocken, and A. Tasooji, "Iodine Stress Corrosion Cracking of Zircaloy: laboratory data, a phenomenological model, and predictions of in-reactor behavior." Journal of Nuclear Materials, 1981.

[151] D. Le Boulch, "Testing and modelling iodine-induced stress corrosion cracking in zircaloy alloys." PCI Workshop, Lucca, Italy, 2016.

[152] K. Konashi, K. Kamimura, and Y. Yokouchi, "Estimation of irradiation induced iodine pressure in an LWR fuel rod," *Journal of Nuclear Materials*, vol. 125, pp. 244–247, 1984.

[153] K. Konashi, Y. Shiokawa, and H. Kayano, "Simulation of CsI decomposition in fuel cladding gap," *Journal of Nuclear Materials*, vol. 232, no. 2-3, pp. 181–185, 1996.

[154] E. Cordfunke and R. Konings, "Thermochemical data for reactor materials and fission products: the ECN database," *Journal of phase equilibria*, vol. 14, no. 4, pp. 457–464, 1993.

[155] C. Anghel, A.-M. Holston, G. Lysell, S. Karlsson, R. Jakobsson, J. Flygare, S. Mahmood, D. Le Boulch, and I. Arimescu, "Experimental and finite element modeling parametric study for iodine-induced stress corrosion cracking of irradiated cladding," *TopFuel conference, Orlando, US*, 2010.

[156] A. Oussoren, "Towards a mechanistic model for stress corrosion cracking in nuclear fuel elements." Master thesis, Royal Military College of Canada, 2015.

[157] J. R. Rice, "A path independent integral and the approximate analysis of strain concentration by notches and cracks," *Journal of applied mechanics*, vol. 35, no. 2, pp. 379–386, 1968.

[158] L. Kachanov, "Rupture time under creep conditions," *International Journal of Fracture*, vol. 97, no. 1-4, pp. 11–18, 1999.

[159] T. Jezequel, Q. Auzoux, D. Le Boulch, M. Bono, E. Andrieu, C. Blanc, V. Chabretou, N. Mozzani, and M. Rautenberg, "Stress corrosion crack initiation of zircaloy-4 cladding tubes in an iodine vapor environment during creep, relaxation, and constant strain rate tests," *Journal of Nuclear Materials*, vol. 499, pp. 641–651, 2018.

[160] P. Lucuta, H. Matzke, and I. Hastings, "A pragmatic approach to modelling thermal conductivity of irradiated UO_2 fuel: review and recommendations," *Journal of Nuclear Materials*, vol. 232, no. 2-3, pp. 166–180, 1996.

[161] D. Martin, "The thermal expansion of solid UO_2 and (U, Pu) mixed oxides—a review and recommendations," *Journal of Nuclear Materials*, vol. 152, no. 2-3, pp. 94–101, 1988.

[162] D. Martin, "The elastic constants of polycrystalline UO2 and (U, Pu) mixed oxides: a review and recommendations," *High Temperatures. High Pressures*, vol. 21, no. 1, pp. 13–24, 1989.

[163] "MATPRO - a library of MATerials PROperties for Light Water Reactor accident analysis," tech. rep., NUREG/CR-6150 Vol. 4, 1997.

[164] I. Palmer, K. Hesketh, and P. Jackson, "A model for predicting the radial power profile in a fuel pin." Proc. IAEA Meeting on LWR fuel performance, Orlando, 1983.

[165] K. Lassmann and F. Hohlefeld, "The revised URGAP model to describe the gap conductance between fuel and cladding," *Nuclear Engineering and Design*, vol. 103, no. 2, pp. 215–221, 1987.

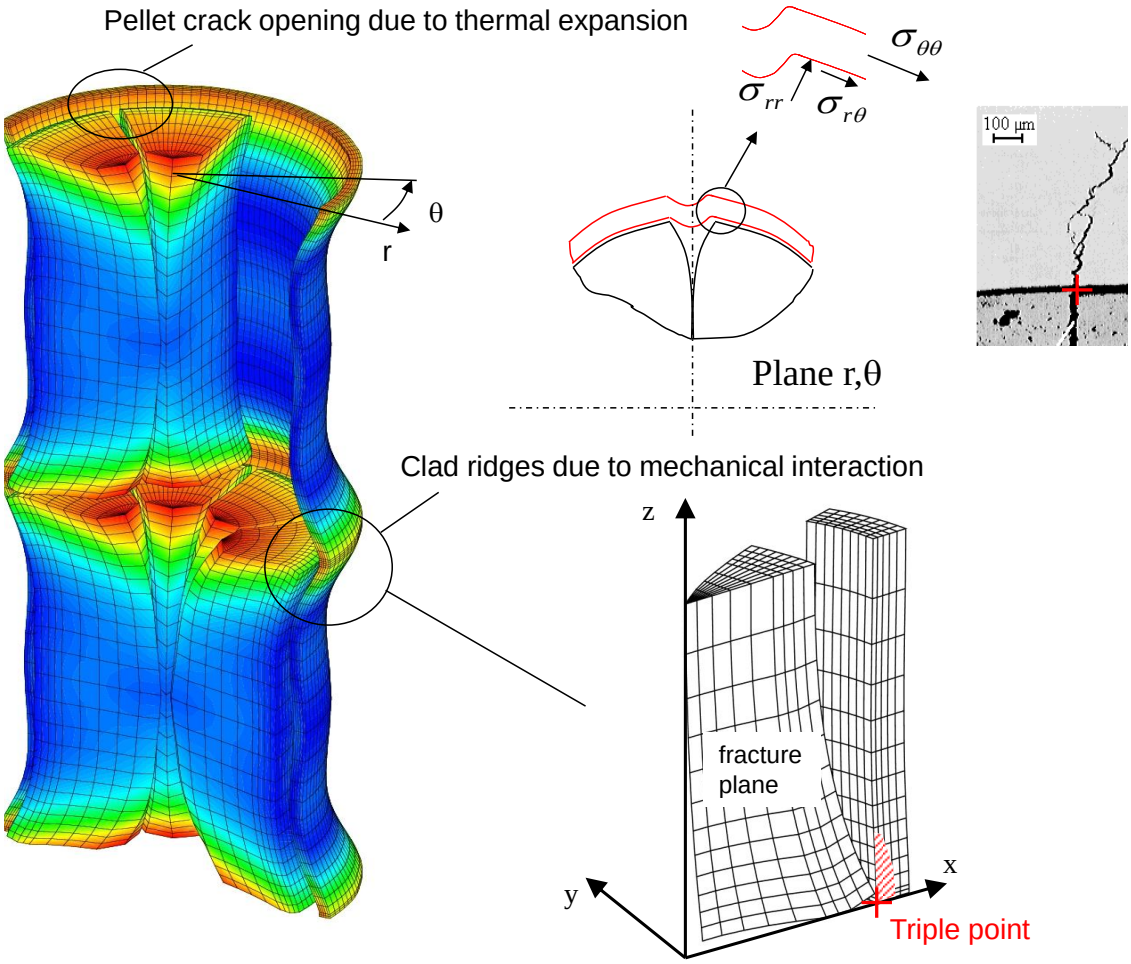

Figure 1: Stress and strain localization in the cladding in front of main cracks in the pellet. Clading with ridges in front of pellet ends in consequence of pellet non uniform radial deformation. Location of the triple point.

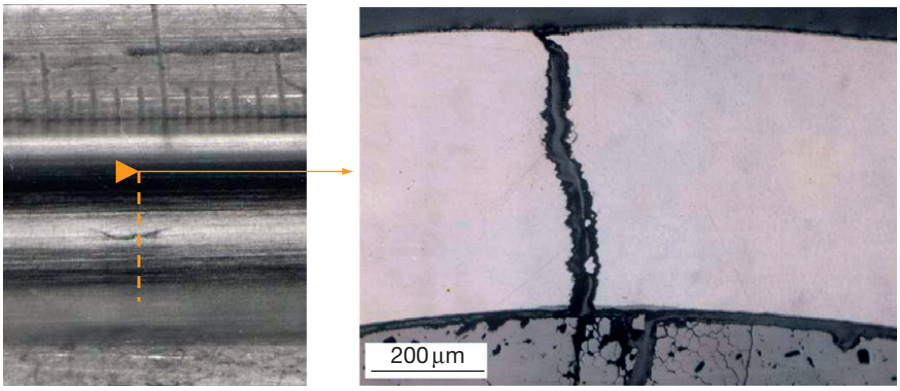

Figure 2: Typical I-SCC failure after a power ramp. a) Axial crack observed on the external surface of the cladding. b) I-SCC crack observed on a fuel cross-section near the pellet-pellet interface.

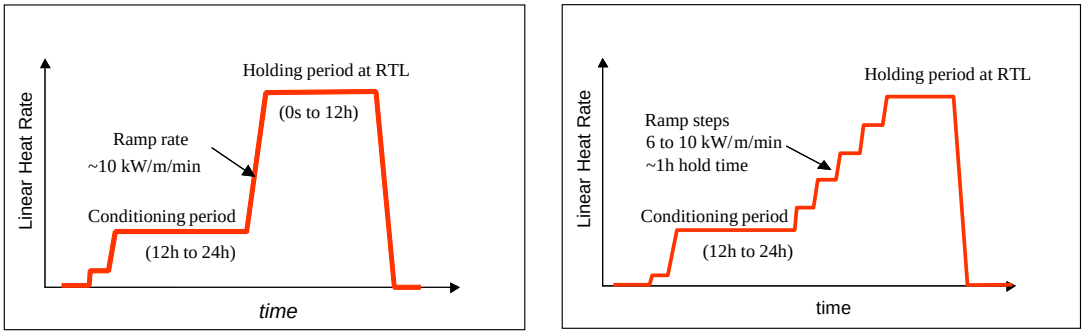

Figure 3: Typical power ramp test sequence (top: staircase, bottom: single step).

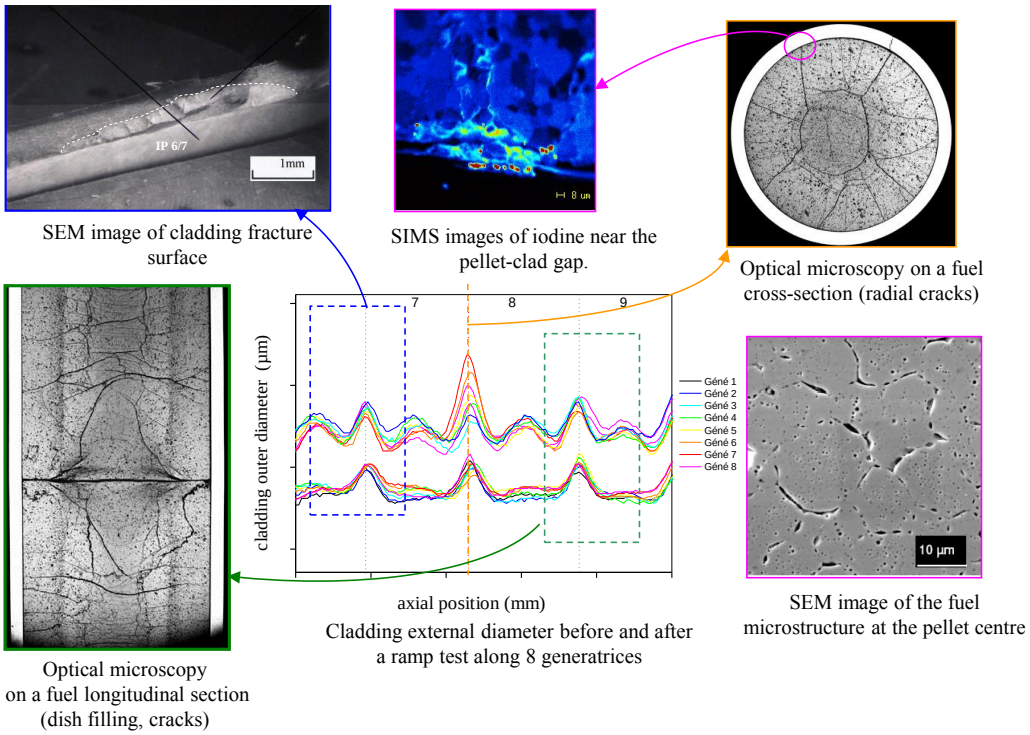

Figure 4: PIE on a PWR fuel rod performed before and after a power ramp.

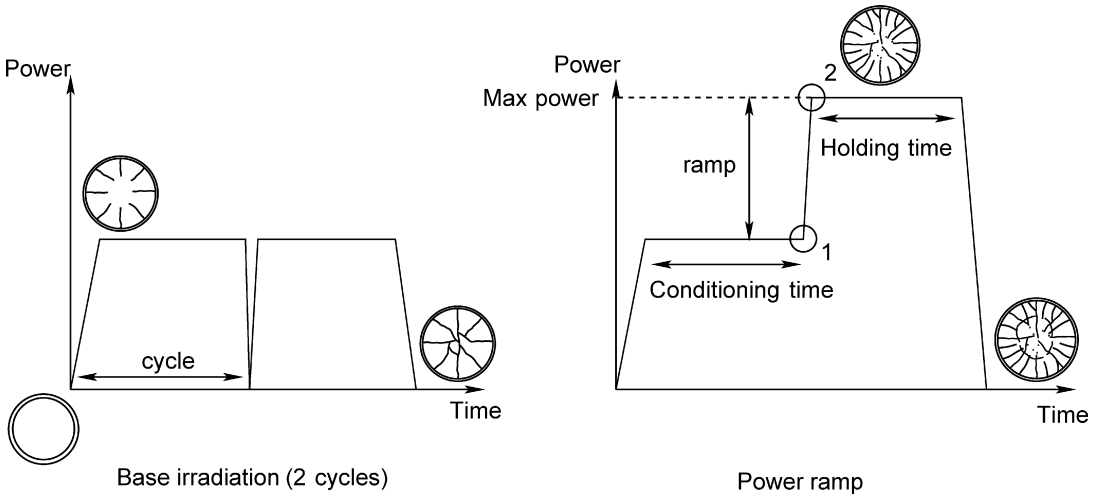

Figure 5: Irradiation history and pellet radial crack pattern during normal (base irradiation), and off-normal (power ramps) operating conditions, reproduced from [19].

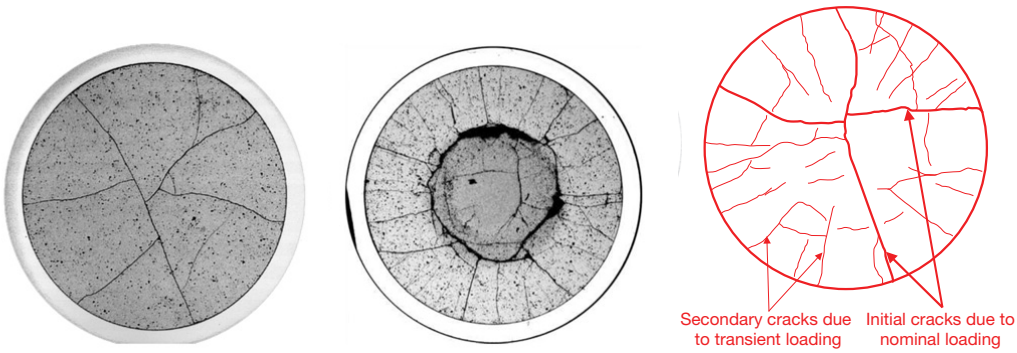

Figure 6: Cross-sections of UO_2 fuel pellets after irradiation in a commercial PWR reactor up to an average burnup of 25 GWd/tU (left) and after a power ramp test with a 12h holding period, reproduced from [22] (middle). Separation of primary and secondary radial cracks after a power ramp, reproduced from [23](right).

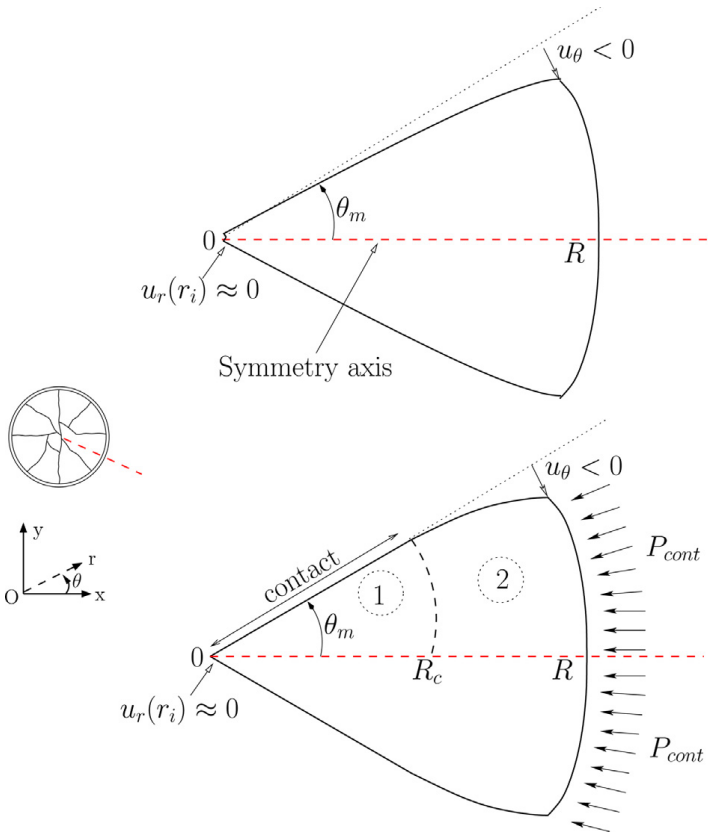

Figure 7: Pellet fragment submitted to an isotropic swelling only (top), pellet fragment submitted to an isotropic swelling and a contact pressure with two zones delimited by the contact radius (bottom), reproduced from [39].

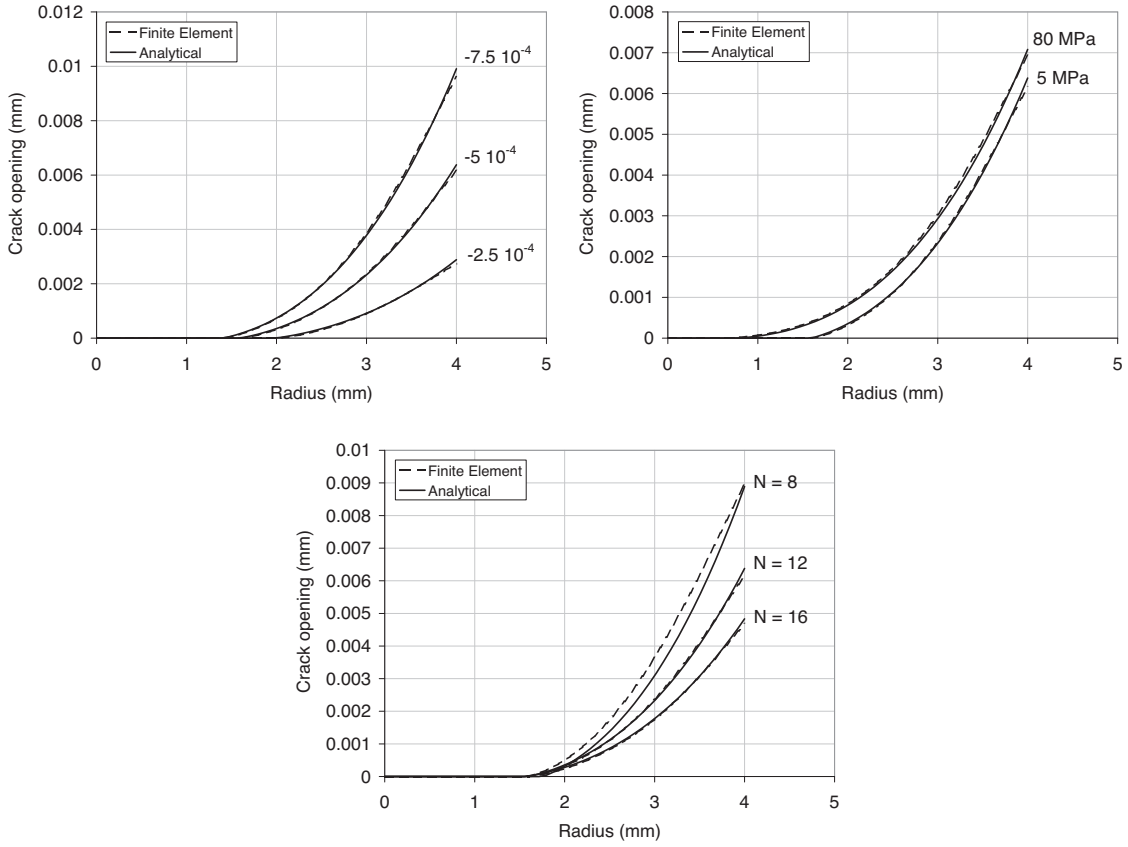

Figure 8: Impact of the thermal strains magnitude (top left), of the contact pressure (top right) and of the number of pellet fragments (bottom) on the crack opening radial profile, reproduced from [39].

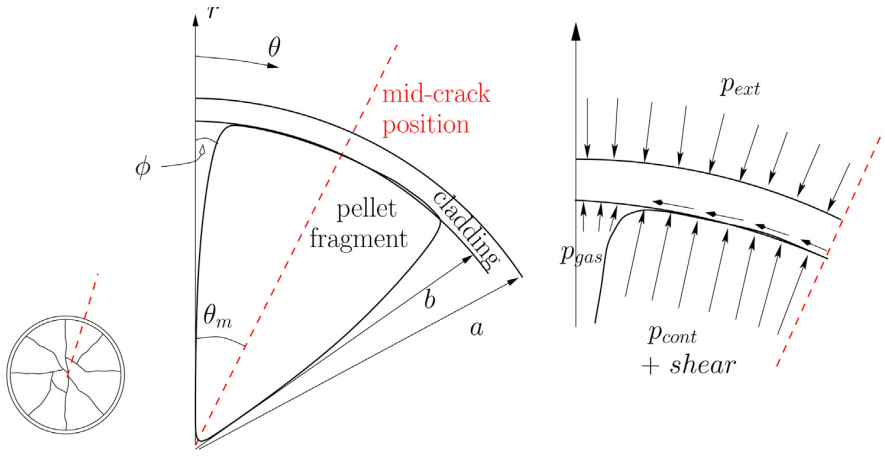

Figure 9: Schematic fuel clad model used in the clad stress calculations (adapted from Roberts [28]).

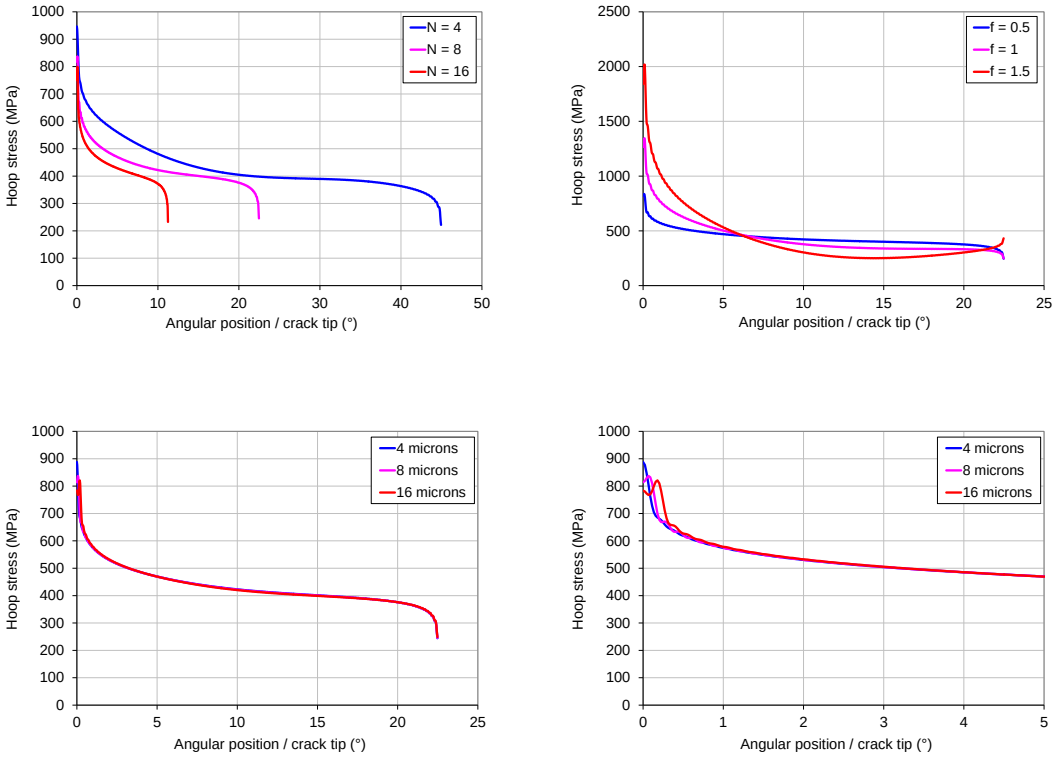

Figure 10: Hoop stress distribution in the clad inner wall as a function of the number of pellet fragments (top left), of the friction coefficient at the pellet-clad interface (top right), and of the pellet crack opening (bottom, zoom near the crack tip in the right graph), reproduced from [42].

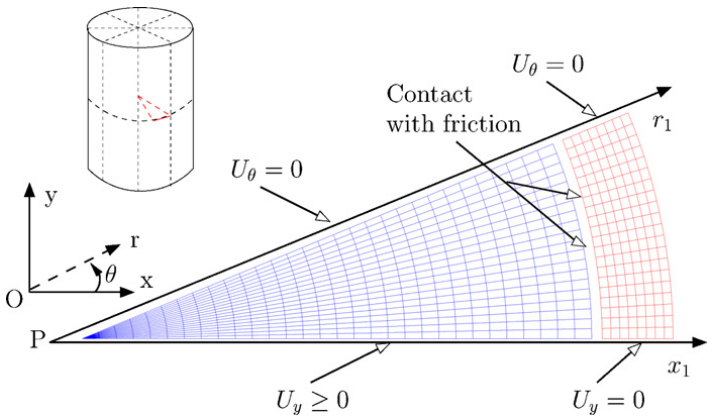

Figure 11: Mesh and boundary conditions in ALCYONE 2DRθ simulations, reproduced from [19].

Reactor startup, at full power

After reactor shutdown

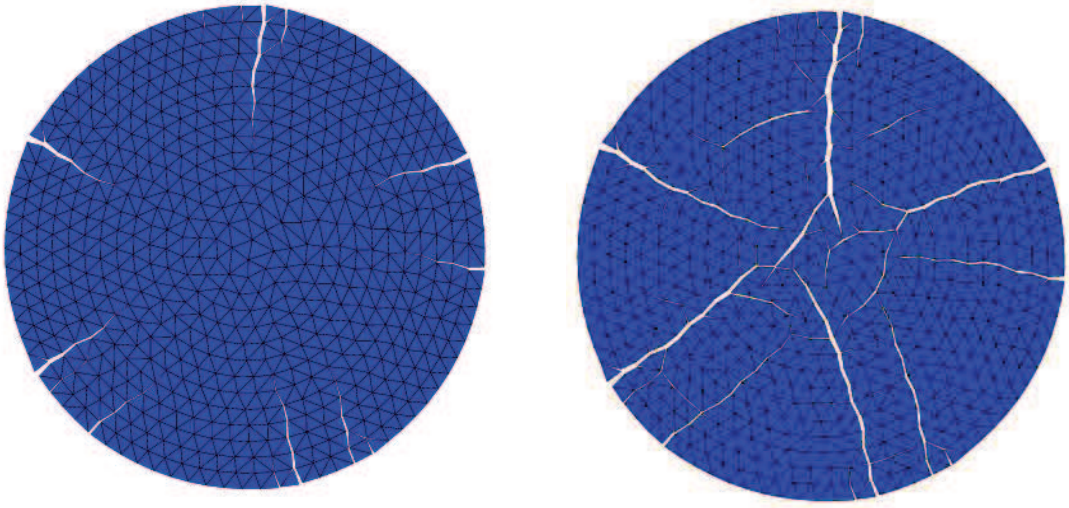

Figure 12: Simulations of fuel pellet radial cracking during base irradiation by interfacing all the continuum elements of the FE mesh with cohesive zones, reproduced from [53].

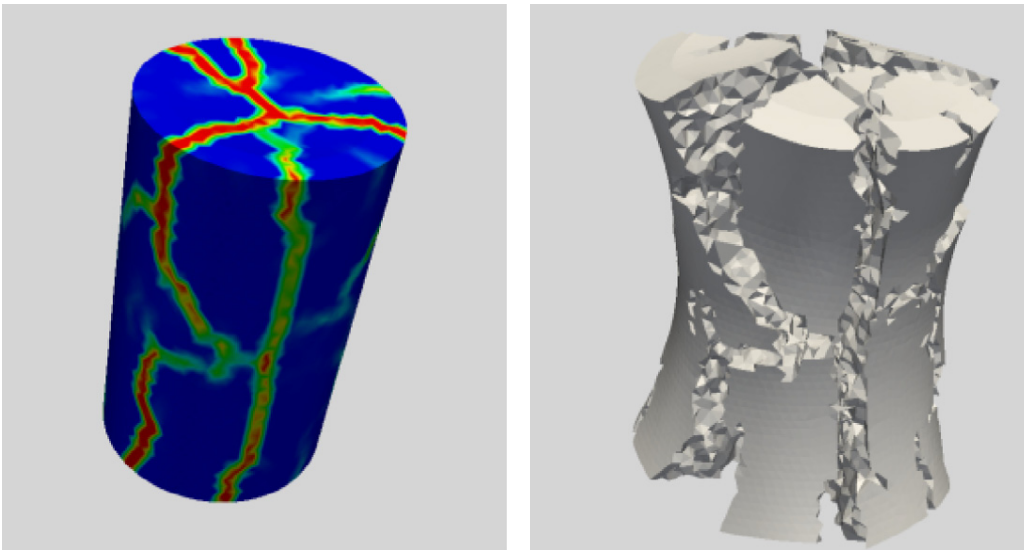

Figure 13: Calculated fuel pellet fragmentation during reactor start-up with a smeared crack model based on the principal stresses, reproduced from [54].

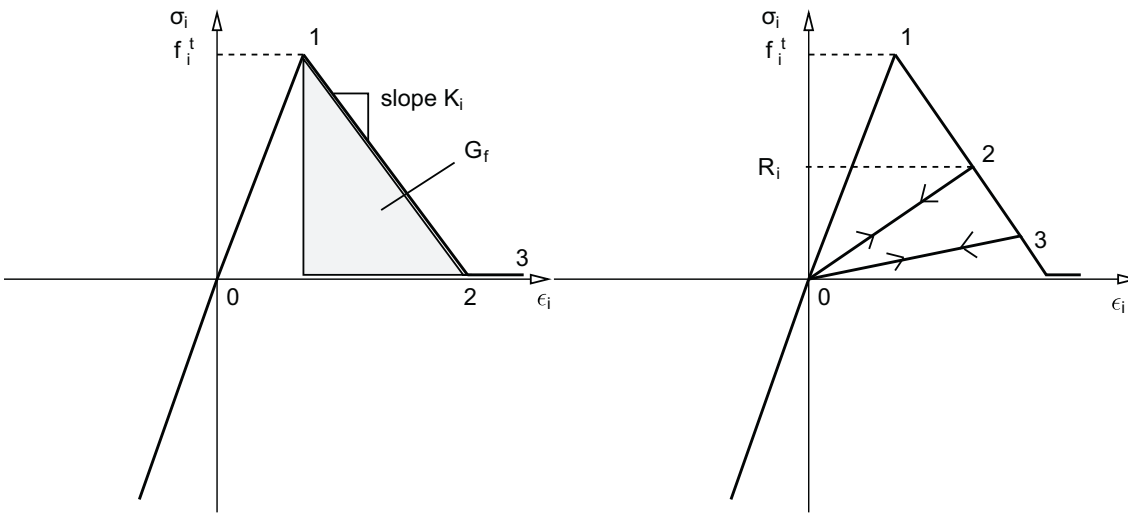

Figure 14: Stress-strain relation during monotonic (left) and cyclic (right) tensile loading, reproduced from [19].

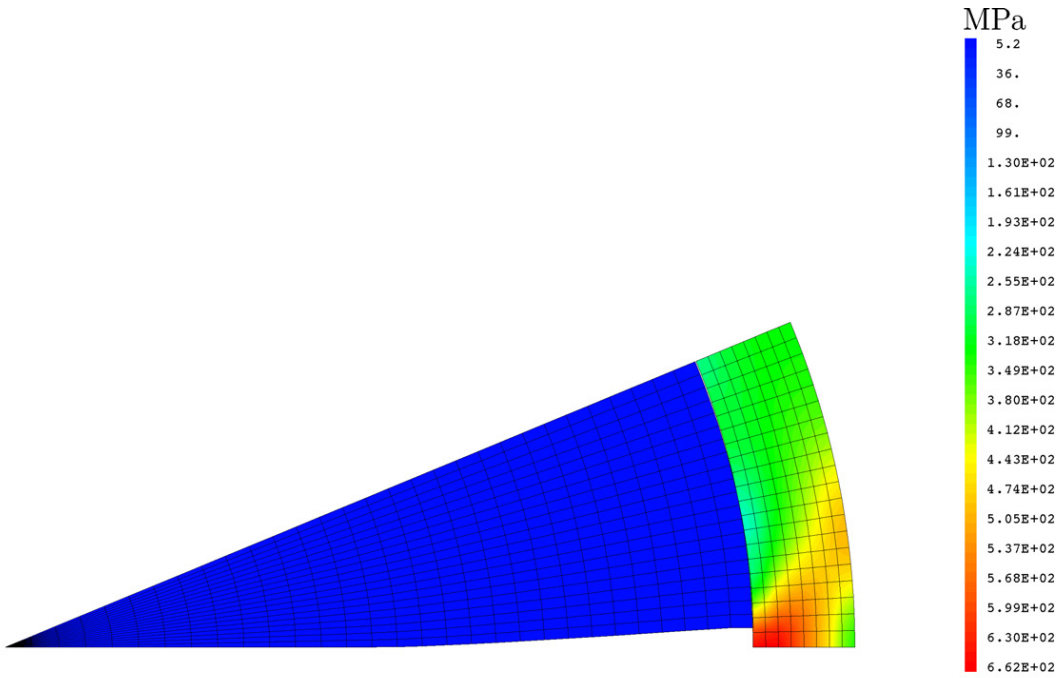

Figure 15: Hoop stress distribution in the cladding at RTL, reproduced from [19].

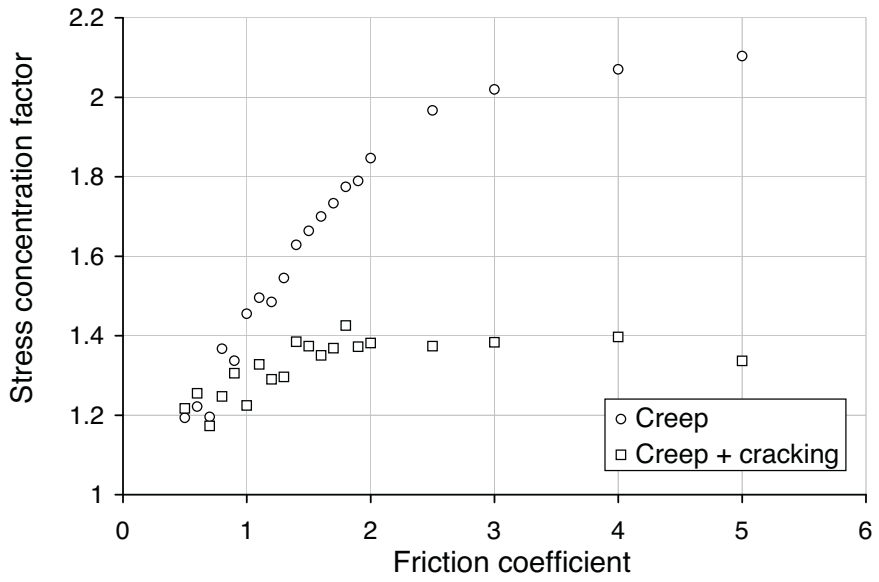

Figure 16: Stress concentration factor ($\sigma_{\theta\theta}^{max}/\sigma_{\theta\theta}^{average}$) in the cladding at RTL versus friction coefficient, reproduced from [19] (from 2DRθ simulations with fuel creep only or with fuel creep and cracking).

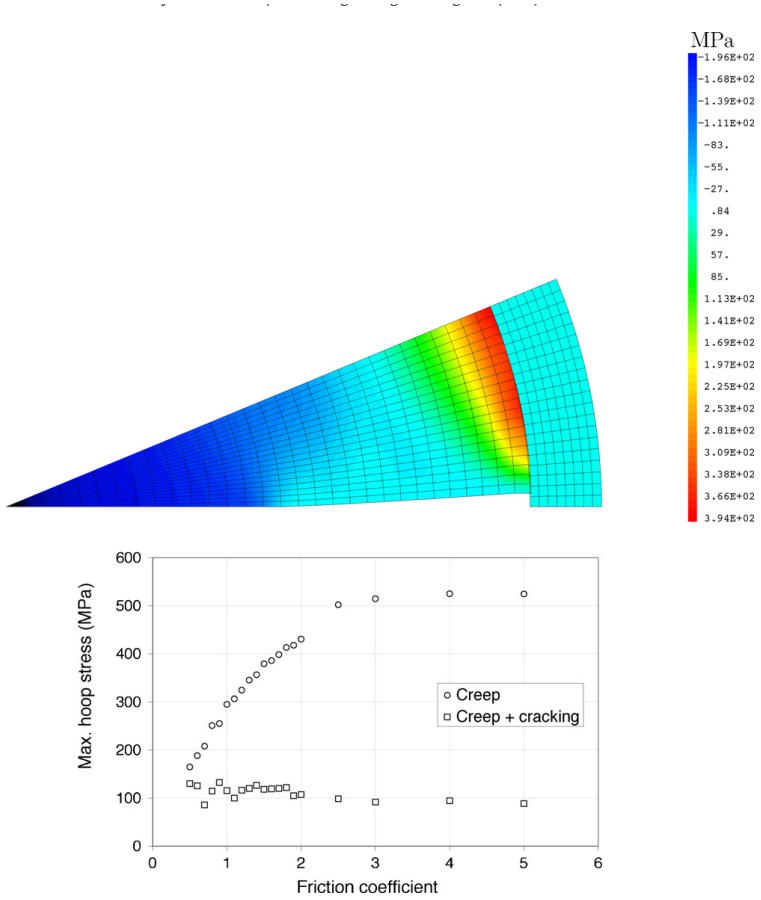

Figure 17: Hoop stress distribution at RTL (friction coefficient 1.7) and maximum hoop stress at the pellet periphery versus friction coefficient (bottom), reproduced from [19] (rom 2DRθ simulations with fuel creep only or with fuel creep and cracking).

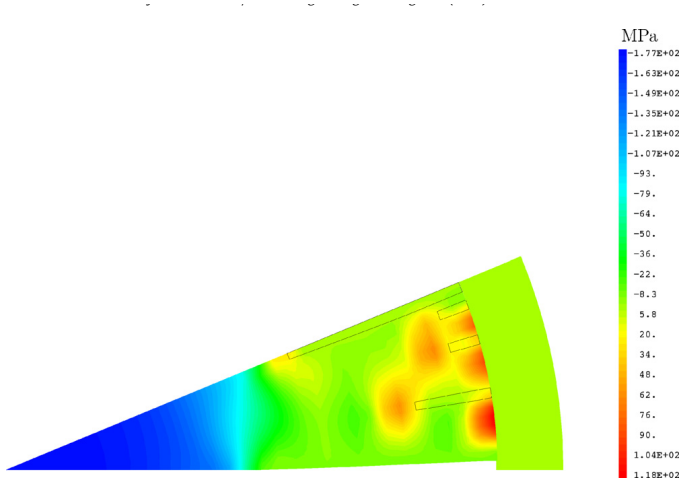

Figure 18: Hoop stress and secondary radial cracks calculated at RTL (friction coefficient 1.7), reproduced from [19].

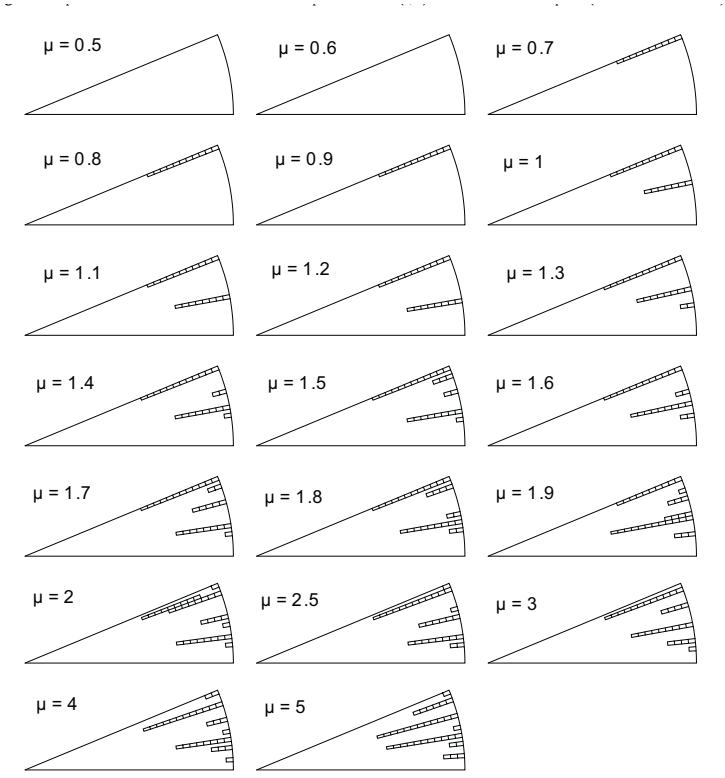

Figure 19: Secondary radial cracking as a function of the friction coefficient calculated, reproduced from [19].

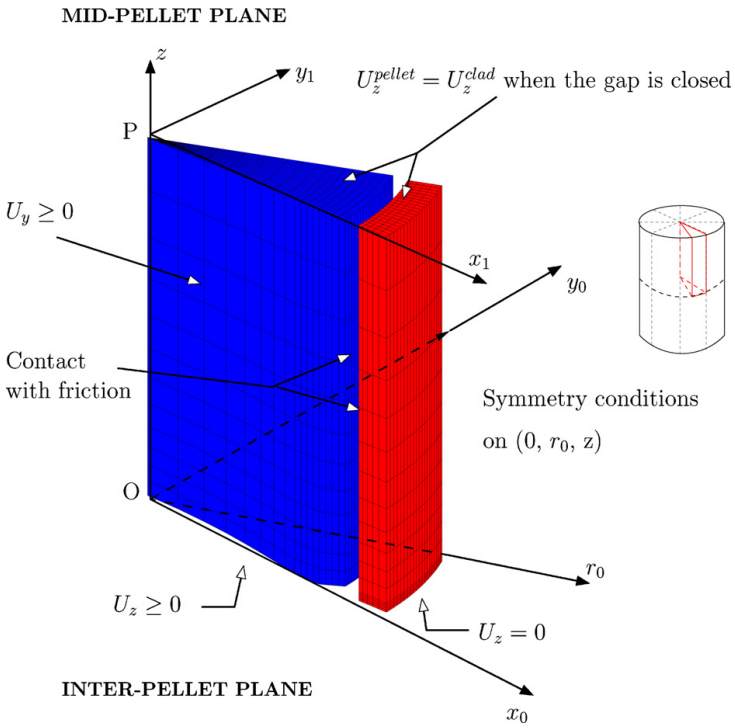

Figure 20: Mesh and boundary conditions in ALCYONE 3D simulations, reproduced from [19].

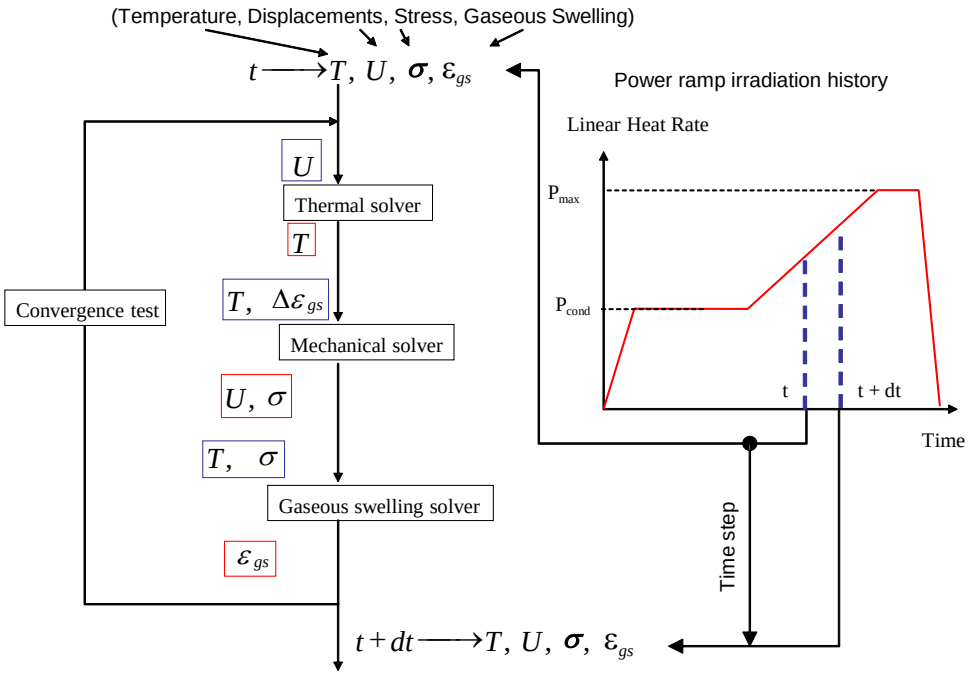

Figure 21: Iterative scheme of ALCYONE for solving the thermal, mechanical and gas swelling coupled system during a typical power ramp irradiation history, reproduced from [91].

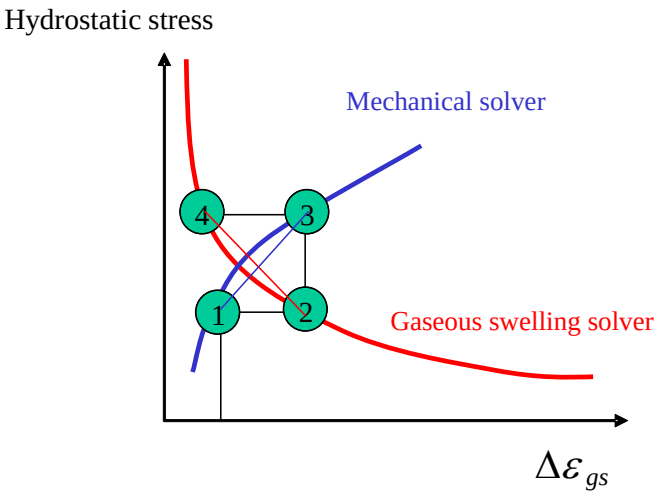

Figure 22: Schematic of the convergence algorithm for gaseous swelling in ALCYONE.

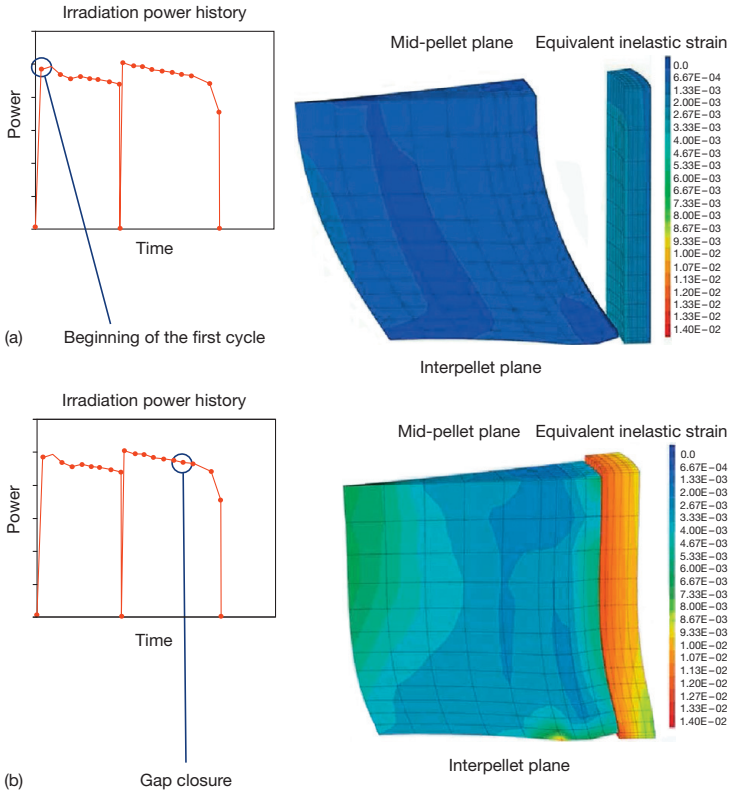

Figure 23: Pellet clad gap closure and formation of clad ridges during nominal irradiation, reproduced from [90] (pellet fragment deformation is magnified).

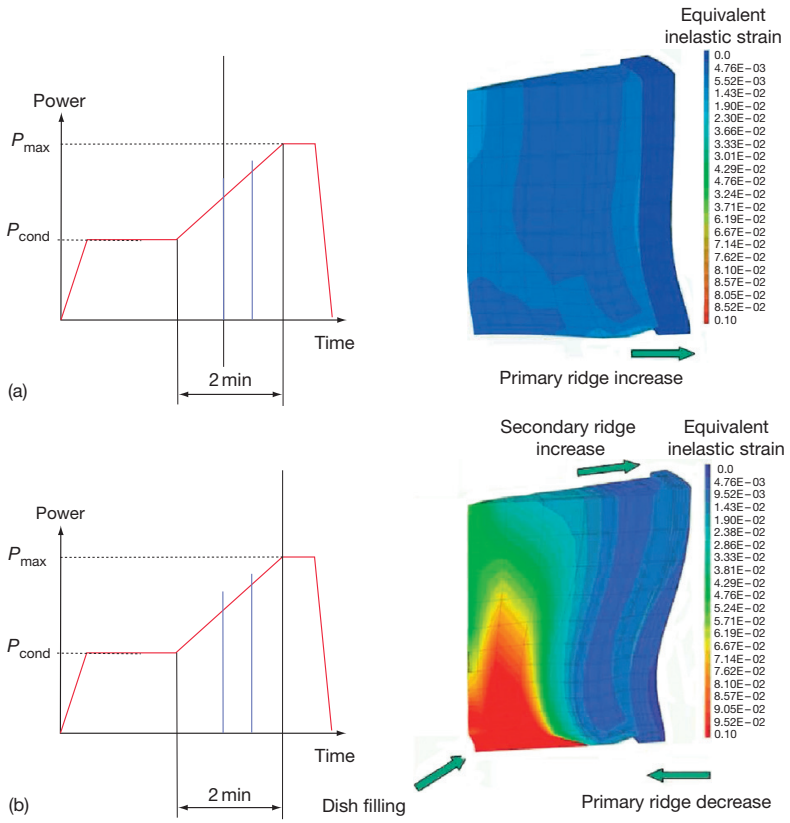

Figure 24: Pellet creep and formation of clad ridges during a power ramp, reproduced from [90] (pellet fragment deformation is magnified).

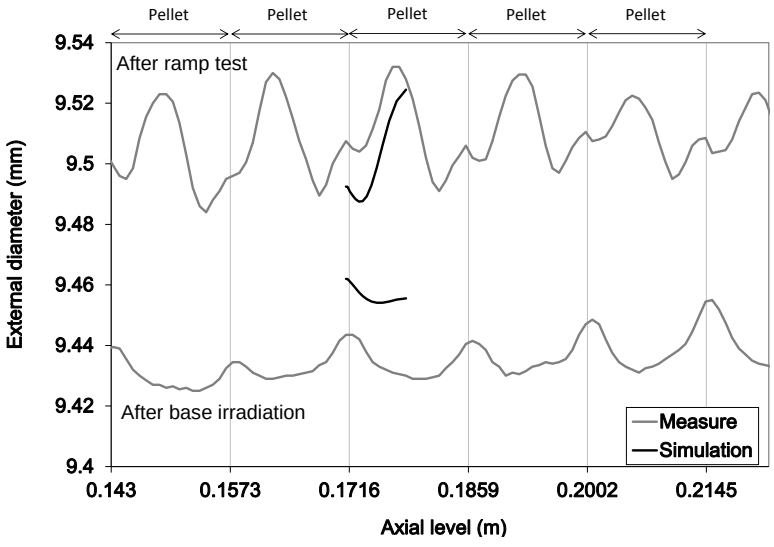

Figure 25: Calculated clad ridges after a base irradiation and a power ramp showing the noticeable development of MP ridges during ramp testing, compared to experimental measurements, reproduced from [7].

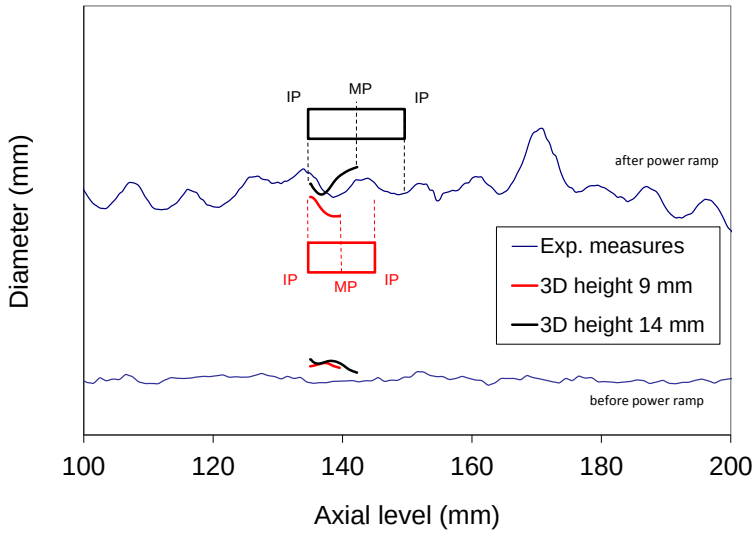

Figure 26: Calculated clad ridges after a base irradiation and a power ramp showing the impact of pellet heigth, compared to experimental measurements (pellet height 9 mm), reproduced from [7].

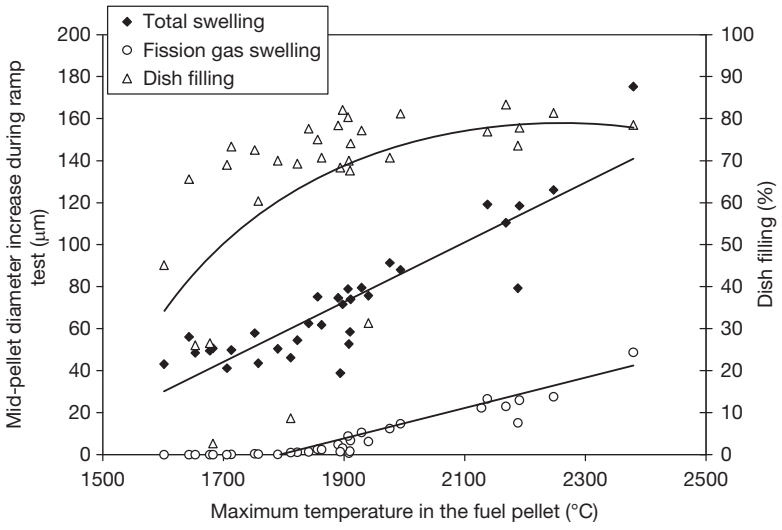

Figure 27: Calculated mid-pellet diameter increase due to total swelling and gaseous swelling only, calculated dish filling after cooling as a function of the maximum temperature in the pellet fragment, reproduced from [7].

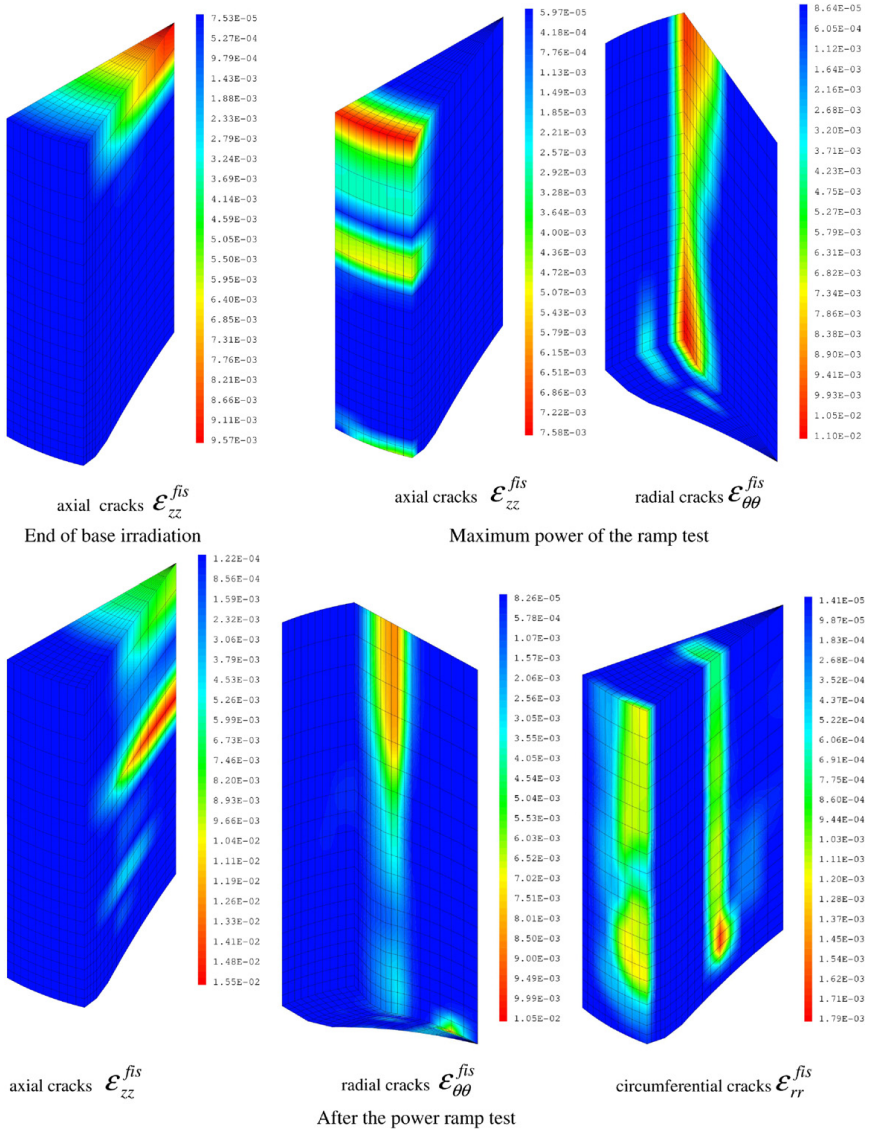

Figure 28: Radial, transverse (axial) and circumferential cracking strains at the end of base irradiation, during and after a power ramp, reproduced from [23].

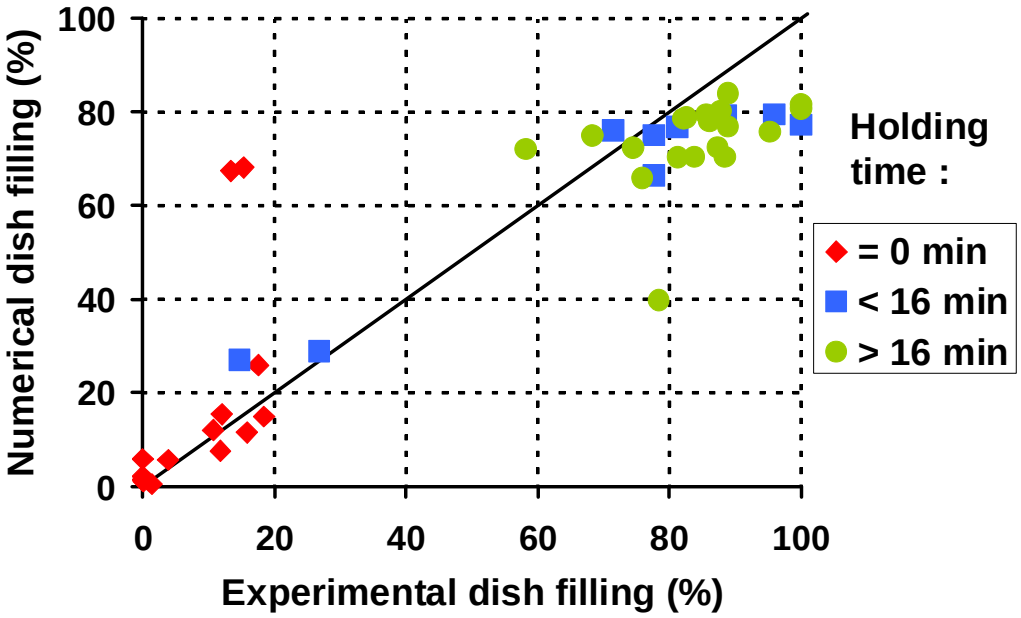

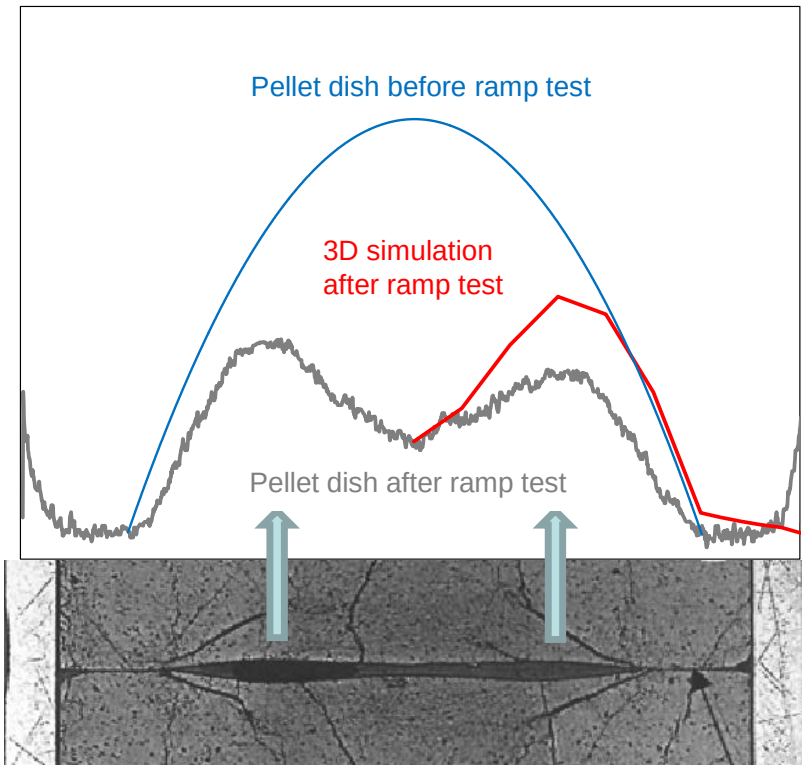

Figure 29: Calculated residual dish filling compared to experimental measurements from optical ceramographies, reproduced from [111] and [112].

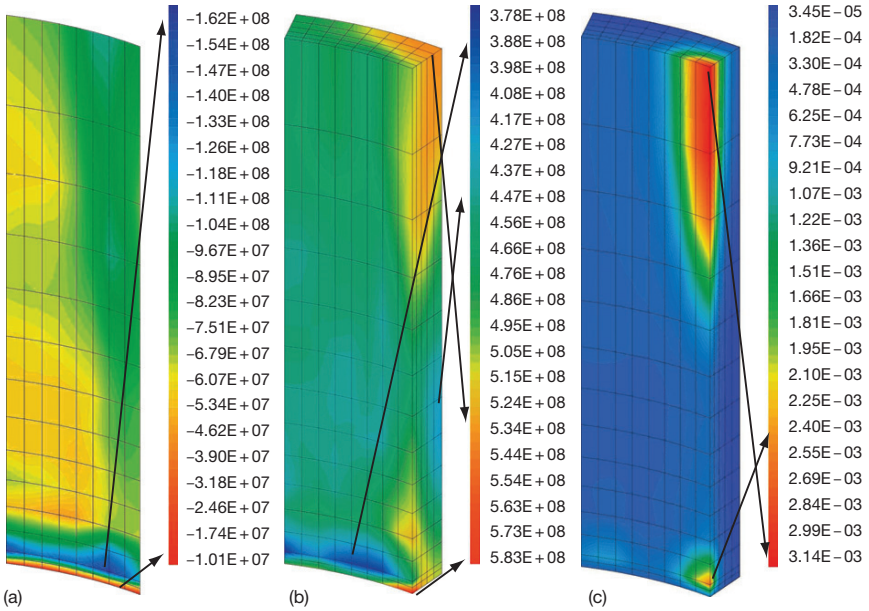

Figure 30: Calculated stress and strain fields in the cladding of a UO_2 rodlet at RTL, reproduced from [114]: (a) radial stress in Pa, (b) hoop stress in Pa, (c) equivalent cumulated creep strain. Triple point is at the bottom corner of the clad mesh.

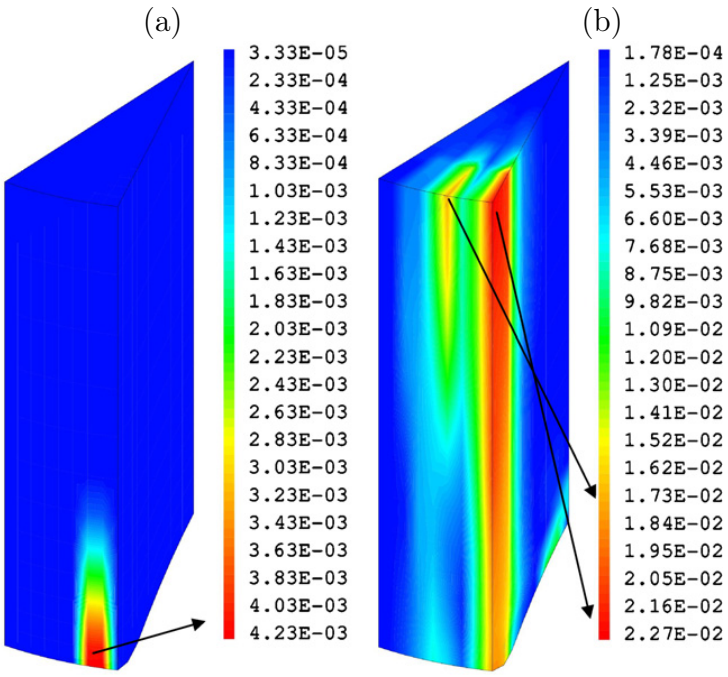

Figure 31: Calculated radial cracking at RTL reproduced from [114]: (a) standard UO_2 rodlet, (b) Cr-doped UO_2 rodlet.

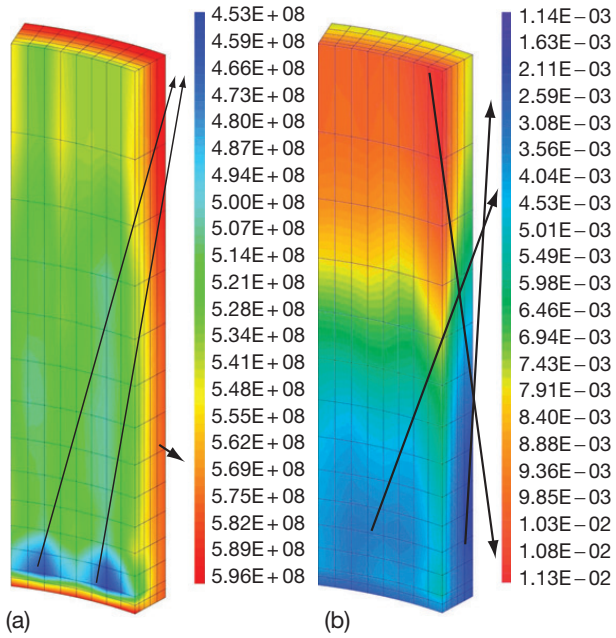

Figure 32: Calculated stress and strain fields in the cladding of a Cr-doped UO_2 rodlet at RTL reproduced from [114]: (a) hoop stress in Pa, (b) equivalent cumulated creep strain.

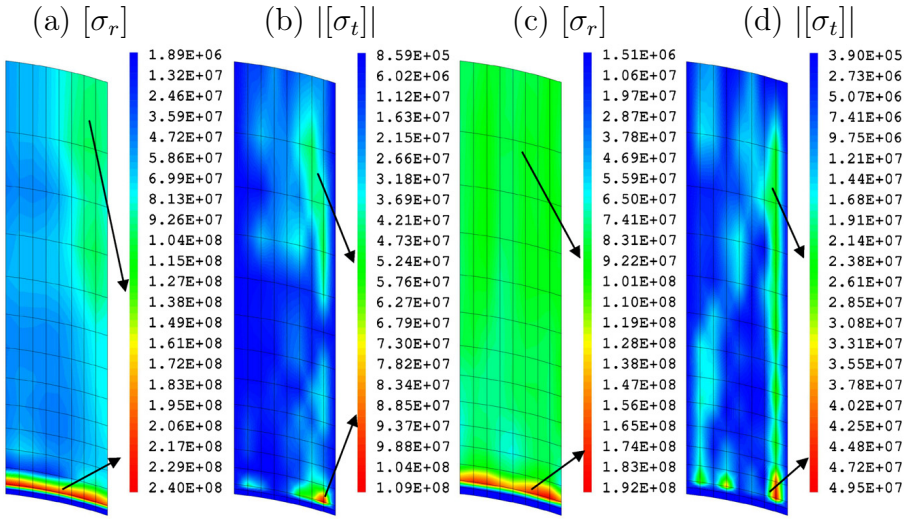

Figure 33: Radial and tangential stresses (absolute value) in Pa at the pellet-clad interface for the standard UO_2 rodlet (respectively (a) and (b)) and for the Cr-doped UO_2 rodlet (respectively (c) and (d)), reproduced from [114]. Triple point is a the bottom corner of the clad mesh.

(a) $[\sigma_r]$ (b) $[\sigma_t]$ (c) $[\sigma_r]$ (d) $[\sigma_t]$

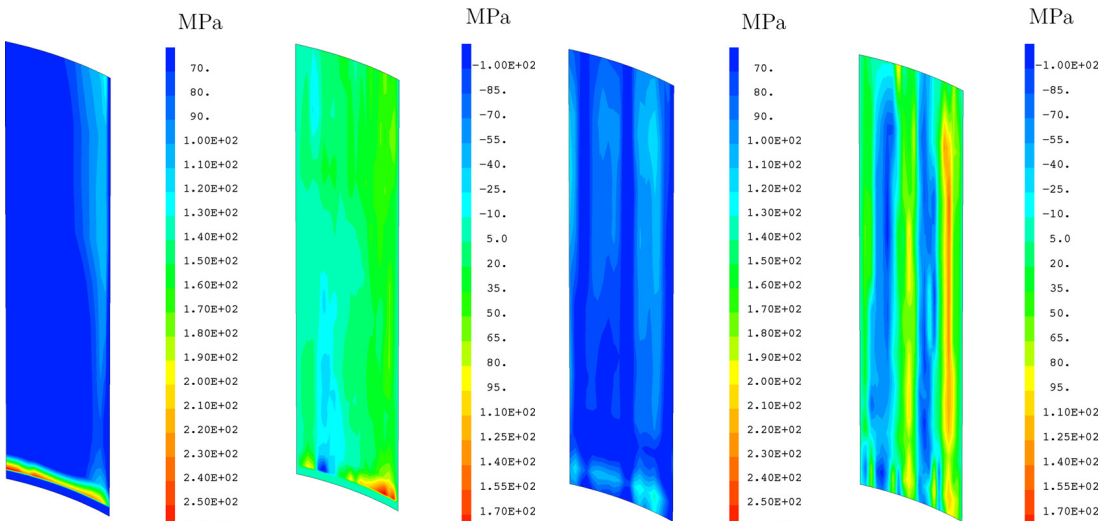

Figure 34: Radial and tangential stresses in MPa at the pellet-clad interface for a 25 GWd/tU UO_2 rodlet (respectively (a) and (b)) and for a 50 GWd/tU UO_2 rodlet (respectively (c) and (d)), reproduced from [19].

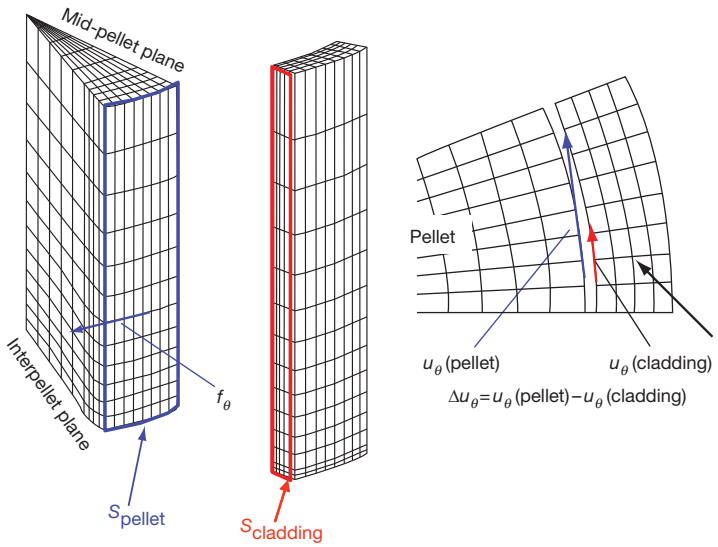

Figure 35: Surfaces used to compute the shear energy density at the pellet-clad interface, reproduced from [114].

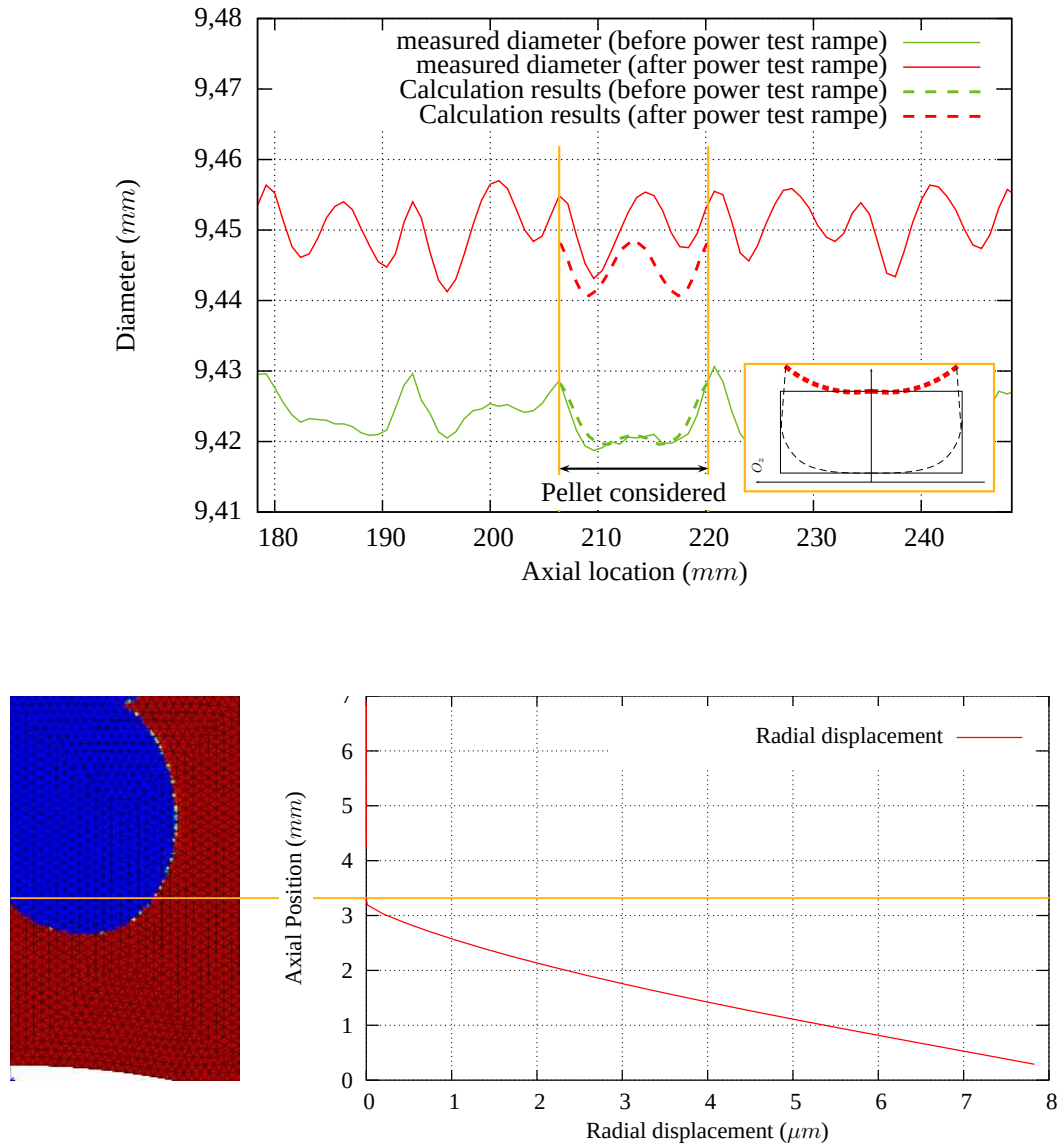

Figure 36: Top: Calculated radial cracking (red = fully cracked, blue = uncracked) and corresponding radial displacement along the axis of symmetry, reproduced from [119].

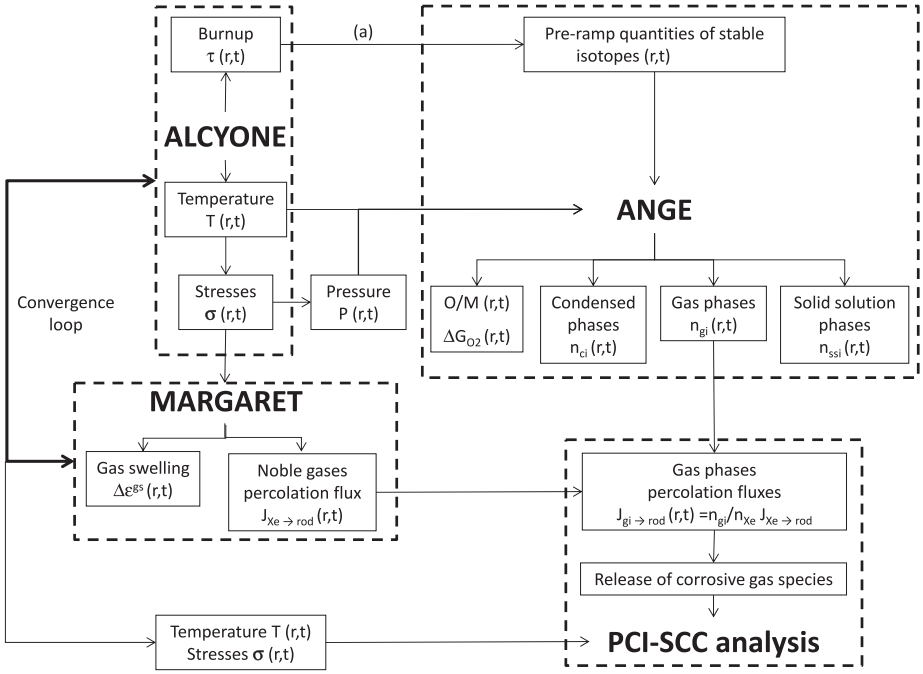

Figure 37: Schematic representation of the coupling within the fuel code ALCYONE of inert FG model MARGARET and of the thermo-chemical code ANGE, reproduced from [92]. (a) The pre-ramp quantities of stable isotopes are obtained from the empirical correlations given in Table 2.

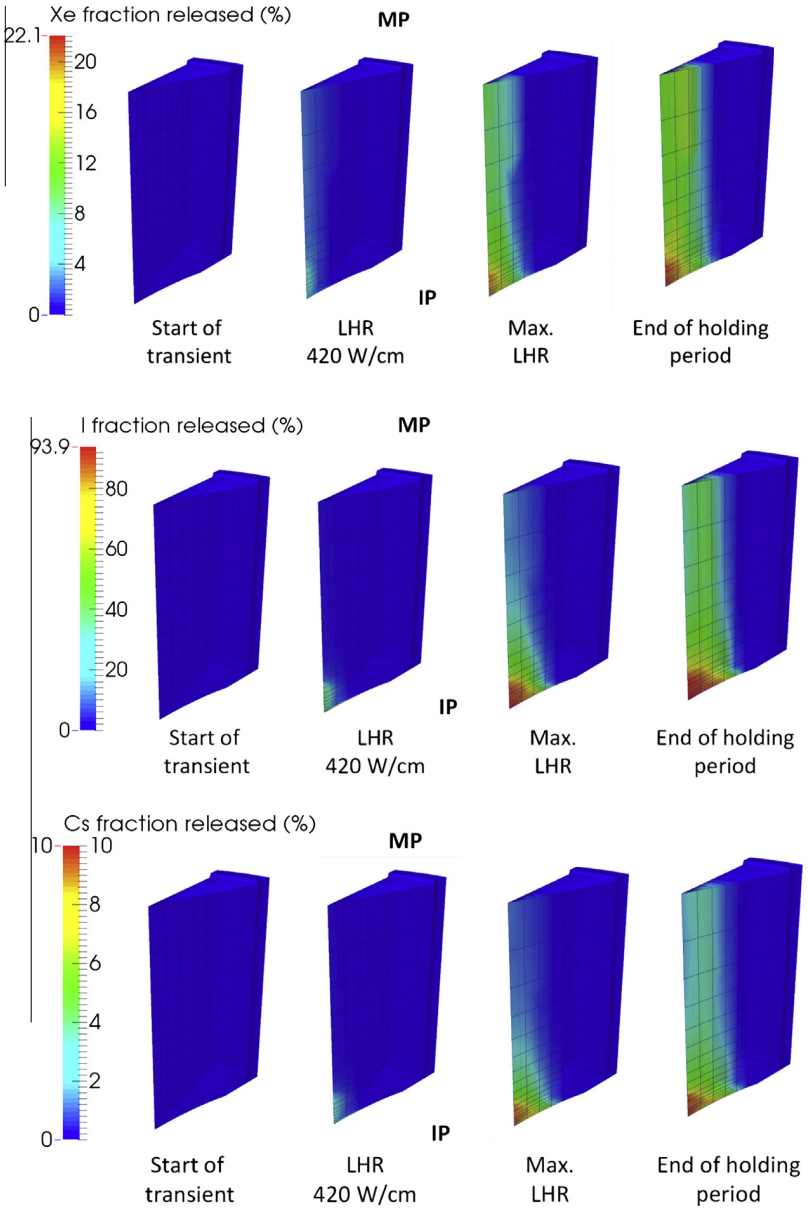

Figure 38: Calculated evolution of the volatile fission products release (Xe, I and Cs) in the fuel fragment during a power ramp, reproduced from [92] (in % of the pre-ramp inventory).

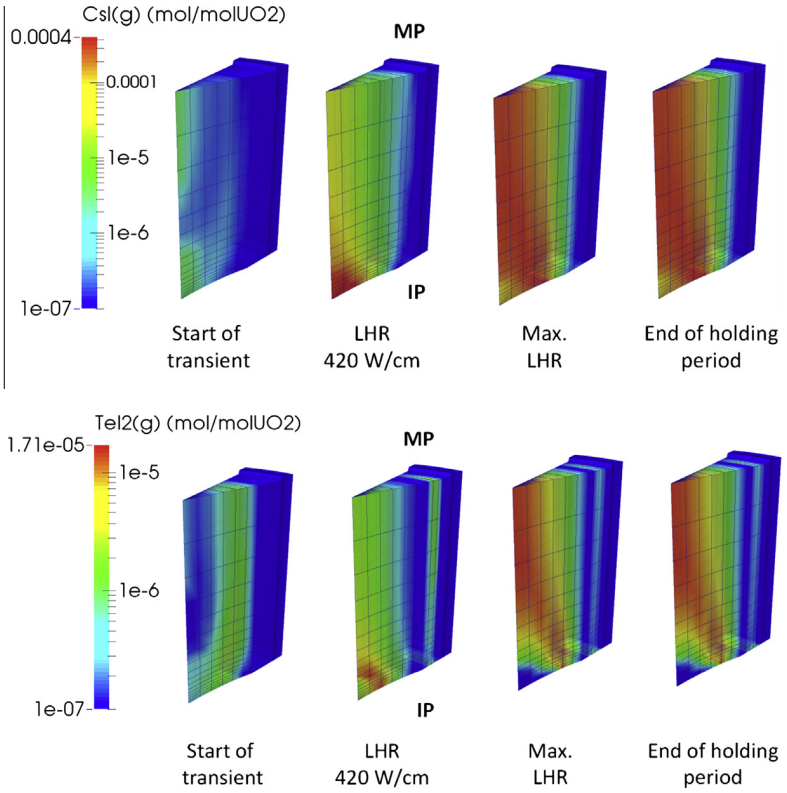

Figure 39: Calculated evolution of the concentrations in gaseous $CsI_{(g)}$ and $TeI_{2(g)}$ (mol/mol UO_2) during a power ramp, reproduced from [92].

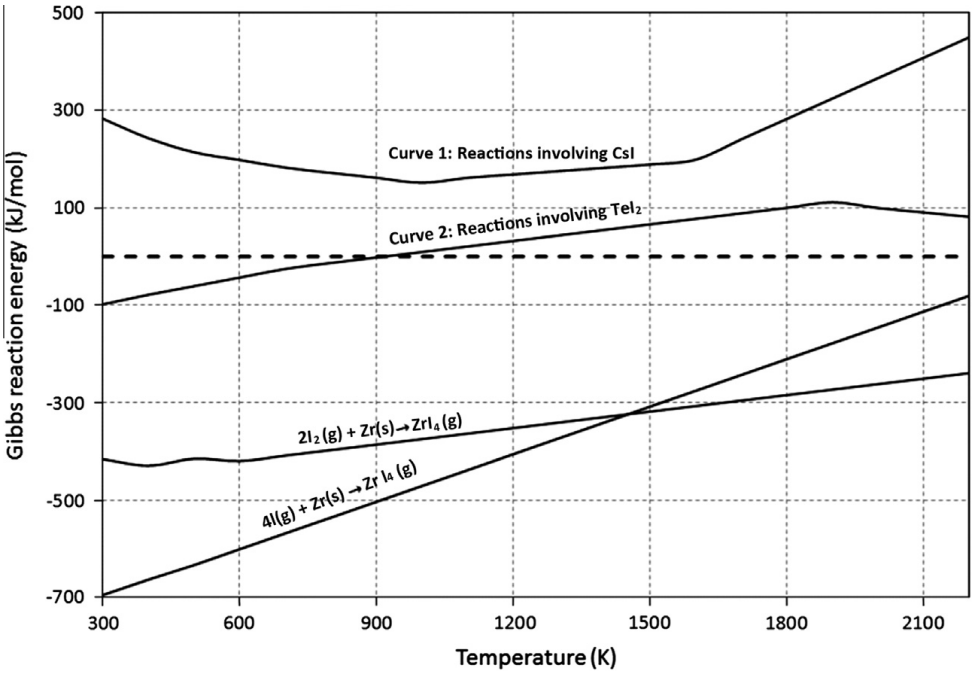

Figure 40: Ellingham diagram of the various reactions involved between $Zr_{(s)}$ and the gaseous iodine forms I, I_2, CsI and TeI_2, reproduced from [92]. Curve 1 includes the following reactions involving $CsI_{(s,l,g)}$: 300 K to 800 K, $4CsI_{(s)} + Zr_{(s)} + 2Te_{(s)} \rightarrow ZrI_{4(g)} + 2Cs_2Te_{(s)}$, 800 K to 1000 K, $4CsI_{(s)} + Zr_{(s)} + 2Te_{(l)} \rightarrow ZrI_{4(g)} + 2Cs_2Te_{(s)}$, 1000 K to 1600 K, $4CsI_{(l)} + Zr_{(s)} + 2Te_{(l)} \rightarrow ZrI_{4(g)} + 2Cs_2Te_{(s)}$, 1600 K to 2200 K, $4CsI_{(g)} + Zr_{(s)} + 2Te_{(l)} \rightarrow ZrI_{4(g)} + 2Cs_2Te_{(s)}$. Curve 2 includes the following reactions involving $TeI_{2(g)}$: 300 to 800 K, $2TeI_{2(g)} + Zr_{(s)} \rightarrow ZrI_{4(g)} + 2Te_{(s)}$, 800K to 1300 K, $2TeI_{2(g)} + Zr_{(s)} \rightarrow ZrI_{4(g)} + 2Te_{(l)}$, 1300K to 2200 K, $2TeI_{2(g)} + Zr_{(s)} \rightarrow ZrI_{4(g)} + Te_{2(g)}$.

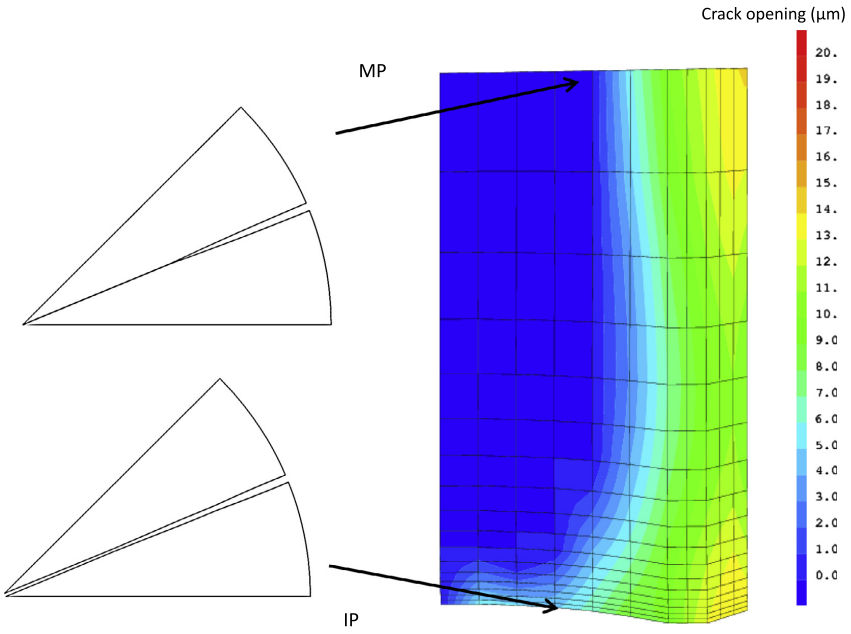

Figure 41: Calculated pellet radial crack opening (in μm) on the fracture plane at RTL. Illustration of the differences in crack aperture at MP and IP level (magnified 4 times), reproduced from [92].

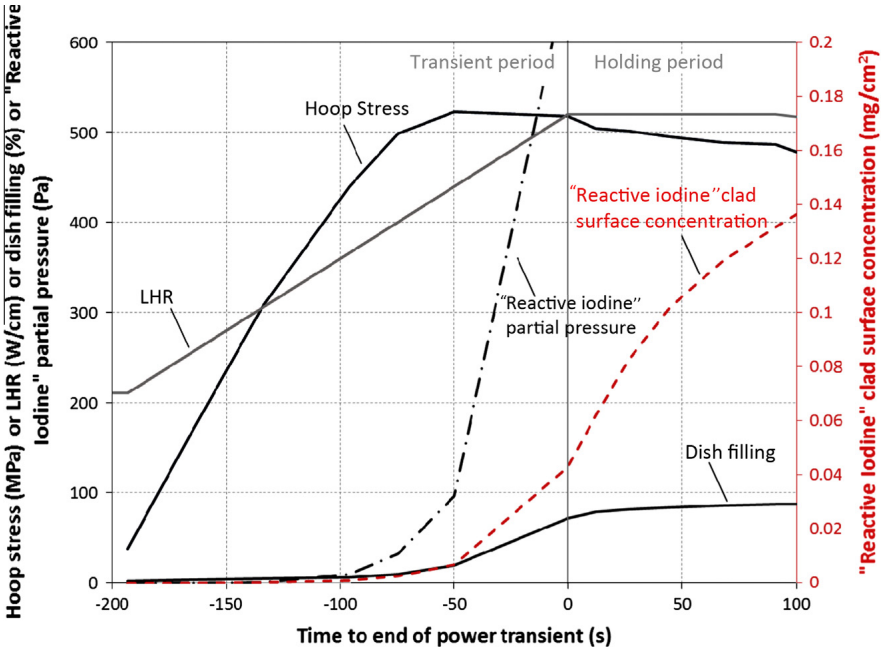

Figure 42: Calculated evolution of the maximum hoop stress at IP level (MPa), of dish filling (%), of the clad surface concentration in "reactive iodine" (mg/cm^2) and of the "reactive iodine" total pressure (Pa) during the power ramp, reproduced from [92]. "Reactive iodine" includes the iodine species $TeI_{2(g)}$, $I_{(g)}$ and $I_{2(g)}$. Hoop stress at IP level (MPa), LHR (W/cm), dish filling (%),and "Reactive iodine" partial pressure (Pa) refer to the linear scale shown to the left. "Reactive Iodine" clad surface concentration refers to the linear scale shown to the right.

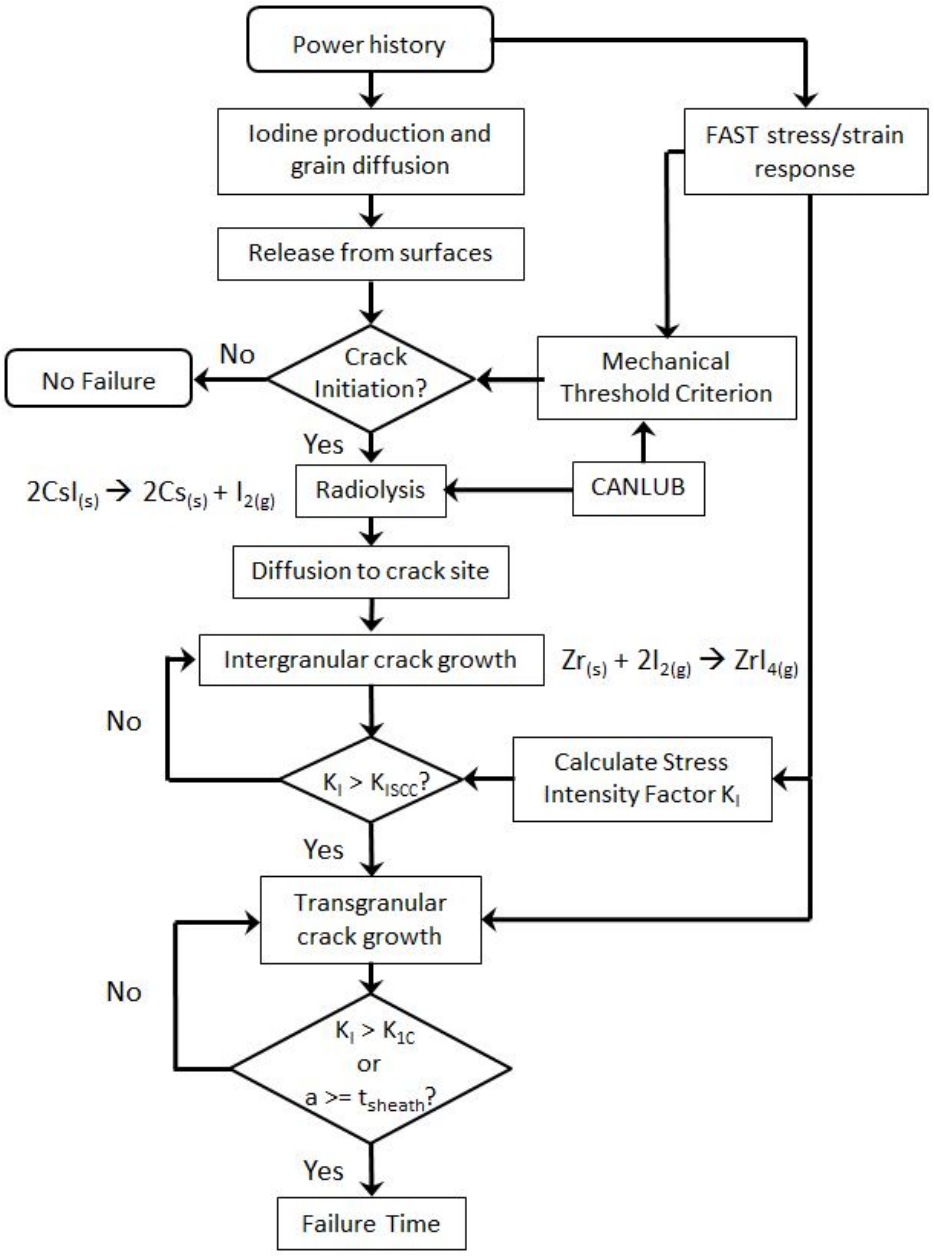

Figure 43: Flow chart of the I-SCC model of Lewis et al. [146] used in post-processing of the stresses and strains calculated by the FAST code, reproduced from [156].

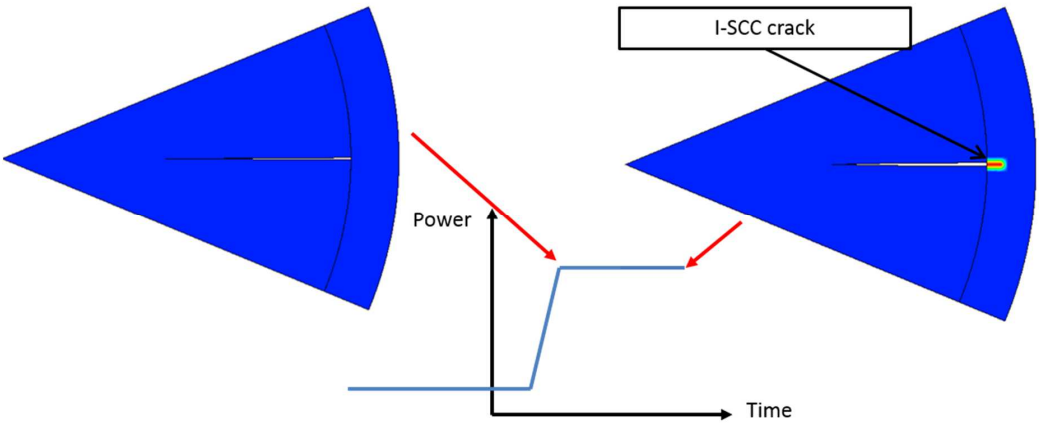

Figure 44: Simulation with ALCYONE and the I-SCC damage model of Leboulch et al. of an I-SCC crack propagation during a ramp test, reproduced from [151].

Table 1: Summary of the models used in the fuel performance code ALCYONE [19].

Fuel properties	
Thermal conductivity	Modified Lucuta's formulation [160]
Thermal expansion coefficient	Martin's formulation for UO_2 [161]
Elasticity coefficients	Martin's formulation for temperature dependency [162]
Creep	Irradiation, scattering and dislocation creep [66]
Cracking	(r, θ, z) smeared crack model [23]
Densification - solid swelling	[163]
Radial power profiles	Modified version of RADAR [164]
Gaseous swelling	stress-dependent intra- and inter-granular bubble swelling model [99]
Clad properties	
Thermal conductivity	SRA Zy-4 temperature-dependent model [163]
Thermal expansion coefficient	SRA Zy-4 anisotropic model (Internal CEA report, 1981)
Elasticity coefficients	SRA Zy-4 isotropic model (Internal CEA report, 1981)
Inelastic clad behavior	SRA Zy-4 anisotropic formulation based on Hill's criterion [18] Irradiation-induced creep, low-stress creep High-stress creep and plasticity
Pellet-clad interface	
Pellet-clad gap thermal heat transfer	URGAP model [165]
Friction between pellet and cladding	Coulomb law [40]

Table 2: Representative elements and quantities of fission product per at% burn-up and per mol of unirradiated UO_2 fuel considered in ANGE calculations [92].

Fission Products	**Representative element**	**Creation mol/mol UO_2/at%)**	**Family**
He+Xe+Kr	He	$3.06\ 10^{-3}$	Inert fission
Cs+Rb	Cs	$1.7\ 10^{-3}$	gas and
I+Br	I	$1.31\ 10^{-4}$	volatile fission
Te+Se+Ge+As	Te	$3.02\ 10^{-4}$	products
Ba+Sr	Ba	$1.38\ 10^{-3}$	Stable oxides
Zr+Nb	Zr	$2.62\ 10^{-3}$	
Mo	Mo	$2.33\ 10^{-3}$	
Ru+Tc+Rh	Ru	$2.44\ 10^{-3}$	Metallic fission
Pd+Sn+Sb	Pd	$1.02\ 10^{-3}$	products
Ce+Pr	Ce	$1.24\ 10^{-3}$	Fission
Eu+Sm	Eu	$3.81\ 10^{-4}$	products and
La+Y	La	$9.31\ 10^{-4}$	actinides in
Gd+Nd+Pm	Gd	$1.92\ 10^{-3}$	solid solution
Pu+Np+Am+Cm	Pu	$5.35\ 10^{-3}$	in UO_2

List of Tables

List of Figures